

Universität Stuttgart



Max-Planck-Institut für
Intelligente Systeme

Interfaces in fluids of Ionic Liquid Crystals

Von der Fakultät für Mathematik und Physik der Universität
Stuttgart zur Erlangung der Würde eines Doktors der
Naturwissenschaften (Dr. rer. nat.) genehmigte Abhandlung

Vorgelegt von
Hendrik Bartsch
aus Stuttgart

Tag der mündlichen Prüfung: **10. Mai 2019**

Hauptberichter: **Prof. Dr. Siegfried Dietrich**

Mitberichter: **Prof. Dr. Christian Holm**

Institut für Theoretische Physik IV, Universität Stuttgart &
Max-Planck-Institut für Intelligente Systeme, Stuttgart

2019

“It can scarcely be denied that the supreme goal of all theory is to make the irreducible basic elements as simple and as few as possible without having to surrender the adequate representation of a single datum of experience.”

Albert Einstein in *On the Method of Theoretical Physics*,
The Herbert Spencer lecture, Oxford, 10 June 1933.

Danksagungen

An dieser Stelle danke ich all jenen Menschen, die durch ihre fachliche oder persönliche Unterstützung zum Gelingen dieser Arbeit beigetragen haben.

Zunächst möchte ich Ihnen, Prof. Dr. Siegfried Dietrich, meinen tiefsten Dank dafür aussprechen, dass Sie es mir ermöglicht haben, diesem wissenschaftlichen Projekt nachzugehen. Ihre Expertise und Sachkenntnis, die Sie stets konstruktiv einbringen, haben mich im gleichen Maße beeindruckt, wie Ihre unterstützende und menschliche Art. Zudem danke ich Ihnen für das entgegengebrachte Vertrauen, welches es erst ermöglicht, während der Promotionszeit, eigene Ideen zu entwickeln und diese umzusetzen. Diese Zeit war enorm lehrreich für mich.

Vielen Dank Ihnen, Prof. Dr. Christian Holm und Prof. Dr. Tilman Pfau, für die bereitwillige Übernahme des Mitberichts beziehungsweise des Vorsitzes des Prüfungsausschusses.

Lieber Prof. Dr. Markus Bier, Dir möchte ich meinen tief empfundenen Dank für Deine vielen Hilfestellungen und Ratschläge aussprechen. Nicht nur Dein fachkundiges Wissen über physikalische wie auch technische Dinge, sondern auch die Leichtigkeit mit der Du es vermagst, diese zu vermitteln, beeindruckten mich sehr.

Lieber Dr. Nima Farahmand Bafi, ich danke Dir für die großartige gemeinsame Zeit als Bürokollegen. In dieser Zeit ist eine wahre Freundschaft gewachsen, welche ich nicht mehr missen möchte.

Darüber hinaus danke ich allen weiteren Kollegen aus der Abteilung für die Hilfsbereitschaft und für die freundliche Arbeitsatmosphäre. Insbesondere danke ich Euch, Anke Geigle und Simone Blümlein, für die Hilfe bei Verwaltungsangelegenheiten und diversen anderen Formalitäten.

Liebe Cora, die Nähe und Unterstützung, die ich jeden Tag durch Dich erfahre, sind von unermesslichem Wert für mich. Dafür kann ich Dir nicht genug danken.

Im gleichen Maße bin ich Euch, Daisy und Harald, als meinen Eltern, von ganzem Herzen dankbar für die bedingungslose Liebe und Unterstützung, die Ihr mir entgegenbringt und schon immer entgegenbrachtet. Dieser Rückhalt ist stets aufbauend und zugleich ermutigend für mich.

Auch Euch, Oma Lisa, Opa Rolf und Dir, Tante Ruth, danke ich für Eure stete Hilfsbereitschaft und für die Zeit, die ich mit Euch verbringen durfte. Die vielen wunderbaren Kindheitserinnerungen bleiben mir ewig.

Erklärung

Hiermit erkläre ich, Hendrik Bartsch, dass ich, abgesehen von den ausdrücklich bezeichneten Hilfsmitteln, diese Dissertation selbstständig verfasst habe und dass die eingereichte Arbeit weder vollständig noch in wesentlichen Teilen Gegenstand eines anderen Prüfungsverfahrens gewesen ist.

Unterschrift

Ort, Datum

Contents

Danksagungen	v
Erklärung	vii
Zusammenfassung	11
Summary	19
1. General introduction	25
1.1. Studies on ionic liquid crystals and the aim of the present work	26
1.2. Basic concepts of classical density functional theory (DFT)	32
2. Model and formalism	37
2.1. Molecular model and pair potential	38
2.2. Present DFT framework	43
3. Bulk phase behavior of ILCs	49
3.1. Introduction	50
3.2. Methods	52
3.2.1. Bulk phases within the present DFT framework	52
3.2.2. Phase behavior	54
3.2.3. Crystallization	56
3.2.4. Grand canonical Monte Carlo simulation	61
3.3. Results	63
3.3.1. Phase diagrams	63
3.3.2. Variety of smectic structures	73
3.3.3. Temperature dependence of the layer spacing	81
3.4. Conclusions	82

4. Free interfaces in ILCs	87
4.1. Introduction	88
4.2. Methods	89
4.2.1. Free interfaces within the present DFT framework	89
4.2.2. Gibbs dividing surface	94
4.2.3. Interfacial tension	95
4.3. Results	95
4.3.1. Interface normal parallel to the smectic layer normal ($\alpha = 0$) . . .	96
4.3.2. Interface normal perpendicular to the layer normal ($\alpha = \pi/2$) . .	100
4.3.3. Asymptotic behavior	104
4.3.4. Tilted interfaces	110
4.4. Conclusions	114
5. Conclusions and outlook	119
A. Derivation of Eq. (3.1)	125
B. Comparison between the exact and the approx. bulk solution	127
C. Derivation of Eq. (3.8)	129
D. Implications of the presence of odd Fourier modes in $\bar{\varrho}(\mathbf{r}, \omega)$	131
Bibliography	135

Zusammenfassung

Die technologische Bedeutung von ionischen Flüssigkristallen (ILCs, englisch: „Ionic Liquid Crystals“) beruht zum einen auf ihrer Fähigkeit flüssigkristalline Phasen, sogenannte Mesophasen, auszubilden. Zudem bestehen sie aus Ionen und können somit als ein Medium für Ladungstransport verwendet werden. Diese Kombination von Nanostrukturen und der Verfügbarkeit von Ladungsträgern macht sie zu vielversprechenden Kandidaten für Anwendungen im Bereich der Energiespeicherung und Energieumwandlung, zum Beispiel in (Hochleistungs)-Batterien, Brennstoffzellen oder Solarzellen. Heutzutage können unterschiedlichste Varianten von ILCs synthetisch hergestellt werden. Beispielsweise ermöglichen verschiedenste Kombinationen von (geladenen) Imidazolium-Ringen und Alkylketten es, die Länge, wie auch die Ladungsverteilung der Ionen nach Belieben zu verändern. Hierdurch ist man in der Lage, jene besonderen Eigenschaften ionischer Flüssigkristalle zu verstärken, welche für konkrete technologische Anwendungen von Nutzen sind. Ein grundlegendes Verständnis des Zusammenhangs zwischen den (intrinsischen) molekularen Eigenschaften und dem daraus resultierenden (makroskopischen) Verhalten dieser Materialien ist hierfür erforderlich und es bedarf daher weiterer theoretischer Arbeit auf diesem wissenschaftlichen Gebiet.

In diesem Zusammenhang zielt die vorliegende Dissertation zunächst auf die Entwicklung einer theoretischen Darstellung ab, welche im Stande ist, sowohl Bulk-, als auch Grenzflächensysteme von ionischen Flüssigkristallen zu beschreiben (Kapitel 2). Darüber hinaus sollen Vorhersagen über die thermodynamischen und strukturellen Eigenschaften getroffen und deren Abhängigkeit von den zugrundeliegenden mikroskopischen Mechanismen untersucht werden (Kapitel 3 und 4). Der Ausgangspunkt dieser Arbeit ist dabei eine Modelldescription von ILC-Systemen, welche nur eine der ionischen Komponenten, d.h., entweder die Kationen oder die Anionen, explizit berücksichtigt. Diese sogenannten Koionen wechselwirken untereinander jedoch nicht mit dem reinen elektrostatischen Coulombpotential, denn ihre direkte elektrostatische Wechselwirkung wird durch eine „Ladungswolke“ aus (entgegengesetzt geladenen) Gegenionen abgeschirmt. Demnach werden die Gegenionen hier nur indirekt als ein strukturloses Hintergrundmedium

modelliert, welches eine Abschirmung der Ladungen der Koionen auf der Längenskala der Debye-Länge λ_D bewirkt. Die Koionen hingegen werden explizit als harte Ellipsoide mit einem Längen-zu-Breiten-Verhältnis von L/R dargestellt. Sie haben eine symmetrische Ladungsverteilung inne, d.h., sie besitzen zwei Ladungen jeweils im Abstand D von ihrem Zentrum entfernt (in Richtung der Längsachse), wie in Abb. 2.1 dargestellt. Somit werden hier ionische Flüssigkristalle in einem effektive Modell einer Teilchensorte wiedergegeben. Neben den eben erwähnten Beiträgen zum (totalen) Wechselwirkungspotentials durch die elektrostatische und „hard-core“ Wechselwirkung, interagieren die Teilchen zudem mittels dem sogenannten Gay-Berne-Potentials, welches die Anziehung benachbarter Moleküle durch Dispersions- und van-der-Waals-Kräfte imitieren soll.

Auf Grundlage dieses Modells wird im zweiten Teil von Kapitel 2 eine theoretische Beschreibung im Rahmen der Dichtefunktionaltheorie (DFT) entwickelt. Hierfür wird eine „weighted-density“-Formulierung, welche die „projizierte Dichte“ $\bar{\rho}$ (Gl. (2.12)) einführt, für das Exzess-Funktional $\beta\mathcal{F}[\rho]$ der freien Energie (Gl. (2.10)) gewählt. Die projizierte Dichte $\bar{\rho}$ ist eine Entwicklung der positions- und orientierungsabhängigen Dichteverteilung $\rho(\mathbf{r}, \boldsymbol{\omega})$ in einer Fourier- und Legendre-Reihe. Dieser Ansatz erlaubt es isotrope, nematische und smektisch-A Phasen, sowie (freie) Grenzflächen zwischen diesen zu studieren. Mittels dieser theoretischen Beschreibung werden in Kapitel 3 zunächst das Phasenverhalten von ionischen Flüssigkristallen und die strukturellen Eigenschaften der beobachteten Bulk-Phasen diskutiert. Abhängig vom Längen-zu-Breiten-Verhältnis L/R der Moleküle und den Positionen der Ladungen innerhalb der Moleküle, d.h., der molekularen Ladungsverteilung, zeigt sich ein vielfältiges Phasenverhalten. Für Teilchen mit $L/R = 2$ wird die gewöhnliche smektische S_A -Phase bei hohen Temperaturen und großen Dichten beobachtet (siehe Abb. 3.2). Hingegen, bei niedrigen Temperaturen und mittleren Dichten wird eine andere smektische Struktur beobachtet, welche als S_{AN} -Phase bezeichnet werden soll. Beide smektischen Phasen werden durch Phasenübergänge erster Ordnung von der isotropen Flüssigkeit separiert. Erstaunlicherweise besteht die S_{AN} -Phase aus Teilchen, die parallel zu den smektischen Schichten, d.h., senkrecht zur Schichtnormalen, ausgerichtet sind (siehe Abb. 3.7). Im Gegensatz zur S_A -Phase zeigen diese Teilchen keine bevorzugte Ausrichtung mit dem Direktor. (Abbildung 3.3 vergleicht die Strukturen beider smektischen Phasen S_A und S_{AN} .) Das Ausbilden einer weiteren smektischen Phasen S_{AN} mit geringerer Orientierungsordnung scheint mit dem kleinen Verhältnis von Länge zu Breite $L/R = 2$ und dem kleinen Wert des Anisotropieparameter $\varepsilon_R/\varepsilon_L = 2$ des zugrunde liegenden Gay-Berne-Potentials zusammenzuhängen. Dadurch erscheinen die Teilchen fast isotrop, was für ionische Flüssigkristalle noch ausgepräg-

ter ist, als für (ungeladene) gewöhnliche Flüssigkristalle des selben Längen-zu-Breiten-Verhältnisses, aufgrund der zusätzlichen elektrostatischen Abstoßung (siehe Abb. 3.2). Folglich ist die L - S_{AN} - S_A -Tripelpunkttemperatur in diesem Fall erhöht. Gleichwohl, im Bereich großer Dichten für den die flüssigkristallinen Phasen in diesen Systemen vorhergesagt werden, würde bei einer (exemplarisch gewählten) hexagonalen Gitterstruktur ein lateraler Gitterabstand von $a/R \leq 1.1$ auftreten (siehe Abschn. 3.2.3 und 3.3.1) und vorangegangene Simulationen (siehe Ref. [85]) deuten an, dass dort bereits Kristallisation einsetzt. Es kann daher erwartet werden, dass die thermodynamische Stabilität der flüssigkristallinen Phasen S_A und S_{AN} ein Artefakt der verwendeten DFT-Methode ist, da sie keine echten kristallinen Phasen wiedergeben kann (siehe oben). Ungeachtet dessen, kann die Vorhersage von diversen smektischen Phasen, die sich durch periodische Dichteprofile entlang der Schichtnormalen auszeichnen, ein Hinweis auf das Vorhandensein von verschiedenen Typen von kristallinen Phasen in diesen Systemen sein. Die S_A -Phase kann als Analogon zu einer kristallinen Phase mit zusätzlicher Orientierungsordnung gesehen werden, während die S_{AN} -Phase eine kristalline Phase mit einem niedrigeren Grad an Orientierungsordnung, d.h., plastische Kristalle, darstellt.

Für längere Teilchen mit $L/R = 4$ wird neben der isotropen Flüssigkeit und der gewöhnlichen smektischen S_A -Phase, bei niedrigen Temperaturen und hinreichend großen Dichten, die neue S_{AW} -Phase beobachtet (siehe Abb. 3.4 und 3.5). (Alle drei Phasen sind jeweils durch Phasenübergänge erster Ordnung von einander getrennt.) Die S_{AW} -Phase zeichnet sich durch einen deutlich *weiteren* Schichtabstand aus, als wie er in der gewöhnlichen S_A -Phase beobachtet wird (vergleiche Abb. 3.8 und 3.9). Während die Mehrzahl der Teilchen sich in den smektischen Schichten befindet und überwiegend parallel zur Schichtnormalen ausgerichtet ist, befindet sich eine kleinere aber nennenswerte Anzahl von Teilchen zwischen diesen Schichten und bevorzugt Orientierungen senkrecht zur Schichtnormalen. Werden die Ladungen der ILC-Moleküle in einen moderaten Abstand zum geometrischen Mittelpunkt gebracht, verändert sich das Phasenverhalten nicht wesentlich im Vergleich zu dem Fall, dass die Ladungen sich im Zentrum befinden (vergleiche Abb. 3.4(b) und 3.5(a)). Wenn sich die Ladungen jedoch nahe der Moleküleenden befinden (siehe Abb. 3.5(b)), tritt eine signifikante Veränderung des Phasenverhaltens auf. Die Koexistenz der Phasen S_{AW} und S_A wird in Richtung höherer Temperaturen verschoben. Diese Verschiebung stabilisiert die S_{AW} -Phase weiterhin in einem Temperaturbereich unterhalb der gewöhnlichen S_A -Phase, jedoch nun auch oberhalb der Schmelzkurve. Hingegen für alle anderen untersuchten Systeme ergibt eine Stabilitätsanalyse (siehe Abschn. 3.2.3), dass die S_{AW} -Phase erst im Bereich der Kristallisation auftreten würde

(Abb. 3.4 und 3.5(b)). Zusätzlich zu den bereits erwähnten DFT-Berechnungen wurden (großkanonische) Monte Carlo Simulationen eines ILC-Systems mit den Ladungen an den Molekülen durchgeführt. In qualitativer Übereinstimmung mit den DFT-Ergebnissen zeigen die Simulationen eine stabile S_A -Phase bei hohen Temperaturen und großen Dichten (siehe Abb. 3.10 und 3.11). Bemerkenswerterweise tritt bei niedrigeren Temperaturen in der Tat die neuartige S_{AW} -Phase mit großem Schichtabstand auf, so dass sich tatsächlich ein gewisser Teil der Moleküle zwischen den smektischen Schichten aufhält und vorzugsweise senkrecht zur Schichtnormalen ausgerichtet ist (siehe Abb. 3.6(b) und 3.12).

Die Analyse der Abhängigkeit des smektischen Schichtabstandes von der Temperatur im letzten Abschnitt von Kapitel 3 zeigt deutlich Unterschiede zwischen den Phasen S_A und S_{AW} (siehe Abb. 3.13): Während der Schichtabstand der gewöhnlichen smektischen S_A -Phase nicht wesentlich als Funktion der Temperatur variiert (dies ist eine typische Beobachtung für gewöhnliche smektische Phasen), kann für die S_{AW} -Phase ein zunehmender Schichtabstand bei abnehmender Temperatur beobachtet werden. Dies lässt sich anhand des Freiraumes zwischen den smektischen Schichten verstehen, der zu einer gewissen Flexibilität des Schichtabstandes führt. Durch die erhöhte effektive elektrostatische Abstoßung bei niedrigeren Temperaturen neigen die Schichten dazu, sich zu verbreitern. Jedoch zeigt sich diese ausgeprägte Abhängigkeit des Schichtabstandes von der Temperatur erst im metastabilen Bereich der S_{AW} -Phase.

Nachdem das Phasenverhalten von ILCs detailliert analysiert wurde, werden im anschließenden Kapitel 4 Grenzflächen zwischen den koexistierenden Phasen dieser Systeme untersucht. Die Diskussion konzentriert sich dabei auf zwei spezielle Exemplare von ionischen Flüssigkristallen: Zum einen, ILCs mit Ladungen im Zentrum der Moleküle und, zum anderen, Moleküle mit Ladungen an ihren Enden (in beiden Fällen gilt $L/R = 4$). Für diese Arten von ILCs zeichnen sich die entsprechenden Phasendiagramme (siehe Abb. 3.5) durch Phasenübergänge erster Ordnung von der isotropen Flüssigkeit L zu der gewöhnlichen smektischen S_A -Phase, beziehungsweise zu der weiten S_{AW} -Phase aus. In beiden Fällen, d.h., entweder für L - S_A - oder für L - S_{AW} -Koexistenz, wird eine planare Grenzfläche betrachtet, deren Geometrie durch den Neigungswinkel α zwischen der smektischen Schichtnormalen und der Grenzflächennormalen gekennzeichnet ist (siehe Abb. 4.1). Bei paralleler Ausrichtung der Schicht- und Grenzflächennormalen, d.h., $\alpha = 0$, werden Grenzflächenpositionen z_η und z_{S_2} , welche mit den Übergängen in der Struktur (welche durch das Grenzflächenprofil $\eta(\mathbf{r})$ der Packungsdichte) und in der Orientierungsordnung (beschrieben durch den Orientierungsordnungsparameter $S_2(\mathbf{r})$) ver-

bunden sind, beobachtet, die sehr nahe beieinander liegen (siehe Abb. 4.2-4.4). Somit verschwindet die Orientierungsordnung innerhalb der letzten smektischen Schicht und der Verlust der Orientierungsordnung geht unmittelbar mit dem Verschwinden der smektischen Schichtstruktur einher.

Interessanterweise zeigen sich für $\alpha = \pi/2$, d.h., die Schicht- und die Grenzflächennormale sind senkrecht zueinander, qualitative Veränderungen der Grenzflächeneigenschaften: Eine periodische Struktur der Grenzfläche in lateraler Richtung x ist zu beobachten. Dies ist eine direkte Folge der Periodizität der smektischen Phasen (siehe Abb. 4.5 und 4.6). Zudem beobachtet man für die L - S_A -Grenzfläche deutliche Abweichungen $(z_\eta - z_{S_2})/R \gtrsim 2$ in den Grenzflächenpositionen. Die (nahezu) parallele Ausrichtung der Teilchen in den S_A -Schichten bleibt somit auf einer Länge von einigen Teilchendurchmessern R in die flüssige Phase L hinein erhalten. Dies steht im Gegensatz zum Fall $\alpha = 0$, für den die Orientierungsordnung sofort mit dem Auflösen der Schichtstruktur verschwindet. Darüber hinaus beobachtet man für $\alpha = \pi/2$ eine strukturelle Veränderung der L - S_{AW} -Grenzfläche gegenüber der L - S_A -Grenzfläche. Während an den Ausläufern der S_{AW} -Hauptschichten ebenfalls eine in die flüssige Phase hinein bestehende Orientierungsordnung zu finden ist, zeigt sich an den Sekundärschichten, dass dort die Schichtstruktur weiter als die Orientierungsordnung in die L -Phase hinein besteht. Dieses gegenteilige Verhalten an den Haupt- und Sekundärschichten wird vermeintlich durch ihre jeweiligen Orientierungseigenschaften bestimmt. Während in den Hauptschichten der S_{AW} -Phase die Teilchen mit der Schichtnormalen nahezu ausgerichtet sind und daher einen effektiven Durchmesser in der y - z -Ebene aufweisen, der mit dem Teilchendurchmesser R vergleichbar ist, vermeiden die Teilchen in den Sekundärschichten Ausrichtungen parallel zur x -Achse (die Richtung der Schichtnormalen), was zu einem vergrößerten effektiven Radius führt, denn die Teilchen bevorzugen es parallel zur y - z -Ebene ausgerichtet zu sein. Bei Annäherung an die isotrope Flüssigkeit L erhöht sich somit der effektive Radius in den Hauptschichten, wohingegen er sich in den Sekundärschichten *verringert*.

Anschließend, im nächsten Abschnitt des Kapitels 4, wird das asymptotische Verhalten der L - S_A -Grenzfläche (für $\alpha = \pi/2$, d.h., die Schicht- und Grenzflächennormale sind orthogonal zueinander) mittels der logarithmischen Variationen $\ln |\eta(x, z) - \eta_L|$ und $\ln |S_2(x, z) - S_{2,L}|$ der Dichte und des Orientierungsordnungsparameters, um ihre jeweiligen Werte in der isotropen Flüssigkeit L , untersucht. Wenn sich die Ladungen im Zentrum der Moleküle befinden, ist die periodische Struktur der Grenzfläche sogar weit entfernt von ihr ($z/R < -20$) immer noch erkennbar (siehe Abb. 4.8). Umgekehrt,

wenn sich die Ladungen an den Molekülen befinden, variieren $\ln|\eta(x, z) - \eta_L|$ und $\ln|S_2(x, z) - S_{2,L}|$ nur marginal als Funktion der lateralen Koordinate x , weit entfernt von der Grenzfläche. Während für $D = 0$ die Ladungen stark in den Zentren der smektischen Schichten lokalisiert sind und daher die periodische Struktur hervorheben, sind die Ladungen für $D/R = 1.8$ weniger lokalisiert und gleichmäßiger entlang der lateralen x -Richtung verteilt.

Das asymptotische Verhalten der Grenzflächenprofile der untersuchten ILC-Systeme zeigt drei verschiedene Regime, die explizit den drei zugrundeliegenden Beiträgen zum Wechselwirkungspotential zugeordnet werden können. Bemerkenswerterweise, obwohl das Vorhandensein von Ladungen das entscheidende Charakteristikum von ILC-Materialien darstellt, bestimmt der elektrostatische Beitrag das asymptotische Verhalten lediglich bei mittleren Distanzen von der Grenzfläche (siehe Abb. 4.8). Nur in diesem Bereich wird die Abklinglänge eindeutig durch die Debye-Länge $\lambda_D/R = 5$ bestimmt. Letztlich ist es der attraktive Gay-Berne-Beitrag, der das asymptotische Verhalten weit entfernt von der Grenzfläche dominiert; dort wird weite große Abklinglänge $\xi_{GB}/R \approx 10 > 5 = \lambda_D/R$, welche dem Potenzgesetz des Gay-Berne-Potentials zugeordnet werden kann, beobachtet. Nahe der Grenzfläche ist es die hard-core Wechselwirkung, welche die Grenzflächenprofile der Dichte und des Orientierungsordnungsparameters bestimmt. Die entsprechende Abklinglänge $\xi_{PL}/R \approx 1.9$ ist mit dem Teilchendurchmesser R vergleichbar, denn die Moleküle bevorzugen Ausrichtungen senkrecht zur Grenzflächennormalen (für $\alpha = \pi/2$ in der S_A -Phase). Interessanterweise treten die Übergänge zwischen den drei verschiedenen Abklingregimen für $\ln|\eta(x, z) - \eta_L|$ und $\ln|S_2(x, z) - S_{2,L}|$ in jeweils unterschiedlichen Abständen zur Grenzfläche auf. Während alle drei Abklinglängen ξ_{PL} , ξ_{GB} und λ_D aus dem funktionellen Verlauf von $\ln|S_2(x, z) - S_{2,L}|$ ersichtlich sind (für beide betrachteten ILCs), ist für $\ln|\eta(x, z) - \eta_L|$ nur ein Abklingen mit der Länge λ_D im untersuchten Bereich zu beobachten. Dies wird durch die relativen Stärken der Abklingamplituden verursacht: Für das Packungsdichteprofil sind die Abklingamplituden aufgrund der Gay-Berne- und der hard-core Wechselwirkung, im Vergleich zur Amplitude durch die Elektrostatik, zu klein, um beobachtet werden zu können.

Abschließend wird auch die Abhängigkeit der Struktur und der Orientierungseigenschaften der untersuchten flüssig-smektischen Grenzflächen vom Neigungswinkel α zwischen der Grenzflächen- und Schichtnormalen diskutiert. Für die L - S_A -Grenzfläche (siehe Abb. 4.10(a)) stellt sich heraus, dass die parallele Ausrichtung der Gleichgewichtskonfiguration entspricht, d.h., $\alpha_{eq} = 0$, während die senkrechte Ausrichtung $\alpha = \pi/2$ metastabil ist. Interessanterweise geht die Erhöhung der Grenzflächenspannung $\Gamma^*(\alpha)$ um

$\alpha = \pi/2$ mit einer Erhöhung des Abstandes $z_\eta - z_{S_2}$ zwischen den Grenzflächenpositionen einher, was darauf hindeutet, dass die Aufrechterhaltung der lokalen Orientierungsordnung jenseits der smektischen Schichten freie Energie kostet. Folgerichtig, ist im Fall $\alpha = \alpha_{\text{eq}} = 0$, bei dem die Orientierungsordnung sofort mit dem Auflösen der smektischen Schichten verschwindet, die beobachtete Grenzflächenspannung am geringsten. Demzufolge liefert die vorliegende Theorie eine Erklärung der auftretenden Grenzflächenspannungen $\Gamma^*(\alpha)$ auf Grundlage der (mikroskopischen) Orientierungs- und Struktureigenschaften der ILC-Moleküle an der Grenzfläche. Für die L - S_{AW} -Grenzfläche ergibt sich ein vergleichbares Bild (siehe Abb. 4.10(b)). Wiederum entspricht der Gleichgewichts-Neigungswinkel $\alpha_{\text{eq}} = 0$ der parallelen Ausrichtung von Grenzflächen- und Schichtnormalen. Allerdings ist hier die Grenzflächenspannung $\Gamma^*(\alpha)$ um $\alpha = \pi/2$ (nahezu) flach als Funktion von α . Daher ist die senkrechte Ausrichtung in diesem Fall labil.

Summary

On one hand, the technological importance of ionic liquid crystals (ILCs) is based on their ability to form liquid-crystalline phases, so-called *mesophases*. On the other hand, ILCs are composed of ions and therefore can be used as media for charge transport. This combination of various nanostructures and charge carriers within ILC-materials makes them promising candidates for versatile applications, e.g., in energy storage and conversion devices such as high-performance batteries, fuel-cells or solar cells. Various types of ILCs have been synthesized until now. For example, different combinations of (charged) imidazolium rings and alkyl chains allow one to tune the aspect-ratio and the charge distribution of the ionic compounds. Thereby one is able to promote those distinctive properties of ILCs which are beneficial for particular technological applications. However, an in-depth understanding of the relation between the (intrinsic) molecular features and the resulting (macroscopic) properties of these materials is still lacking and demands further theoretical studies dedicated to this scientific field.

In this context, first, the present dissertation aims at developing a theoretical description of ILC systems which is applicable to bulk and interfacial systems (Chapter 2). Second, it aims at providing predictions and insights concerning the thermodynamic and structural properties as well as their connection to the underlying microscopic mechanisms (Chapters 3 and 4). The starting point of the present dissertation is an effective model of ILC systems in which only one of the ion species, i.e., either the cations or the anions, are explicitly incorporated. These so-called coions do, however, not interact among each other via the pure electrostatic Coulomb potential, but they are subject to a screened Coulomb interaction, because they are considered to be surrounded by a screening “charge cloud” composed of the (oppositely charged) counterions. This means that the counterions are indirectly incorporated as a structureless background medium, which gives rise to screening of the charges of the coions on the scale of the Debye-screening length λ_D . However, the coions are explicitly modeled as hard ellipsoids with a length-to-breadth ratio L/R carrying a symmetric charge distribution, i.e., they possess two charge sites, each of the two located at a distance D (in the direction of the long axis)

from the geometrical center, as it is shown in Fig. 2.1. Thus, here, ILCs are described effectively by a one-species model. Besides the hard-core and electrostatic repulsion, the particles additionally interact via the Gay-Berne potential, which mimics the attraction of neighboring molecules by dispersion and van der Waals-type forces.

In the second part of Chapter 2 a theoretical framework within density functional theory (DFT) is developed in order to study the aforementioned model of ionic liquid crystals. To that end, a weighted density formulation – via introducing the projected density $\bar{\rho}$ (Eq. (2.12)), which is an expansion of the position- and orientation-dependent number density distribution $\rho(\mathbf{r}, \boldsymbol{\omega})$, into a Fourier- and Legendre-series – is used for the evaluation of the excess free energy functional $\beta\mathcal{F}[\rho]$ (Eq. (2.10)). This approach allows one to study isotropic, nematic, and smectic-A phases. Moreover, it is constructed such that it is applicable to (free) interfaces between these types of bulk phases. Based on this DFT framework, in Chapter 3 at first the phase behavior of ILCs is studied in terms of the bulk phase diagrams. Furthermore, the structural and orientational properties of the corresponding bulk phases is analyzed. Depending on the length-to-breadth ratio L/R of the underlying particles and the loci of the charges, i.e., the molecular charge distribution, a rich phase behavior is observed. For particles with $L/R = 2$ there is an ordinary smectic-A phase (S_A) stable at sufficiently high temperatures and sufficiently large densities (see Fig. 3.2). Whereas at low temperatures and within an intermediate density regime, a distinct smectic-A structure, referred to as S_{AN} phase, occurs. Both kinds of smectic phases are separated from the isotropic liquid phase L by first-order phase transitions. Remarkably, unlike the ordinary S_A phase, the S_{AN} phase is characterized by layers in which the particles are oriented parallel to the smectic layers, i.e., perpendicular to the layer normal (see Fig. 3.7), and thus do not show a preferred orientation. (Figure 3.3 provides a comparison of the S_{AN} and S_A smectic structures.) The formation of the distinct smectic S_{AN} phase of less orientational order seems to be related to the small length-to-breadth ratio $L/R = 2$ and to the small value of the anisotropy parameter $\varepsilon_R/\varepsilon_L = 2$ of the underlying Gay-Berne pair potential. Thus, the particles are rather isotropic which is even more pronounced in the case of an ILC fluid, compared to an (uncharged) ordinary liquid crystal of the same length-to-breadth ratio $L/R = 2$, due to the additional electrostatic repulsion (see Fig. 3.2). This leads to a higher L - S_{AN} - S_A triple point temperature. Nevertheless, it turns out that the (high) densities, at which the liquid-crystalline phases are predicted to occur in these systems, for an exemplary hexagonal lattice structure, lead to a lateral lattice spacing $a/R \leq 1.1$ (see Secs. 3.2.3 and 3.3.1); previous simulations (see Ref. [85]) report the onset of crystal-

lization within that regime. On this basis, at least in parts, the thermodynamic stability of the liquid-crystalline phases S_A and S_{AN} can be expected to be an artifact of the DFT method employed, which cannot capture genuine crystalline phases (see above). The occurrence of distinct types of smectic phases, which show periodically varying density distributions in the direction parallel to the layer normal, can be a hint at the presence of various types of crystalline phases in these systems. The S_A phase can be interpreted as an analogue of a crystalline phase with additional orientational ordering, while the S_{AN} phase mimics a crystalline phase with a lower degree of orientational ordering, i.e., plastic crystals. For longer particles of length-to-breadth ratio $L/R = 4$, besides the isotropic liquid and the ordinary smectic S_A phase, at low temperatures and sufficiently large densities the novel S_{AW} phase occurs (see Figs. 3.4 and 3.5). (All three of them are separated by first-order phase transitions.) The S_{AW} phase is characterized by a considerably *wider* layer spacing as compared to the ordinary S_A phase (compare Figs. 3.8 and 3.9). While the majority of particles is located within the smectic layers of the S_{AW} phase and exhibit orientations (mostly) parallel to the smectic layer normal, a smaller but considerable number of particles is located in between the smectic layers and prefer orientations perpendicular to the layer normal.

Concerning the phase behavior of ILCs as function of the location of the charges in the molecules, positioning the charges at intermediate distances from the geometric center does not alter the phase behavior much as compared to positioning the charges in the center (see Figs. 3.4(b) and 3.5(a)). However, if the charges are located very close to the tips of the ILC molecules (Fig. 3.5(b)), the phase behavior changes significantly. The coexistence of the phases S_{AW} and S_A is shifted towards higher temperatures. This shift stabilizes the S_{AW} phase in a temperature regime below the ordinary S_A phase but above the melting curve, unlike the other cases studied (see Figs. 3.4 and 3.5(b)), for which a crystallization stability analysis (see Sec. 3.2.3) shows that the S_{AW} phase is expected to be preempted by crystallization. In addition to the DFT calculations, (grand canonical) Monte Carlo simulations have been performed for an ILC system with charges at the tips of the molecules. In qualitative agreement with DFT, the simulations yield an ordinary smectic S_A phase at high temperatures and large densities (see Figs. 3.10 and 3.11). Remarkably, at lower temperatures, indeed the novel S_{AW} phase with wide layer spacing occurs, such that, in fact, a considerable fraction of particles is located in between the smectic layers with mainly perpendicular orientations with respect to the layer normal (see Figs. 3.6(b) and 3.12).

In the final section of Chapter 3 the dependence of the (bulk) smectic layer spacing

on temperature is investigated. Interestingly, this analysis reveals distinct behaviors of the smectic S_A and S_{AW} phases (see Fig. 3.13). While the layer spacing of the ordinary smectic S_A phase does not vary notably as function of temperature, which is a common finding for ordinary S_A phases, increasing layer spacings for decreasing temperatures can be observed for the low-temperature smectic phase S_{AW} . This can be understood in terms of the free space in between the smectic layers, which gives rise to a certain softness in the layer spacing. Due to the enhanced effective electrostatic repulsion at lower temperatures, the layers tend to widen upon lowering the temperature. Yet, this behavior is prominent only in the metastable region of the S_{AW} phase, while within the stable region of the S_{AW} phase, in analogy to the high-temperature S_A phase, there is no pronounced temperature dependence of the layer spacing.

Having analyzed in detail the phase behavior of ILCs, subsequently, in Chapter 4, interfaces between the coexisting bulk states are studied. To this end, the discussion focuses on two particular kinds of the aforementioned ILCs: First, ILC molecules with charges in the center and, second, molecules with charges at the tips (in both cases $L/R = 4$). Recall, that for those types of ILCs the respective phase diagrams (see Fig. 3.5) are characterized by first-order phase transitions from the isotropic liquid L to the ordinary smectic-A phase S_A , respectively towards the S_{AW} phase. For both cases, i.e., either for L - S_A or for L - S_{AW} coexistence, a planar interface is considered, the geometry of which is characterized by the tilt angle α between the (bulk) smectic layer normal and the interface normal (see Fig. 4.1). A parallel orientation of the smectic layer normal and the interface normal, i.e., $\alpha = 0$, leads to interface positions z_η and z_{S_2} , associated with the transitions in the structure (described by the packing fraction interface profile $\eta(\mathbf{r})$) and in the orientational order (described by the orientational order parameter profile $S_2(\mathbf{r})$), which are very close to each other (see Figs. 4.2-4.4), such that the orientational order vanishes within the last smectic layer for $\alpha = 0$. Thus, for $\alpha = 0$, it turns out that the loss of orientational order coincides with the disappearance of the smectic layer structure at the interface to the isotropic liquid. Interestingly, $\alpha = \pi/2$, i.e., the smectic layer normal and the interface normal are perpendicular to each other, leads to qualitative changes in the interfacial properties: A periodic structure of the interface in lateral direction x can be observed, which is a direct consequence of the periodicity of the bulk smectic-A phases (see Figs. 4.5 and 4.6). For the L - S_A interface, one observes considerable deviations $(z_\eta - z_{S_2})/R \gtrsim 2$ in the interface positions. Thus, the (nearly) parallel orientations of particles in the S_A layers persists a few particle diameters R into the liquid phase L , unlike in the case $\alpha = 0$ in which the orientational order vanishes

instantaneously with the breakdown of the S_A layer structure at the interface, i.e., within the last smectic layer. For $\alpha = \pi/2$ one observes a qualitative change in the interfacial structure for the L - S_{AW} interface compared to the L - S_A interface. While at the tails of the S_{AW} main layers the interface also features an orientational order which persists into the liquid phase L , at the tails of the secondary layers it is the layer structure which persists more than the orientational order. The opposite behavior at the main and secondary S_{AW} layers is presumably driven by their respective orientational properties. In the main layers the particles are well aligned with the smectic layer normal and therefore show an effective diameter in the y - z -plane which is comparable to the particle diameter R . However, in the secondary layers the particles avoid orientations parallel to the x -axis (i.e., the direction of the layer normal), giving rise to an considerably larger effective radius, because the particles prefer to be parallel to y - z -plane. Thus, by approaching the liquid L , this effective radius *increases* for the case of the main layers, whereas it *decreases* for the secondary layers.

Subsequently, in the next section of Chapter 4, the asymptotic behavior of the L - S_A interface (for $\alpha = \pi/2$, i.e., the layer normal and the interface normal are orthogonal) is studied in terms of the logarithmic deviations $\ln|\eta(x, z) - \eta_L|$ and $\ln|S_2(x, z) - S_{2,L}|$ of the density and of the orientational order parameter from their respective values in the isotropic bulk. If the charges are located in the center, the periodic structure of the interface is apparent even at far distances $z/R < -20$ from the L - S_A interface (see Fig. 4.8). Conversely, if the charges are at the tips, $\ln|\eta(x, z) - \eta_L|$ and $\ln|S_2(x, z) - S_{2,L}|$ vary only marginally as function of the lateral coordinate x far from the interface. While for $D = 0$ the charges are strongly localized at the centers of the smectic layers, promoting the periodic structure, for $D/R = 1.8$ the charges are less localized and more distributed along the lateral x -direction.

The asymptotic decays towards the isotropic liquid L of the interface profiles for ILCs show an interesting and rich behavior, because one observes three distinct regimes, which can be associated explicitly with the three underlying contributions to the pair interaction potential. Notably, although it is the presence of charges which is the distinctive property of ILC materials, the (screened) electrostatic contribution determines the asymptotic decay only at intermediate distances from the interface, cf., Fig. 4.8. In this regime, clearly, the decay length is determined by the Debye screening length $\lambda_D/R = 5$. Nonetheless, ultimately, it is the attractive Gay-Berne contribution which dominates the outermost asymptotic behavior; a considerably large decay length $\xi_{GB}/R \approx 10 > 5 = \lambda_D/R$ is observed, which results from the truncated power law decay of the potential.

Close to the interface it is the hard-core interaction which determines the interface profiles of the density and of the orientational order parameter. Thus, the corresponding decay length $\xi_{\text{PL}}/R \approx 1.9$ is comparable to the particle diameter R , because the particles are oriented preferentially perpendicular to the interface normal for $\alpha = \pi/2$ in the S_A phase. Interestingly, the crossovers between the three different decay regimes occur at distinct distances for $\ln |\eta(x, z) - \eta_L|$ and $\ln |S_2(x, z) - S_{2,L}|$. While all three decay lengths ξ_{PL} , ξ_{GB} , and λ_D are apparent from $\ln |S_2(x, z) - S_{2,L}|$ for both considered types of ILCs, for $\ln |\eta(x, z) - \eta_L|$ only the decay length λ_D is observable within the investigated range. This is caused by the relative magnitudes of the respective decay amplitudes: For the packing fraction profile the decay amplitudes due to the Gay-Berne and the hard-core interaction are too small (compared to the amplitude due to the electrostatic interaction) to be observable.

Finally, the dependence of the structural and orientational properties of liquid-smectic interfaces on the tilt angle α between the interface normal and the smectic layer normal is discussed as well. For the L - S_A interface (see Fig. 4.10(a)) it turns out that the parallel orientation of the interface normal and smectic layer normal is the one in thermal equilibrium, i.e., $\alpha_{\text{eq}} = 0$, whereas the perpendicular orientation $\alpha = \pi/2$ is metastable. Interestingly, the increase in the interfacial tension $\Gamma^*(\alpha)$ around $\alpha = \pi/2$ is accompanied by an increase of the distance $z_\eta - z_{S_2}$ between the structural and orientational interface positions, suggesting that maintaining the local orientational order beyond the smectic layers costs free energy. Consistently, in the case $\alpha = \alpha_{\text{eq}} = 0$, for which the orientational order immediately vanishes with the disappearance of the smectic layers, the cost of free energy is lowest. Thus, the present theory provides an explanation for the observed behavior of the interfacial tensions $\Gamma^*(\alpha)$ in terms of the (microscopic) orientational and structural properties of the ILC molecules at the interface. Similar results are obtained for the L - S_{AW} interface (see Fig. 4.10(b)). Again, the equilibrium tilt angle $\alpha_{\text{eq}} = 0$ corresponds to the parallel orientation of the interface and smectic layer normal. However, here around $\alpha = \pi/2$ the interfacial tension $\Gamma^*(\alpha)$ is (merely) flat as function of α , and therefore the perpendicular orientation is labile in this case.

GENERAL INTRODUCTION

A general introduction to the field of ionic liquid crystals (ILCs) is provided. Particular attention is paid to their technological importance as well as the 'state of the art' concerning the development of theoretical models and the understanding of ILC-systems. In this context the aim of the present dissertation is formulated.

1.1. Studies on ionic liquid crystals and the aim of the present work

The term '*ionic liquid crystal*' is composed of two parts, that refer to two distinct classes of physical systems: The latter, i.e., *liquid crystal*, relates to the vast field of soft matter built of molecules which show elongated or prolate molecular shapes, giving rise to the occurrence of so-called *mesophases* [4]. Mesophases are states of matter in between the isotropic fluid, in which the molecules are homogeneously distributed in space and do not show any preferred orientation, and the crystalline phases characterized by long-range correlations among the positions and the orientations of particles. While the isotropic fluid and crystal structures are of course also observable in systems of spherical particles [5], it is the presence of orientational degrees of freedom that leads to the emergence of mesophases.

Until the present day a vast amount of these liquid-crystalline phases has been discovered and they are typically categorized by the degree of their microscopic ordering [4]: The nematic phase is spatially homogeneous, like the isotropic fluid, but the liquid crystal molecules (typically referred to as *mesogenes*) show a preferred orientation, described by the director of the nematic fluid. By either lowering the temperature or raising the molar concentration of mesogenes further mesophases are observable, associated to the formation of spatial ordering. For elongated molecules (*calamitic* mesogenes), e.g., rod-like or ellipsoidal particles, smectic phases occur, in which the molecules form layers. Typically, within the layers the particles are well aligned with each other and depending on the relative orientation of the director with respect to the smectic layer normal, one distinguishes between the smectic-A phase, the layer normal and director of which are parallel, and the smectic-C phase, in which the director is tilted with respect to the layer normal. Importantly, both of these smectic phases do not show long-range spatial ordering in lateral directions (i.e., within the smectic layers). This is why smectic layers are sometimes denoted as two-dimensional fluids [4].

Whereas, if the molecules in the layers are ordered in a hexagonal lattice, such that the correlations among the bond orientations are long-ranged but the positional order is still short-ranged, this is referred to as the smectic-B phase or 'hexatic' smectic phase, relating to the hexatic phase which is well-known to occur in 2-dimensional hard disk systems [6–9]. Though, the lateral order differs among these different types of smectic phases and, in particular, the smectic-B phase is the closest to a truly crystalline structure, all of

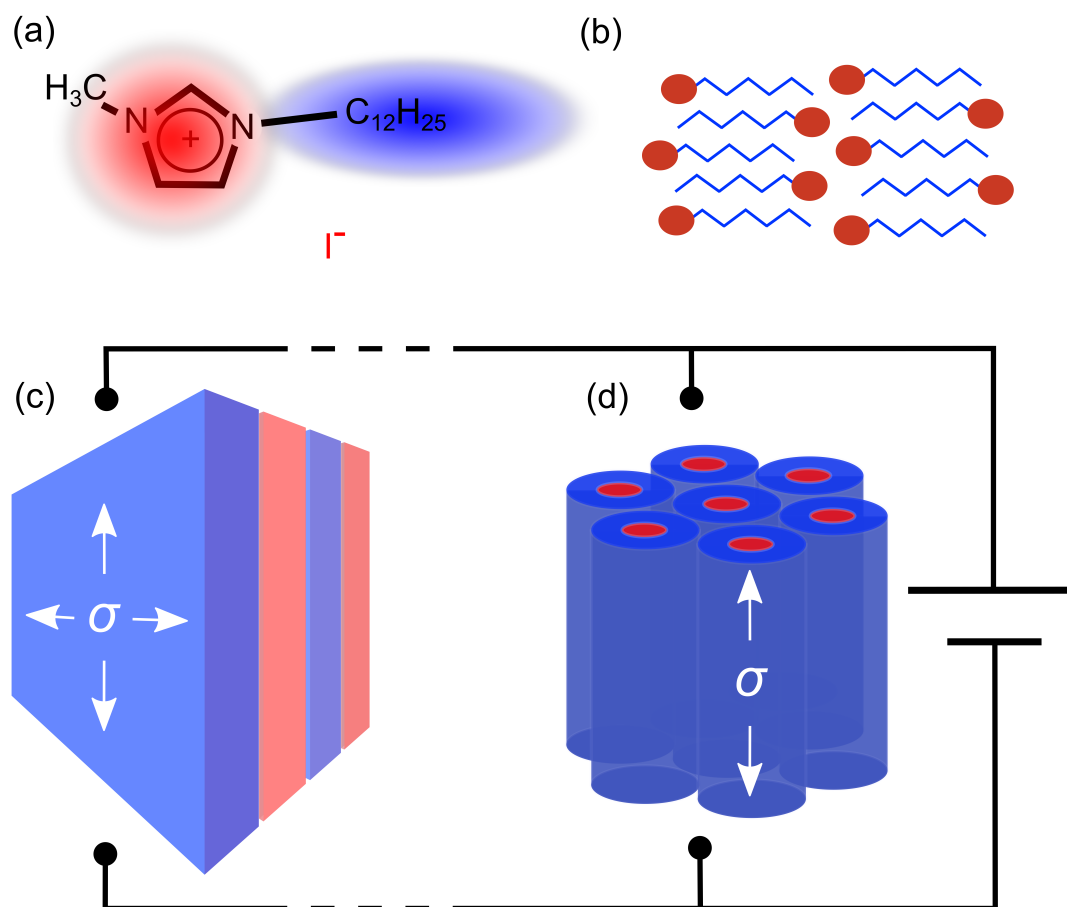


FIGURE 1.1.: 1-dodecyl-3-methylimidazolium iodide as a generic example of an ionic liquid crystal (ILC) is shown in panel (a). The charged imidazolium-ring is localized close to one of the ends of the mesogenic cation. Due to its long alkyl chains, highlighted by blue background in (a), the cations are able to form a smectic-A phase, as shown in (b), in which the charged groups, highlighted in red, orient themselves alternately towards both ends of the smectic layers. This is called an *interdigitated bilayer structure* [1,2]. The smaller iodide (I^-) anions are then located in between the smectic layers and due to the formation of these (2-dimensional) “pathways” in between the smectic layers an enhanced conductivity σ is observable parallel to the smectic layers, cf., panel (c). ILCs composed of molecules of a disk-like shape, cf., [3], can form columnar phases and here an enhanced conductivity is measurable in the direction of the stack structures (1-dimensional pathway) as shown in panel (d).

them share a low interplane shear elastic constant [4, 10], i.e., neighboring smectic layers can rather easily be sheared against each other, unlike crystals which show large shear-moduli in all directions.

While the occurrence of smectic phases is typical for calamitic mesogenes, a plate-like molecular shape (*discotic* mesogenes) advances the formation of columnar phases in which the mesogenes form stack-like structures [11, 12]. Familiar examples of discotic mesogenes are clay particles [13] or blood cells. As a last point concerning liquid crystals it is important to point out that a sufficient degree of rotational symmetry around one molecular axis is indispensable for the occurrence of meso- or macroscopical orientational ordering, because an arbitrary anisotropic molecular structure, without a sufficient (1-dimensional) rotational symmetry, in general does not lead to the emergence of mesophases.

The term '*ionic*' refers, at first glance, to a completely different type of physical system, namely fluids containing cations and anions. Common examples are electrolyte solutions or molten salts. While the latter is a pure ionic system, composed solely of ions, electrolyte solutions additionally contain water leading to the dissociation of salt into its ionic compounds. A key feature of such (charged) fluids is the motility of the ions giving rise to ionic conductivity. This mechanism is used for energy transport in various technological applications for example in batteries or fuel cells.

In ionic systems electrostatic interactions of the ions via the Coulomb potential are present. The potential's $1/(\text{distance})$ -decay renders it particularly long-ranged and leads to remarkable consequences: For instance, the thermodynamic limit might even depend on the geometry of the ionic system if the global charge Q increases as $\mathcal{V}^{3/2}$ or faster with the system volume \mathcal{V} [14, 15]. Accordingly this affects systems that carry a sufficiently strong (global) net charge. However even for the case of a globally charge neutral system interesting and distinct implications follow from the presence of the Coulomb interaction: One can show that the Stillinger-Lovett sum rules [16–20] are valid in ionic fluids. These are conditions that have to be fulfilled by the corresponding ionic pair distribution functions. Furthermore, it is an ongoing debate, whether the long range or the valency dependence of the Coulomb interaction is decisive for the properties of ionic fluids. Some evidence points towards the valency dependence to be the key property because experiments [21–24] as well as simulations [25–27] suggest that the critical behavior of ionic fluids is reminiscent of the Ising universality class, which comprises physical systems with short-range (nearest-neighbor) interactions. In addition to that there exist short-range (valency-dependent) interaction potentials that give rise to a similar phase

behavior compared to Coulombic fluids and also fulfill the Stillinger-Lovett perfect-screening property [28].

These peculiarities render the development of quantitatively reliable theoretical predictions a long-lasting challenge in this field [29,30]. While for dilute electrolyte solutions Debye-Hückel theory is a reasonable starting point [5,30,31], for dense ionic fluids further mechanisms like ion pairing [16,18], that is the binding of neighboring cat- and anions to form dipolar entities, are relevant and need to be accounted for by any reliable theoretical description. In this context an interesting question has been raised concerning the structure of dense ionic liquids: Is the majority of ions bound in (dipolar) ion pairs while only a small amount remains “free”, such that ionic liquids are similar to dilute electrolytes, or are they highly concentrated melts of cat- and anions in which only a small amount of them form dipolar entities? Addressing this question, first experimental studies [32] measured an astonishing large Debye screening length of the order of 10 nm, which indicates a weak screening. It was suggested that a considerable amount of ions are (temporarily) paired and therefore they act as an effective dipolar solvent while only a few (motile) ions participate in screening electrostatic fields, in analogy to dilute electrolytes. On the contrary, theory [33] based on a mean-field description of a mixture of free ions and ion pairs, being in chemical equilibrium, predicts that the majority of ions stays free and the corresponding Debye screening length is even smaller than the size of the ions, a consequence of an actually very strong screening. They argued that the experimental results might be dubious because a gold surface was used, which renders the determination of the Debye screening length nontrivial due to the complex surface morphology of gold in contact with an electrolyte. Another interesting and yet puzzling phenomenon observable for dense ionic fluids is the effect of underscreening. In contrast to Debye-Hückel theory which predicts a decreasing screening length with increasing ion concentration, an “anomalous” large screening length is observed in experiments [34,35] on concentrated electrolytes. While no satisfying theoretical concept concerning the effect of underscreening has been developed so far, it has been speculated that the high density in these electrolytes leads to rather immotile molecular structures. Similar to ionic crystals in which the cat- and anions are bonded to lattice sites and only defects of these sublattices are free to move, the density entering in the Debye screening length might be an effective one, arising from defects in the dense structure of concentrated electrolytes, instead of the pure ionic strength as most of the ions are immotile [35].

As set out above the term ‘ionic liquid crystals’ adverts on materials that combine properties from both of the two aforementioned physical fields: Ionic liquid crystals

(ILCs) merge characteristics of liquid crystals and ionic liquids such as anisotropic material properties and ionic conductivity, respectively [1,36]. A generic molecular structure of ILCs is that of (charged) imidazolium rings with alkyl chains attached, cf., Fig. 1.1(a). Varying the length of the organic chains as well as the number and loci of the charged groups offers the possibility to tune (and optimize) material properties during synthesis [1]. For instance, ILCs forming either columnar or smectic phases can show a low-dimensional high conductivity, because the smectic, respectively columnar microstructure of the mesogenes opens up pathways for the charge carriers and thereby increases the conductivity either perpendicular to the smectic layer normal, cf., Fig. 1.1(b) and (c), or parallel to the columnar stacks (see Fig. 1.1(d)). Thus potential applications as anisotropic electrolytes, e.g., in batteries are conceivable [3,37,38]. Moreover, ILCs can be synthesized such that they exhibit high thermal as well as mechanical stability [1,36]. The combination of (low-dimensional) high conductivity and durability renders ILCs promising candidates as electrolyte constituents for example in solar cells [2,39]. They can also be used as organized reaction media [36,40] which, due to their nanostructure, facilitate chemical reactions or offer a higher degree of control over the reactions.

Nonetheless, the technological use of ILCs requires an in-depth understanding of the microscopical mechanisms: In particular the interplay of molecular shape-anisotropy and the presence of charges needs to be understood. Theoretical studies, which incorporate anisotropic charged particles and which allow one to vary molecular properties like the aspect-ratio or the charge distribution within the molecules, might elucidate the role these microscopic properties play for the remarkable (macroscopic) features of ILCs.

Previous theoretical studies mainly focused either on the effect of molecular shape-anisotropy on thermodynamic properties or on ionic liquids within simplistic models. Regarding the latter, for instance, the *restricted primitive model* (RPM) considers only two ionic species: Two types of uniformly charged hard spheres of the same size and the same charge strength but opposite charge sign. Though the RPM has been studied intensively in the past [28,41–44], it is limited to the study of gross features such as the nature of criticality [25,29,43–46].

Likewise, there is a substantial number of theoretical studies about ordinary (un-charged) liquid crystals, which are based on anisotropic pair potentials [47–56] characterizing the underlying mesogenes. A huge diversity of mesophases can be observed, depending on the effective shape of the particles and their interaction potentials. This distinct behavior due to the molecular anisotropy gives rise to macroscopically measurable optical and mechanical anisotropies of liquid-crystalline materials and drives phe-

nomena like self-assembly or nano-structuring on microscopic scales [57–59]. However, while the anisotropic molecular shape gives rise to a fascinating richness of thermodynamic phases and microstructures to occur in liquid-crystalline systems, it renders their theoretical and computational treatment a complex and subtle challenge. On that score studies [47, 48, 60–62] on liquid crystals are typically based on simplified and effective descriptions of these systems, including, i.a., coarse-grained representations, e.g., as rods, ellipsoids or discs, of the underlying anisotropic molecules. In addition further features of the molecules such as side-chains or charged groups along the backbone of the mesogenes have mostly been disregarded due to the resulting gain in complexity.

In that regard, ILCs are such kinds of particularly complex physical systems for which it is the very interplay of shape-anisotropy and electrostatic interactions that gives rise to the vast phenomenology observed for ILC materials. Establishing a theoretical framework, which is applicable to this kind of materials and which provides a deeper understanding of the origin of their properties, is an ongoing process. Recently, Goossens et al. discussed in their review article [36] the latest developments in characterization, synthesis, and applications of ILCs. It was concluded that the effect of the molecular size, the shape, and the charge distribution on the (macroscopic) properties of those materials is yet not fully understood. In this context, the aim of the present dissertation is, first, to demonstrate that the considered molecular model of ILCs, incorporating orientational degrees of freedom as well as an anisotropic charge distribution, gives rise to a phenomenology concerning the phase behavior and the structural properties of the bulk phases, which is much richer than the one of simpler models of spherical ions or of ordinary liquid crystals. Second, to extent this analysis to inhomogeneous systems of ILCs. Within the scope of this dissertation the particular case of (free) interfaces between coexisting bulk phases is studied in order to gain insights on how the bulk structure and orientational properties are altered by the presence of inhomogeneities, such as free interfaces. Moreover, the theoretical methodology is formulated in a generic way and can be extended to further inhomogeneous systems, e.g., an ILC-electrolyte in contact with an electrode. Thus, this work can also serve as a starting point for future (theoretical) studies on ionic liquid crystals.

The thesis is structured as follows: The molecular model which is used to describe ILC systems throughout this work as well as the employed density functional theory (see below) framework are unrolled and explained in detail in Chapter 2. Afterwards, in Chapter 3, this framework is applied to bulk systems of ionic liquid crystals. Additionally, the theoretical predictions are tested against grand canonical Monte Carlo

simulations. In Chapter 4 inhomogeneous systems of ionic liquid crystals are studied. In particular, free interfaces between the coexisting bulk phases, obtained in Chapter 3, are considered. Finally, conclusions based on the present findings are drawn and an outlook on potential future studies related to the present thesis is provided (Chapter 5).

As set out above, the present study is based on the theoretical framework of *classical density functional theory*. In order to provide some of the conceptual ideas of this widely used method within the field of theoretical statistical physics of classical systems, the next section of this introductory chapter is devoted to the basics of classical DFT. Although, it cannot be regarded as a comprehensive review, the subsequent section presents the relevant DFT terminology, which is adopted throughout this thesis, in particular in Sec. 2.2.

Conclusively, it is expressly declared that parts of this thesis have been published in Refs. [63, 64] beforehand.

1.2. Basic concepts of classical density functional theory (DFT)

Classical density functional theory (DFT) [65] has become a standard technique in the context of theoretical studies on soft matter. For soft matter systems a treatment of equilibrium phenomena within the general framework of statistical mechanics is typically not feasible, because the corresponding partition functions are too involved to be computed, due to the various types of body interactions among the constituent particles. While simulational methods, such as Monte Carlo simulations, rely on sampling the corresponding configurational space efficiently, using methods such as importance sampling [66, 67], DFT follows a different route. Within DFT the specific calculation of the partition function can be avoided. Instead the corresponding grand potential functional has to be minimized with respect to all realizable density profiles; its minimum corresponds to the equilibrium density profile. (A detailed overview and derivation of the basic concepts of (classical) DFT can be found in Ref. [65].) A general representation of the grand potential functional is given by

$$\beta\Omega[\varrho] = \int d^d x \varrho(\mathbf{x})(\ln(\varrho(\mathbf{x})v) - 1) + \beta\mathcal{F}[\varrho] - \beta\mu \int d^d x \varrho(\mathbf{x}), \quad (1.1)$$

where the first term is the ideal gas contribution to the Helmholtz free energy and the second term, i.e., $\beta\mathcal{F}[\varrho]$, represents its excess contribution that incorporates the interaction between the constituent particles. $\beta = 1/(kT)$ denotes the inverse thermal energy and μ the chemical potential. Note, that in Eq. (1.1) a general notation is used, such that the integrals run over the d -dimensional configurational space, which is determined by the underlying degrees of freedom. For the scope of this dissertation $d = 5$, because the configurational space renders 3 spatial and 2 orientational degrees of freedom. Therefore the vector $\mathbf{x} = (\mathbf{r}, \boldsymbol{\omega})$ covers the (3-dimensional) position vector \mathbf{r} and the (2-dimensional) orientation vector $\boldsymbol{\omega}$ (describing the position and the orientation of a uniaxial particle). The quantity v has the dimension of a d -dimensional volume and it is called the *thermal de Broglie volume*. It originates from the kinetic degrees of freedom that can be integrated out beforehand [5]. For the relevant case of uniaxial particles in 3 spatial dimensions $v = 4\pi\Lambda^3$ with the *thermal de Broglie wavelength* Λ . The aforementioned statement that in equilibrium the grand potential is minimized, in the formalism of DFT can be expressed by [65]

$$\frac{\delta\beta\Omega[\varrho]}{\delta\varrho(\mathbf{x})} = 0, \quad (1.2)$$

i.e., the functional derivative of $\beta\Omega[\varrho]$ (Eq. (1.1)) with respect to the density $\varrho(\mathbf{x})$ vanishes. It has been pointed out above that the excess contribution $\mathcal{F}[\varrho]$ to the Helmholtz free energy is the characterizing quantity of the particle interactions. In units of kT it can generically be written as

$$\beta\mathcal{F}[\varrho] = \int d^d x \varrho(\mathbf{x})\beta\psi(\mathbf{x}, [\varrho]). \quad (1.3)$$

$\psi(\mathbf{x}, [\varrho])$ is the so-called *effective one-particle potential* that acts on a particle at \mathbf{x} , due to the presence of all the other remaining particles. It is not only function of \mathbf{x} , but additionally it is, in general, a functional of the density $\varrho(\mathbf{x})$, accounting for non-local effects due to the correlations among the particles. Analogously to the complex structure of the partition function, due to the pair interactions, in general, an exact expression for the excess free energy \mathcal{F} is not known. (From Eq. (1.3) it follows that this statement is equivalent to the statement that the effective one-particle potential $\psi(\mathbf{x}, [\varrho])$ is unknown.) Nevertheless, the above reformulation of statistical mechanics in terms of Eqs. (1.1) and (1.2) allows one to explicitly identify \mathcal{F} , respectively $\psi(\mathbf{x})$, as the remaining unknown quantity. Furthermore, guided by physical intuition about the nature of

the particle interactions, appropriate approximations to $\mathcal{F}[\varrho]$ can be constructed. As a generic example one can think of hard particle systems for which only the accessible space of any test particle is restricted due to the presence of the other (hard) particles which is frequently referred to as *excluded volume* effects [5]. In that regard, the geometrical properties of the particles are essential and this knowledge can be used to find appropriate approximations to the excess free energy functional \mathcal{F} [68–70].

Until the present day, DFT methods are well studied and various approximations to the excess free energy suited for all kinds of systems are available. Frequently, the excess free energy itself is subdivided into a reference and an excess part, separating the strongly repulsive steric interactions in realistic soft matter systems (typically modeled by hard-core potentials, see above) from the pair interactions that reach beyond contact of neighboring particles [5]. The benefit of such a treatment is, that while one needs to use sophisticated methods to sufficiently describe the hard-core interactions in order to account properly for the pronounced correlation effects, i.a., layering and packing effects, at short distances, for the longer-ranged interactions such an involved treatment is typically not necessary. Hence, they are often incorporated via mean-field like descriptions in a perturbative manner. This subdivision of the excess free energy is an adequate structure of the theoretical description of such systems.

In fact, the presence of correlations between the constituent particles is the driving mechanism for the complexity of any liquid state theory. In that regard, the simplest type of (approximate) excess free energy functionals is the class of the *local density approximation* (LDA) [65]. The LDA does not incorporate any correlations at all, which is directly linked to its purely local nature. This is reflected by the fact that for any LDA functional the effective one-particle potential $\psi_{\text{LDA}} := \psi(\mathbf{x}, \varrho)$ is a function of the local density $\varrho(\mathbf{x})$, instead of being a functional of $\varrho(\mathbf{x})$. Nevertheless, LDA represents an important class of approximate functionals, because it allows the study of the phase behavior of the considered model system. In fact, for any thermodynamic equation of state a corresponding LDA-functional can be obtained. Beyond local density approximation reaches the *square-gradient approximation* (SGA) that additionally incorporates gradient terms and therefore represents a semi-local description that is applicable to inhomogeneous fluid systems with long wavelength variations in the density. Furthermore, because for homogeneous (bulk) systems there are no density variations, all free energy contributions due to gradient terms vanish. Thus, the phase behavior obtained within SGA coincides with the one obtained by the corresponding LDA. Within SGA correlations can be indeed observed however, they decay monotonically, thus no packing

effects are observable. In order to resolve considerable density variations, e.g., close to a hard wall or in the vicinity of a test particle, one needs to consider non-local density functionals. One route is to expand the correlation terms of the excess free energy functional in a power series of the density. This represents a reasonable extrapolation of the ideal gas behavior for small densities. Truncating such a power series at second order gives rise to the famous second-order virial expansion. Here the non-locality is embodied by a convolution of the local density and the famous Mayer f-function. While this treatment is capable of qualitatively reproducing oscillatory density profiles at higher densities, the quantitative agreement with corresponding results by simulations or experiments is poor. In principle, this can be overcome by including successively higher order terms $\mathcal{O}(\rho^n)$, where $n \geq 3$, which however is practically not feasible anymore at sufficiently large densities. Nevertheless, it is worth mentioning that the second order virial expansion turns out to be exact in the particular case of infinitely long rods [47].

At present, the quantitatively best results compared to simulations and experiments are obtained by so-called *weighted-density approximations* (WDA) [5, 68, 70]. These are effective descriptions of the excess free energy functional. In particular, the effective one-particle potential $\psi_{\text{WDA}} := \psi(\mathbf{x}, \bar{\rho})$ depends on a so-called *weighted density* $\bar{\rho}(\mathbf{x})$. $\bar{\rho}(\mathbf{x})$ can be regarded as a smoothed density distribution which smears out the (narrow) peaks of the actual density $\rho(\mathbf{x})$. Thus the weighted density $\bar{\rho}(\mathbf{x})$ is evaluated non-locally. Typically one includes information about the geometrical properties of the particles into the particular form of the weighted density $\bar{\rho}(\mathbf{x})$ in terms of a set of weight functions, which is commonly referred to as *fundamental measure theory*. These sophisticated DFT schemes are particularly powerful and obtain quantitatively good results even at large densities.

MODEL AND FORMALISM

This chapter presents in detail the molecular model of ionic liquid crystals as employed throughout this dissertation. In the first part, the intermolecular pair potential is discussed. It is applicable to a wide range of ionic and ordinary liquid crystalline materials due to its flexibility provided by a large set of parameters. Second, the general framework of the density functional theory, which is utilized for theoretical predictions concerning the structural and orientational properties of ionic liquid crystals in the bulk and at interfaces, is unrolled.

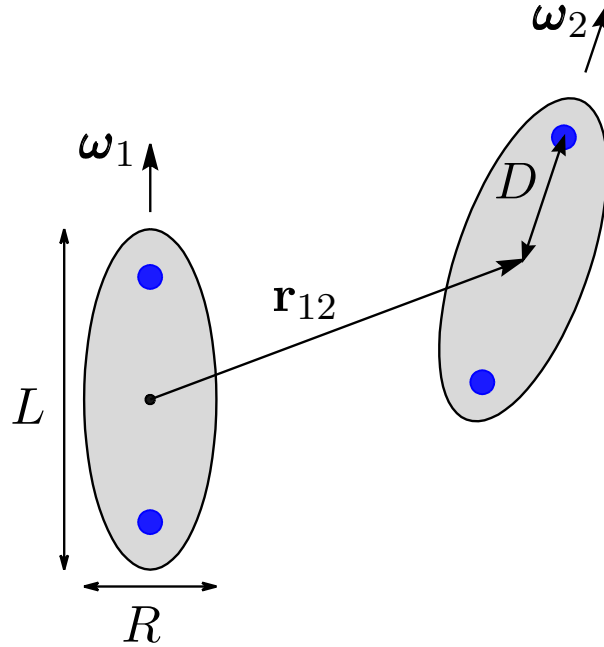


FIGURE 2.1.: Cross-sectional view of two ionic liquid crystal (ILC) coions in the plane spanned by the orientations ω_i , $i = 1, 2$, of their long axis. The particles are treated as rigid prolate ellipsoids, characterized by their length-to-breadth ratio L/R . Their orientations are fully described by the direction of their long axis ω_i ; \mathbf{r}_{12} is the center-to-center distance vector. The charges of the ILC molecules (blue dots) are located on the long axis at a distance D from their geometrical center. It is important to mention that the counterions are not modeled explicitly, but they are implicitly accounted for in terms of a background, giving rise to the screening of the charges of the coion molecules.

2.1. Molecular model and pair potential

As mentioned in the previous chapter, ionic liquid crystals (ILCs) can be synthesized in many ways [1, 36] and therefore can have various – sometimes complicated – molecular structures. However, the important chemical properties are mainly the molecular length and the location of the charged group. In order to account for these crucial properties appropriately but at the same time reducing the complexity of the utilized model, in

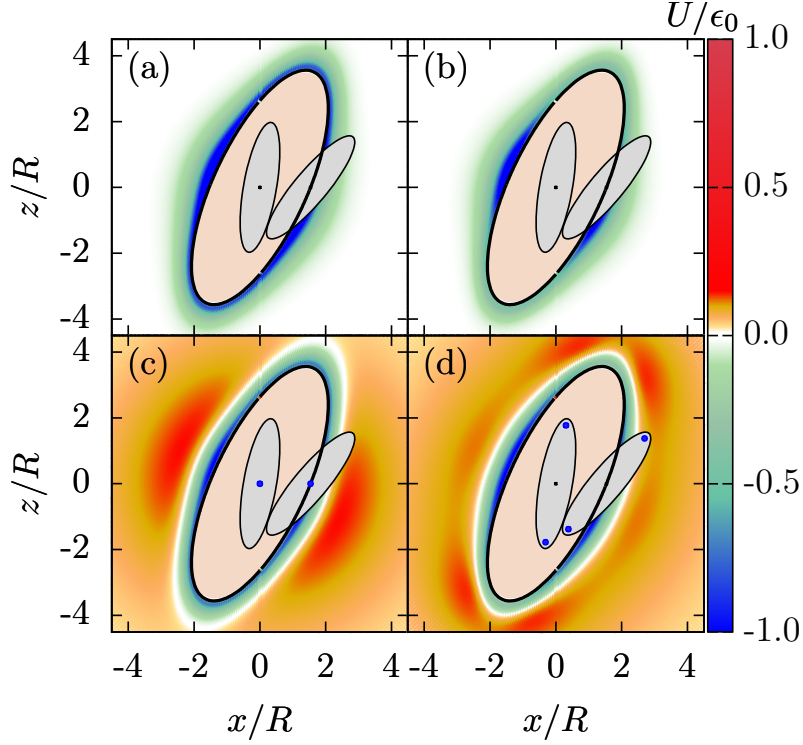


FIGURE 2.2.: Contour-plots of the pair potential U for $|\mathbf{r}_{12}| \geq R\sigma$ in the x - z -plane for four cases of particles with fixed length-to-breadth ratio $L/R = 4$ and fixed orientations. In each panel the centers of both particles lie in the plane $y = 0$. To illustrate the orientations of the ellipsoidal particles, they have been included in the plots at contact with relative direction $\hat{\mathbf{r}}_{12} = \hat{\mathbf{x}}$. The set of points at contact in the x - z -plane is illustrated by the black curve and the centers of the particles are shown by small black dots. Panel (a): uncharged liquid crystal with $\varepsilon_R/\varepsilon_L = 2$. Panel (b): uncharged liquid crystal with $\varepsilon_R/\varepsilon_L = 4$. The anisotropy of the potential is increased slightly. Panel (c): ILC with $\varepsilon_R/\varepsilon_L = 2, D/R = 0, \lambda_D/R = 5, \gamma/(R\varepsilon_0) = 0.25$. Panel (d): ILC with $\varepsilon_R/\varepsilon_L = 2, D/R = 1.8, \lambda_D/R = 5, \gamma/(R\varepsilon_0) = 0.25$. In (c) and (d) the loci of the charges are indicated as blue dots. The salmon-colored area is the excluded volume for given orientations of the two particles.

this thesis, a generic coarse-grained description, which has been introduced in Ref. [71], shall be considered. The ILC molecules are rendered as rigid prolate ellipsoids of length-to-breadth ratio L/R (see Fig. 2.1) such that the orientation of a molecule is determined by the direction $\boldsymbol{\omega}(\phi, \vartheta)$ of its long axis, where ϑ and ϕ denote the polar and azimuthal angle, respectively. As will be unveiled in the following, this model description allows

for a convenient control over the significant molecular parameters, namely the aspect ratio of the ILC molecules and their molecular charge distribution and at the same time employs a rather simple geometry. The two-body interaction potential consists of a hard core repulsive and an additional contribution $U_{\text{GB}} + U_{\text{es}}$ beyond the contact distance $R\sigma$, the sum of which can be attractive or repulsive:

$$U = \begin{cases} \infty & , |\mathbf{r}_{12}| < R\sigma(\hat{\mathbf{r}}_{12}, \boldsymbol{\omega}_1, \boldsymbol{\omega}_2) \\ U_{\text{GB}}(\mathbf{r}_{12}, \boldsymbol{\omega}_1, \boldsymbol{\omega}_2) + & , |\mathbf{r}_{12}| \geq R\sigma(\hat{\mathbf{r}}_{12}, \boldsymbol{\omega}_1, \boldsymbol{\omega}_2), \\ U_{\text{es}}(\mathbf{r}_{12}, \boldsymbol{\omega}_1, \boldsymbol{\omega}_2) & \end{cases} \quad (2.1)$$

where $\mathbf{r}_{12} := \mathbf{r}_2 - \mathbf{r}_1$ denotes the center-to-center distance vector between the two particles labeled as 1 and 2, and $\boldsymbol{\omega}_i$, $i = 1, 2$, are their orientations. The contact distance $R\sigma(\hat{\mathbf{r}}_{12}, \boldsymbol{\omega}_1, \boldsymbol{\omega}_2)$ depends on the orientations of both particles and their relative direction expressed by the unit vector $\hat{\mathbf{r}}_{12} := \mathbf{r}_{12}/|\mathbf{r}_{12}|$. In Eq. (2.1), the contribution beyond the contact distance $|\mathbf{r}_{12}| \geq R\sigma$ is subdivided into two parts: $U_{\text{GB}}(\mathbf{r}_{12}, \boldsymbol{\omega}_1, \boldsymbol{\omega}_2)$ is the so-called Gay-Berne potential [72, 73], which incorporates an attractive van der Waals-like interaction between molecules. It can be interpreted as a generalization of the Lennard-Jones pair potential to ellipsoidal particles:

$$\begin{aligned} U_{\text{GB}}(\mathbf{r}_{12}, \boldsymbol{\omega}_1, \boldsymbol{\omega}_2) &= 4\varepsilon(\hat{\mathbf{r}}_{12}, \boldsymbol{\omega}_1, \boldsymbol{\omega}_2) \\ &\times \left[\left(1 + \frac{|\mathbf{r}_{12}|}{R} - \sigma(\hat{\mathbf{r}}_{12}, \boldsymbol{\omega}_1, \boldsymbol{\omega}_2) \right)^{-12} \right. \\ &\left. - \left(1 + \frac{|\mathbf{r}_{12}|}{R} - \sigma(\hat{\mathbf{r}}_{12}, \boldsymbol{\omega}_1, \boldsymbol{\omega}_2) \right)^{-6} \right] \end{aligned} \quad (2.2)$$

with

$$\begin{aligned} \sigma(\hat{\mathbf{r}}_{12}, \boldsymbol{\omega}_1, \boldsymbol{\omega}_2) &= \left[1 - \frac{\chi}{2} \left(\frac{(\hat{\mathbf{r}}_{12} \cdot (\boldsymbol{\omega}_1 + \boldsymbol{\omega}_2))^2}{1 + \chi \boldsymbol{\omega}_1 \cdot \boldsymbol{\omega}_2} \right. \right. \\ &\left. \left. + \frac{(\hat{\mathbf{r}}_{12} \cdot (\boldsymbol{\omega}_1 - \boldsymbol{\omega}_2))^2}{1 - \chi \boldsymbol{\omega}_1 \cdot \boldsymbol{\omega}_2} \right) \right] \end{aligned} \quad (2.3)$$

and

$$\begin{aligned} \varepsilon(\hat{\mathbf{r}}_{12}, \boldsymbol{\omega}_1, \boldsymbol{\omega}_2) &= \varepsilon_0 \left(1 - (\chi \boldsymbol{\omega}_1 \cdot \boldsymbol{\omega}_2)^2\right)^{-1/2} \\ &\times \left[1 - \frac{\chi'}{2} \left(\frac{(\hat{\mathbf{r}}_{12} \cdot (\boldsymbol{\omega}_1 + \boldsymbol{\omega}_2))^2}{1 + \chi' \boldsymbol{\omega}_1 \cdot \boldsymbol{\omega}_2} \right. \right. \\ &\left. \left. + \frac{(\hat{\mathbf{r}}_{12} \cdot (\boldsymbol{\omega}_1 - \boldsymbol{\omega}_2))^2}{1 - \chi' \boldsymbol{\omega}_1 \cdot \boldsymbol{\omega}_2} \right) \right]. \end{aligned} \quad (2.4)$$

The contact distance $R\sigma(\hat{\mathbf{r}}_{12}, \boldsymbol{\omega}_1, \boldsymbol{\omega}_2)$ and the direction- and orientation-dependent interaction strength $\varepsilon(\hat{\mathbf{r}}_{12}, \boldsymbol{\omega}_1, \boldsymbol{\omega}_2)$ are both parametrically dependent on the length-to-breadth ratio L/R via the auxiliary function $\chi = ((L/R)^2 - 1)/((L/R)^2 + 1)$. Additionally, $\varepsilon(\hat{\mathbf{r}}_{12}, \boldsymbol{\omega}_1, \boldsymbol{\omega}_2)$ can be tuned via $\chi' = ((\varepsilon_R/\varepsilon_L)^{1/2} - 1)/((\varepsilon_R/\varepsilon_L)^{1/2} + 1)$, where $\varepsilon_R/\varepsilon_L$ is called the anisotropy parameter, defined in terms of the ratio of ε_R , which is the depth of the potential minimum for parallel particles positioned side by side ($\hat{\mathbf{r}}_{12} \cdot \boldsymbol{\omega}_1 = \hat{\mathbf{r}}_{12} \cdot \boldsymbol{\omega}_2 = 0$), and ε_L , which is the depth of the potential minimum for parallel particles positioned end to end ($\hat{\mathbf{r}}_{12} \cdot \boldsymbol{\omega}_1 = \hat{\mathbf{r}}_{12} \cdot \boldsymbol{\omega}_2 = 1$). The energy scale of the Gay-Berne pair interaction is set by ε_0 . Thus, the Gay-Berne pair potential has four independent free parameters: ε_0 , R , L/R , and $\varepsilon_R/\varepsilon_L$. Note that in the case of spherical particles, i.e., for $L = R$, the Gay-Berne pair potential reduces to the well-known (isotropic) Lennard-Jones potential iff, additionally, the anisotropy parameter equals unity, i.e., $\varepsilon_R/\varepsilon_L = 1$, because then $\sigma(\hat{\mathbf{r}}_{12}, \boldsymbol{\omega}_1, \boldsymbol{\omega}_2) = 1$ and $\varepsilon(\hat{\mathbf{r}}_{12}, \boldsymbol{\omega}_1, \boldsymbol{\omega}_2) = \varepsilon_0$. The second contribution $U_{\text{es}}(\mathbf{r}_{12}, \boldsymbol{\omega}_1, \boldsymbol{\omega}_2)$ in Eq. (2.1) is the electrostatic interaction of ILC molecules. Here, only the coions shall be modeled explicitly as they are embodied by the ellipsoidal particles which interact via $U(\mathbf{r}_{12}, \boldsymbol{\omega}_1, \boldsymbol{\omega}_2)$, cf., Eq. (2.1) and Fig. 2.1, whereas the counterions are not modeled explicitly. They are considered to be much smaller in size than the coions such that they can be treated as a continuous background. This background gives rise to the screening of the pure Coulomb potential between two charged sites on a length scale given by the Debye screening length λ_D such that the effective electrostatic interaction of the ILC

coions, on the level of linear response [5], is given by

$$\begin{aligned}
 U_{\text{es}}(\mathbf{r}_{12}, \boldsymbol{\omega}_1, \boldsymbol{\omega}_2) = \gamma & \left[\frac{\exp\left(-\frac{|\mathbf{r}_{12} + D(\boldsymbol{\omega}_1 + \boldsymbol{\omega}_2)|}{\lambda_D}\right)}{|\mathbf{r}_{12} + D(\boldsymbol{\omega}_1 + \boldsymbol{\omega}_2)|} \right. \\
 & + \frac{\exp\left(-\frac{|\mathbf{r}_{12} + D(\boldsymbol{\omega}_1 - \boldsymbol{\omega}_2)|}{\lambda_D}\right)}{|\mathbf{r}_{12} + D(\boldsymbol{\omega}_1 - \boldsymbol{\omega}_2)|} \\
 & + \frac{\exp\left(-\frac{|\mathbf{r}_{12} - D(\boldsymbol{\omega}_1 + \boldsymbol{\omega}_2)|}{\lambda_D}\right)}{|\mathbf{r}_{12} - D(\boldsymbol{\omega}_1 + \boldsymbol{\omega}_2)|} \\
 & \left. + \frac{\exp\left(-\frac{|\mathbf{r}_{12} - D(\boldsymbol{\omega}_1 - \boldsymbol{\omega}_2)|}{\lambda_D}\right)}{|\mathbf{r}_{12} - D(\boldsymbol{\omega}_1 - \boldsymbol{\omega}_2)|} \right]. \tag{2.5}
 \end{aligned}$$

The charges q are located symmetrically on their long axis at a distance D from the geometrical center of the particles (compare Fig. 2.1); $\gamma = q^2/(4\pi\epsilon)$ characterizes the electrostatic energy scale with permittivity ϵ . In principle, the Debye screening length

$$\lambda_D = \sqrt{\frac{kT}{q^2 \varrho_c}} \tag{2.6}$$

is a function of temperature T and of the number density ϱ_c of the counter ions. Thus, it depends on the thermodynamic state of the fluid. However, in the present model λ_D is taken to be a constant parameter. In order to compare results, obtained within this model, with data from actual physical systems, one could measure the value of the Debye screening length experimentally and tune the model parameter λ_D accordingly.

In Fig. 2.2 the full pair potential $U(\mathbf{r}_{12}, \boldsymbol{\omega}_1, \boldsymbol{\omega}_2)$ (Eq. (2.1)) is illustrated beyond the contact distance for specific choices of the model parameters. The panels (a) and (b) show the pure Gay-Berne potential, which is predominantly attractive in the space outside the overlap volume (cream-colored area). The overlap volume changes by varying the particle orientations as well as by changing the length-to-breadth ratio L/R . Note that these dependences are not apparent from Fig. 2.2, since $L/R = 4$ and the particle orientations $\boldsymbol{\omega}_i$ stay unchanged for all panels. In panel (b) the anisotropy parameter $\epsilon_R/\epsilon_L = 4$ is chosen to be two times larger than for panel (a) ($\epsilon_R/\epsilon_L = 2$). Thus, the ratio of the well depth at the tails and at the sides is increased. The two bottom panels, (c) and (d), show the same choices for the Gay-Berne parameters as for panel (a), but the electrostatic repulsion of the charged groups on the molecules, illustrated

by blue dots, is included ($\gamma/(R\varepsilon_0) = 0.25$). In panel (c) the loci of the two charges of the particles coincide at its center (i.e., $D = 0$) while in panel (d) they are located near the tips ($D/R = 1.8$). For both cases with charge, the effective interaction range is significantly increased compared with the uncharged case and is governed by the Debye screening length, chosen as $\lambda_D/R = 5$.

2.2. Present DFT framework

The degrees of freedom of the particles (compare Sec. 2.1) are fully described by the positions \mathbf{r} of their centers and the orientations $\boldsymbol{\omega}$ of their long axes. Thus, within density functional theory [65] an appropriate variational grand potential functional $\beta\Omega[\varrho]$ of position- and orientation-dependent number density profiles $\varrho(\mathbf{r}, \boldsymbol{\omega})$ has to be found; its minimum corresponds to the equilibrium density profile. The grand potential functional for uniaxial particles, in the absence of external fields, can generically be expressed as

$$\beta\Omega[\varrho] = \int_{\mathcal{V}} d^3r \int_{\mathcal{S}} d^2\omega \varrho(\mathbf{r}, \boldsymbol{\omega}) [\ln(4\pi\Lambda^3\varrho(\mathbf{r}, \boldsymbol{\omega})) - (1 + \beta\mu)] + \beta\mathcal{F}[\varrho], \quad (2.7)$$

where the integration domains \mathcal{V} and \mathcal{S} denote the system volume and the full solid angle, respectively (see Eq. (1.1)). The first term in Eq. (2.7) is the purely entropic free energy contribution of non-interacting uniaxial particles, where $\beta = 1/(k_B T)$ denotes the inverse thermal energy, μ the chemical potential, and Λ the thermal de Broglie wavelength. The last term is the excess free energy $\beta\mathcal{F}[\varrho]$ in units of $k_B T$, which incorporates the effects of the particle interactions. Minimization of Eq. (2.7) leads to the Euler-Lagrange equation, which determines the equilibrium density profile $\varrho(\mathbf{r}, \boldsymbol{\omega})$ (compare Eq. (1.2)):

$$\varrho(\mathbf{r}, \boldsymbol{\omega}) = \frac{e^{\beta\mu}}{4\pi\Lambda^3} \exp[c^{(1)}(\mathbf{r}, \boldsymbol{\omega}, [\varrho])], \quad (2.8)$$

where

$$c^{(1)}(\mathbf{r}, \boldsymbol{\omega}, [\varrho]) = -\frac{\delta\beta\mathcal{F}[\varrho]}{\delta\varrho} \quad (2.9)$$

is the one-particle direct correlation function. It is completely determined by the excess free energy functional $\beta\mathcal{F}[\varrho]$.

Since $\beta\mathcal{F}[\varrho]$ is the characterizing quantity of the underlying many-body problem, in general it is not known exactly so that appropriate approximations have to be found.

The starting point of this dissertation is a *weighted density* formulation of $\beta\mathcal{F}[\varrho]$ in the spirit of Ref. [68]:

$$\beta\mathcal{F}[\varrho] = \frac{1}{2} \int_{\mathcal{V}} d^3r \int_{\mathcal{S}} d^2\omega \varrho(\mathbf{r}, \boldsymbol{\omega}) \beta\psi(\mathbf{r}, \boldsymbol{\omega}, [\bar{\varrho}]). \quad (2.10)$$

This choice leads immediately to the following expression for the one-particle direct correlation function:

$$\begin{aligned} c^{(1)}(\mathbf{r}, \boldsymbol{\omega}, [\varrho]) &= -\frac{1}{2} \left[\beta\psi(\mathbf{r}, \boldsymbol{\omega}, [\bar{\varrho}]) + \int_{\mathcal{V}} d^3r' \int_{\mathcal{S}} d^2\omega' \varrho(\mathbf{r}', \boldsymbol{\omega}') \right. \\ &\quad \left. \times \int_{\mathcal{V}} d^3r'' \int_{\mathcal{S}} d^2\omega'' \frac{\delta\beta\psi(\mathbf{r}', \boldsymbol{\omega}', [\bar{\varrho}])}{\delta\bar{\varrho}(\mathbf{r}'', \boldsymbol{\omega}'')} \frac{\delta\bar{\varrho}(\mathbf{r}'', \boldsymbol{\omega}'', [\varrho])}{\delta\varrho(\mathbf{r}, \boldsymbol{\omega})} \right]. \end{aligned} \quad (2.11)$$

In order to evaluate Eq. (2.11), one needs to know the effective one-particle potential $\beta\psi[\bar{\varrho}]$ as a functional of the weighted density $\bar{\varrho}(\mathbf{r}, \boldsymbol{\omega}, [\varrho])$, which in the present case is chosen as a projection of the full density profile $\varrho(\mathbf{r}, \boldsymbol{\omega})$ onto a certain functional subspace, the choice of which will be motivated in the subsequent paragraph:

The present framework shall be designed for the study of ILC-systems which are composed of ellipsoidal particles, cf., Fig. 2.1. Hence, one expects the occurrence of isotropic (no positional and no orientational order), nematic (no positional, but orientational order), and smectic (one-dimensional positional order along the smectic layer normal $\hat{\mathbf{n}}$ and orientational order) bulk phases. At sufficiently low temperatures and sufficiently large densities the homogenous phases mentioned above, i.e., the isotropic and nematic phases, or partially homogenous phases, i.e., the smectic phases, undergo transitions to crystalline phases. The first three types of phases can be represented by spatially periodic density profiles $\varrho(\mathbf{r}, \boldsymbol{\omega})$ with wavelength d in $\hat{\mathbf{n}}$ -direction and spatially constant density perpendicular to it. For a uniform density in $\hat{\mathbf{n}}$ -direction d is not uniquely defined and can be chosen arbitrarily, whereas for smectic structures d is an integer multiple of the layer spacing. (Although there is no need to introduce d for uniform phases, within the present approach based on the projected density $\bar{\varrho}(\mathbf{r}, \boldsymbol{\omega})$ (see Eqs. (2.12)-(2.14) below), also a uniform density profile $\varrho(\mathbf{r}, \boldsymbol{\omega})$ demands a value for d entering into Eq. (2.14). However, the corresponding results do not depend on such a choice of d ; any value $d > 0$ is valid.) This observation motivates the approach to consider a projected density $\bar{\varrho}(\mathbf{r}, \boldsymbol{\omega}, [\varrho])$, which is obtained by weighting the original density profile $\varrho(\mathbf{r}, \boldsymbol{\omega})$ within a periodic cell of volume $\mathcal{V}_d = A \times d$ around the position \mathbf{r} , where A is the cross-sectional area of the system. In order to express the orientational dependence of the projected

density $\bar{\varrho}(\mathbf{r}, \boldsymbol{\omega})$ explicitly, in addition to the Fourier series expansion of $\varrho(\mathbf{r}, \boldsymbol{\omega})$ in terms of $\cos(2\pi i(\mathbf{r} \cdot \hat{\mathbf{n}})/d)$ (with $i = 0, 1, 2$) $\bar{\varrho}(\mathbf{r}, \boldsymbol{\omega})$ (Eq. (2.12)) is determined by performing furthermore an expansion of $\varrho(\mathbf{r}, \boldsymbol{\omega})$ in terms of Legendre polynomials $P_l(y = \cos \vartheta)$ up to and including second order, i.e., $l = 0, 2$. The contribution corresponding to $l = 1$ vanishes due to the symmetry of the underlying pair potential $U(\mathbf{r}_{12}, \boldsymbol{\omega}_1, \boldsymbol{\omega}_2)$, cf., Eq. (2.1):

$$\begin{aligned} \bar{\varrho}(\mathbf{r}, \boldsymbol{\omega}, [\varrho]) &= \frac{1}{4\pi} \left[Q_0(\mathbf{r}, [\varrho]) + Q_1(\mathbf{r}, [\varrho]) \cos(2\pi(\mathbf{r} \cdot \hat{\mathbf{n}})/d) \right. \\ &+ Q_2(\mathbf{r}, [\varrho]) \cos(4\pi(\mathbf{r} \cdot \hat{\mathbf{n}})/d) + 5P_2(\boldsymbol{\omega} \cdot \hat{\mathbf{n}}) \left(Q_3(\mathbf{r}, [\varrho]) \right. \\ &\left. \left. + Q_4(\mathbf{r}, [\varrho]) \cos(2\pi(\mathbf{r} \cdot \hat{\mathbf{n}})/d) + Q_5(\mathbf{r}, [\varrho]) \cos(4\pi(\mathbf{r} \cdot \hat{\mathbf{n}})/d) \right) \right], \end{aligned} \quad (2.12)$$

where $P_0(y) = 1$, $P_2(y) = (3y^2 - 1)/2$, and with coefficients $Q_i(\mathbf{r}, [\varrho])$ defined as

$$Q_i(\mathbf{r}, [\varrho]) = \frac{1}{\mathcal{V}_d} \int_{\mathcal{V}} d^3 r' \int_{\mathcal{S}} d^2 \omega' \varrho(\mathbf{r}', \boldsymbol{\omega}') w_i(\mathbf{r}, \mathbf{r}', \boldsymbol{\omega}') \quad (2.13)$$

with

$$\begin{aligned} w_0 &= \Theta(d/2 - |(\mathbf{r} - \mathbf{r}') \cdot \hat{\mathbf{n}}|), \\ w_1 &= 2\Theta(d/2 - |(\mathbf{r} - \mathbf{r}') \cdot \hat{\mathbf{n}}|) \cos(2\pi(\mathbf{r}' \cdot \hat{\mathbf{n}})/d), \\ w_2 &= 2\Theta(d/2 - |(\mathbf{r} - \mathbf{r}') \cdot \hat{\mathbf{n}}|) \cos(4\pi(\mathbf{r}' \cdot \hat{\mathbf{n}})/d), \\ w_3 &= \Theta(d/2 - |(\mathbf{r} - \mathbf{r}') \cdot \hat{\mathbf{n}}|) P_2(\boldsymbol{\omega}' \cdot \hat{\mathbf{n}}), \\ w_4 &= 2\Theta(d/2 - |(\mathbf{r} - \mathbf{r}') \cdot \hat{\mathbf{n}}|) P_2(\boldsymbol{\omega}' \cdot \hat{\mathbf{n}}) \cos(2\pi(\mathbf{r}' \cdot \hat{\mathbf{n}})/d), \\ w_5 &= 2\Theta(d/2 - |(\mathbf{r} - \mathbf{r}') \cdot \hat{\mathbf{n}}|) P_2(\boldsymbol{\omega}' \cdot \hat{\mathbf{n}}) \cos(4\pi(\mathbf{r}' \cdot \hat{\mathbf{n}})/d). \end{aligned} \quad (2.14)$$

Here $\Theta(x)$ denotes the Heaviside step function. Without loss of generality, for the three relevant bulk phases, one can consider the entire system to be composed of a set of periodic macro-cells with periodicity d in the direction $\hat{\mathbf{n}}$, due to the homogeneity in lateral directions, i.e., $\mathbf{r} \cdot \hat{\mathbf{n}} = 0$. This is accounted for by choosing $\Theta(d/2 - |(\mathbf{r} - \mathbf{r}') \cdot \hat{\mathbf{n}}|)$ as a cut-off function in Eq. (2.14). However at interfaces the homogeneity in lateral directions is not necessarily given. In particular for isotropic-smectic interfaces with non-vanishing tilt angle α between the smectic layer normal and the interface normal, i.e., $\alpha > 0$ (see Secs. 4.2 and 4.3). In these cases a generalized cut-off function $\mathcal{T}(x)$

(Eq. (4.4)) is used which accounts for the preserved periodic structure in the direction perpendicular to the interface normal. (A detailed description and discussion will be provided in Sec. 4.2.1.)

In general the coefficients $Q_i(\mathbf{r}, [\varrho])$ depend on the position \mathbf{r} , for example in the vicinity of an interface, cf., Chapter 4, whereas for the relevant bulk phases, which are described by spatially periodic bulk profiles, they are constant, $Q_i(\mathbf{r}, [\varrho]) = Q_i = \text{const}$. Thus, the Q_i in Eqs. (2.13) and (2.14) represent the first coefficients of a Fourier expansion of the spatially periodic function $\varrho(\mathbf{r}, \boldsymbol{\omega})$. Note, that the factor 2 for w_1 , w_2 , w_4 , and w_5 in Eq. (2.14) is due to the definition of the first and second Fourier modes. Analogously, the factor 5 in the last term of Eq. (2.12) is due to the definition of the second order coefficient of the Legendre-series. Within the present framework the director field, describing the mean orientation of the particles, shall be homogeneous in space and only symmetric distributions of orientations $\boldsymbol{\omega}$ around the director are taken into account, so that the generated profiles depend only on the projection $\boldsymbol{\omega} \cdot \hat{\mathbf{n}}$ of $\boldsymbol{\omega}$ on the direction $\hat{\mathbf{n}}$ of the director (see Eqs. (2.12) and (2.14)). Furthermore, solely smectic phases of the A-type (smectic-A) are considered because, here, the director shall be parallel to the smectic layer normal [4]. This implies that the present description is designed for studying uniaxial phases, like the isotropic, nematic, or the smectic-A phase (see Chapter 3), and additionally it allows to study free interfaces between these bulk phases (Chapter 4). It is worthwhile mentioning, that in order to study biaxial phases (e.g., the smectic-C phase the director of which is tilted with respect to the layer normal) one would need to keep the full orientational dependence of the projected density $\bar{\varrho}(\mathbf{r}, \boldsymbol{\omega})$ on the solid angle, unlike here, where the orientational dependence is reduced to the projection on one distinguished axis, that is the director, respectively the smectic layer normal $\hat{\mathbf{n}}$. Nonetheless, the computer simulations, which will be presented and discussed in Chapter 3 did not reveal any evidence of the occurrence of biaxial phases in the investigated systems. In particular, the smectic-A-type phases were the only smectic phases that could be observed. Therefore, the restriction to uniaxial structures seems to be adequate for the systems studied here.

In the final step of constructing the density functional, the effective one-particle potential $\beta\psi[\bar{\varrho}]$ needs to be specified. Here, it is composed of two parts. The first one is due to the hard-core interaction. The in the context of hard uniaxial particles well-studied

Parsons-Lee functional [74, 75]

$$\begin{aligned} \beta\psi_{\text{PL}}(\mathbf{r}, \boldsymbol{\omega}, [\bar{\rho}]) &= - \int_{\mathcal{V}} d^3r' \int_S d^2\omega' \bar{\rho}(\mathbf{r}', \boldsymbol{\omega}') \\ &\times \frac{\mathcal{J}(Q_0(\mathbf{r})) + \mathcal{J}(Q_0(\mathbf{r}'))}{2} f_M(\mathbf{r} - \mathbf{r}', \boldsymbol{\omega}, \boldsymbol{\omega}'), \end{aligned} \quad (2.15)$$

shall be considered here, where $f_M(\mathbf{r} - \mathbf{r}', \boldsymbol{\omega}, \boldsymbol{\omega}')$ is the Mayer f-function [5] of the hard core pair potential and $\mathcal{J}(Q_0)$ modifies the corresponding original Onsager free energy functional [47, 62] (i.e., the second-order virial approximation) such that the Carnahan-Starling equation of state [75] is reproduced for spheres, i.e., $L = R$:

$$\mathcal{J}(Q_0) = \frac{1 - \frac{3}{4}\eta_0(Q_0)}{(1 - \eta_0(Q_0))^2}, \quad (2.16)$$

where $\eta_0 = Q_0 LR^2\pi/6$ denotes the mean packing fraction within the volume \mathcal{V}_d . It is proportional to the coefficient Q_0 which gives the mean density within the volume \mathcal{V}_d . The original Onsager functional is recovered by replacing $\mathcal{J}(Q_0)$ by Q_0 in Eq. (2.15).

The second contribution to the effective one-particle potential $\beta\psi[\bar{\rho}]$ takes into account the interactions beyond the contact distance (see the case $|\mathbf{r}_{12}| \geq R\sigma$ in Eq. (2.1)) within the modified mean-field approximation [76], a variant of the extended random phase approximation (ERPA) [65]:

$$\begin{aligned} \beta\psi_{\text{ERPA}}(\mathbf{r}, \boldsymbol{\omega}, [\bar{\rho}]) &= \int_{\mathcal{V}} d^3r' \int_S d^2\omega' \bar{\rho}(\mathbf{r}', \boldsymbol{\omega}') \\ &\times \beta U(\mathbf{r} - \mathbf{r}', \boldsymbol{\omega}, \boldsymbol{\omega}') (1 + f_M(\mathbf{r} - \mathbf{r}', \boldsymbol{\omega}, \boldsymbol{\omega}')). \end{aligned} \quad (2.17)$$

For the sake of simplicity, instead of using the full angular expressions for the two contributions to the effective one-particle potential, given by Eqs. (2.15) and (2.17), their expansions in terms of Legendre polynomials up to second order are utilized. In doing so an explicit expression for the orientational dependence of the effective one-particle potential is provided:

$$\begin{aligned} \beta\psi(\mathbf{r}, \boldsymbol{\omega}, [\bar{\rho}]) &= \zeta_0(\mathbf{r}) + \zeta_2(\mathbf{r}) P_2(\boldsymbol{\omega} \cdot \hat{\mathbf{n}}), \\ \zeta_l(\mathbf{r}) &= \frac{1}{4\pi} \int_S d^2\omega' (\beta\psi_{\text{PL}}(\mathbf{r}, \boldsymbol{\omega}') + \beta\psi_{\text{ERPA}}(\mathbf{r}, \boldsymbol{\omega}')) \begin{cases} 1 & , l = 0 \\ 5P_2(\boldsymbol{\omega}' \cdot \hat{\mathbf{n}}) & , l = 2. \end{cases} \end{aligned} \quad (2.18)$$

In the interest of determining the equilibrium density profile in Eq. (2.8), one has to calculate the one-particle direct correlation function (Eq. (2.11)), using the definition of the weighted density $\bar{\varrho}(\mathbf{r}, \boldsymbol{\omega})$ (Eqs. (2.12)-(2.14)), and the effective one-particle potential $\beta\psi(\mathbf{r}, \boldsymbol{\omega}, [\bar{\varrho}])$ (Eqs. (2.15)-(2.18)).

Once the equilibrium density profile $\varrho(\mathbf{r}, \boldsymbol{\omega})$ is known, the structural and orientational properties of the fluid under consideration can be conveniently discussed in terms of the (total) number density profile

$$n(\mathbf{r}) := \int_{\mathcal{S}} d^2\omega \varrho(\mathbf{r}, \boldsymbol{\omega}) \quad (2.19)$$

and the orientational order parameter

$$S_2(\mathbf{r}) := \int_{\mathcal{S}} d^2\omega f(\mathbf{r}, \boldsymbol{\omega}) P_2(\boldsymbol{\omega} \cdot \hat{\mathbf{n}}), \quad (2.20)$$

respectively. $f(\mathbf{r}, \boldsymbol{\omega}) := \varrho(\mathbf{r}, \boldsymbol{\omega})/n(\mathbf{r})$ denotes the orientational distribution function.

Further details regarding the calculation of the equilibrium density profiles $\varrho(\mathbf{r}, \boldsymbol{\omega})$ are provided in Secs. 3.2.1 and 4.2.1. For instance the evaluation of the one-particle direct correlation function $c^{(1)}(\mathbf{r}, \boldsymbol{\omega}, [\varrho])$ (see Eqs. (2.11), (3.3) and (4.5)) is described accounting for the distinct types of systems that are considered in Chapters 3 (bulk) and 4 (free interfaces).

BULK PHASE BEHAVIOR OF ILCs

The bulk phase behavior of various kinds of ILCs, characterized by the set of parameters entering the interaction potential, is studied within density functional theory and grand canonical Monte Carlo simulations. Specifically the effect of the intrinsic molecular properties, i.e., the aspect ratio and the loci of the molecules charges, on the phase behavior is investigated.

3.1. Introduction

Ionic liquid crystals (ILCs) are pure ionic systems, composed solely of cations (+) and anions (−). At least one of the ion species exhibits an anisotropic (either elongated or prolate) molecular shape [1]. This anisotropy gives rise to the occurrence of liquid-crystalline phases, so-called *mesophases* [4]. Various types of ILCs can be synthesized [1, 36]; different combinations of, e.g., (charged) imidazolium rings and alkyl chains allow one to tune the length of the ionic mesogenes as well as the location of their charges. Thereby one is able to promote distinctive properties of ILCs, for instance, a high thermal and high electrochemical stability, which might be beneficial for technological applications [1, 36, 77–79]. A specific example of an ILC system, which has been studied in the past, e.g., in Refs. [2, 80], is composed of large and elongated cations (1-dodecyl-3-methylimidazolium) and significantly smaller anions (iodide). As a result, for such an ILC system, one observes a liquid crystalline structure, in particular the smectic-A phase S_A . (The S_A phase is characterized by layers of particles which are well aligned with the layer normal and the layer spacing is of the size of the particle length.) In this case, the S_A phase is formed by the cations, whereas the anions do not contribute to that structure, but they can serve as ionic charge carriers [2]. The nanostructure of the cations leads to pathways for the anions in between the layers and increases the ionic conductivity in the direction parallel to the layers. Therefore this particular ILC system is a promising candidate for technological applications, e.g., as *electrolyte in dye-sensitized solar cells* (DSSCs) [2, 39].

While the complexity of the underlying interactions gives rise to the interesting properties of ILCs, it is at the same time very challenging to study these systems within theory or simulations. In that regard, the ILC system mentioned above is interesting from a theoretical perspective, too, because the significant difference in size of the cations and the anions rationalizes the approximation to consider the anions as point charges, which give rise to an (effective) screened electrostatic interaction of the mesogenic cations [71]. Thus, effective one-species models can be employed, still capturing the important structural and orientational properties of the mesogenic cations. Such a model has been introduced and discussed in Chapter 2 and it will be used throughout this dissertation.

As a first step, based on this model, the phase behavior of ILCs is studied. Thereby, insights on how molecular properties, e.g., the aspect-ratio or the charge distribution of the molecules, affect the bulk properties of these types of ILCs can be gained. A com-

prehensive understanding of the relation between the underlying molecular properties and the phase behavior is *inter alia* necessary for a systematic synthesis of ILCs, which should meet specific material properties. Furthermore, theoretical guidance is beneficial for finding and exploring novel properties which might occur in ILC systems.

It has been pointed out in Chapter 1, that it is the very interplay of shape-anisotropy and electrostatic interactions, which gives rise to the vast phenomenology observed for ILC materials and at the same time poses a particular challenge for theoretical studies. Constructing theoretical frameworks, that are applicable to this kind of materials and which provide a deeper understanding of the origin of the properties of ILCs, is thus an ongoing process. Recently, it was concluded [36] that the effect of the size, the shape, and the charge distribution of molecules on the properties of ILC materials is yet not sufficiently understood. Further investigations from both the experimental and the theoretical perspective are essential. In that regard, this chapter's analysis aims on showing that the considered molecular model, describing ILC fluids by incorporating orientational degrees of freedom as well as an anisotropic charge distribution, gives rise to a phenomenology concerning the phase behavior and bulk structures, which is much richer than the one of simpler models of spherical ions or of ordinary liquid crystals. The most striking result is the occurrence of a novel smectic phase S_{AW} at low temperatures, the layer spacing of which is larger than that of the ordinary high-temperature smectic phase S_A . Moreover, the crucial role of the loci of the charges on the ILC molecules is unrolled. This emphasizes the necessity of considering such kind of sophisticated model in order to study reliably complex ionic liquids that combine ionic compounds with anisotropic molecular shapes such as ILCs.

This chapter is structured as follows: First, the relevant observables in the context of the bulk phase behavior of anisotropic fluids are introduced and derived from the general DFT formalism which has been presented in Sec. 2.2. In order to assess the stability of the observed mesophases with respect to crystalline phases (which are not captured by the framework provided in Sec. 2.2), in Sec. 3.2.3, an appropriate stability analysis is presented. Furthermore, the methodology of a grand canonical Monte Carlo study of the employed ILC model is unrolled in the successive Sec. 3.2.4. Monte Carlo simulations are used to validate the present theoretical predictions by DFT. The results obtained within these methods, i.e., DFT and grand canonical Monte Carlo simulations, are discussed in Sec. 3.3. Finally, in Sec. 3.4 conclusions regarding the phase behavior and the various observed bulk structures are drawn.

3.2. Methods

3.2.1. Bulk phases within the present DFT framework

In Sec. 2.2 the general DFT-framework which is the theoretical foundation of this dissertation has been unrolled. The equilibrium density profile $\rho(\mathbf{r}, \boldsymbol{\omega})$ is implicitly determined by the Euler-Lagrange equation, i.e., Eq. (2.8), which can be evaluated using Eq. (2.11) with the projected density $\bar{\rho}(\mathbf{r}, \boldsymbol{\omega}, [\varrho])$, i.e., Eq. (2.12) and the effective one-particle potential $\beta\psi[\bar{\rho}]$, i.e., Eq. (2.18). For the particular case of bulk phases, in which the coefficients Q_i in Eq. (2.12) do not depend on the position \mathbf{r} , one finds the following expression for the equilibrium density profile (see Appendix A)

$$\rho^{(0)}(\mathbf{r}, \boldsymbol{\omega}) := \exp \left[\sum_{i=0}^2 A_i \cos(2\pi i(\mathbf{r} \cdot \hat{\mathbf{n}})/d) + P_2(\boldsymbol{\omega} \cdot \hat{\mathbf{n}}) B_i \cos(2\pi i(\mathbf{r} \cdot \hat{\mathbf{n}})/d) \right], \quad (3.1)$$

where the constant coefficients A_i and B_i are to be determined by evaluating Eqs. (2.8) and (2.11) for this expression of $\rho^{(0)}(\mathbf{r}, \boldsymbol{\omega})$. As expected, the bulk density profile depends only on the projections $\mathbf{r} \cdot \hat{\mathbf{n}}$ and $\boldsymbol{\omega} \cdot \hat{\mathbf{n}}$.

It turns out, that the precise evaluation of the coefficients A_i and B_i is very costly in terms of computational resources and it is almost not feasible with reasonable computational effort. In order to circumvent those numerical difficulties, two alternative routes are pursued.

Along the first one, instead of solving the full Euler-Lagrange equation, by using the *exact* one-particle direct correlation function (Eq. (2.11)), a *modified* one-particle direct correlation function $\tilde{c}^{(1)}(\mathbf{r}, \boldsymbol{\omega}, [\varrho])$ is utilized. \tilde{c} is obtained by replacing in the integrand of Eq. (2.11) the true density profile $\rho(\mathbf{r}, \boldsymbol{\omega})$ by the weighted density $\bar{\rho}(\mathbf{r}, \boldsymbol{\omega})$. Consequently, Eq. (2.11) now reads

$$\tilde{c}^{(1)}(\mathbf{r}, \boldsymbol{\omega}, [\varrho]) = -\frac{1}{2} \left[\beta\psi(\mathbf{r}, \boldsymbol{\omega}, [\bar{\rho}]) + \int_{\mathcal{V}} d^3 r' \int_{\mathcal{S}} d^2 \omega' \bar{\rho}(\mathbf{r}', \boldsymbol{\omega}') \frac{\delta \beta\psi(\mathbf{r}', \boldsymbol{\omega}', [\bar{\rho}])}{\delta \bar{\rho}(\mathbf{r}, \boldsymbol{\omega})} \right] \quad (3.2)$$

where $\frac{\delta \bar{\rho}(\mathbf{r}'', \boldsymbol{\omega}'')}{\delta \bar{\rho}(\mathbf{r}, \boldsymbol{\omega})} = \delta(\mathbf{r}'' - \mathbf{r})\delta(\boldsymbol{\omega}'' - \boldsymbol{\omega})$ has been used. In Eq. (3.2), evaluating the functional

derivative of the effective one-particle potential $\beta\psi[\bar{\varrho}]$ w.r.t. the weighted density $\bar{\varrho}$ and using Eq. (2.18) yields the following final expression for the modified one-particle direct correlation function $\tilde{c}^{(1)}$:

$$\begin{aligned} \tilde{c}^{(1)}(\mathbf{r}, \boldsymbol{\omega}, [\varrho]) &= -\beta\psi(\mathbf{r}, \boldsymbol{\omega}, [\bar{\varrho}]) + \frac{\partial Q_0 \mathcal{J}(Q_0)}{2\mathcal{V}_d} \times \\ &\int_{\mathcal{V}} d^3r' \int_{\mathcal{S}} d^2\omega' \bar{\varrho}(\mathbf{r}', \boldsymbol{\omega}') \Theta(d/2 - |z - z'|) \times \\ &\int_{\mathcal{V}} d^3r'' \int_{\mathcal{S}} d^2\omega'' \bar{\varrho}(\mathbf{r}'', \boldsymbol{\omega}'') f_M(\mathbf{r}' - \mathbf{r}'', \boldsymbol{\omega}', \boldsymbol{\omega}''), \end{aligned} \quad (3.3)$$

where $\frac{\delta Q_0(\mathbf{r}', [\bar{\varrho}])}{\delta \bar{\varrho}(\mathbf{r}, \boldsymbol{\omega})} = \Theta(d/2 - |z - z'|)/\mathcal{V}_d$ has been used, which holds for bulk phases. Note that the smectic layer normal $\hat{\mathbf{n}}$ has been chosen to be parallel to z -axis, i.e., $\hat{\mathbf{n}} = \hat{\mathbf{z}}$ and $\mathbf{r} \cdot \hat{\mathbf{n}} = z$. Due to the product rule of functional differentiation, the evaluation of the last term in Eq. (3.2) produces a second term $-\frac{1}{2}\beta\psi(\mathbf{r}, \boldsymbol{\omega}, [\bar{\varrho}])$ and the latter term in Eq. (3.3). As expected, the solution of the modified Euler-Lagrange equation indeed differs from the exact one. However, the solution obtained from the modified one-particle direct correlation function $\tilde{c}^{(1)}(\mathbf{r}, \boldsymbol{\omega}, [\varrho])$ exhibits the same functional form as the exact solution in Eq. (3.1), but with modified coefficients A_i and B_i (see the last paragraph in Appendix A).

Yet, as mentioned above, one could have followed another, second, route, which utilizes the knowledge of the functional form of the (exact) equilibrium density profile in Eq. (3.1). By plugging this generic form into the grand potential functional and by minimizing it w.r.t. the coefficients A_i and B_i , $i = 0, 1, 2$,

$$\left. \frac{\partial \beta\Omega[\varrho^{(0)}]}{\partial X_i} \right|_{X_j} = 0, \quad X_i = A_i, B_i, \quad i \neq j, \quad (3.4)$$

one obtains six equations, which determine the equilibrium values for the coefficients A_i and B_i and therefore yield the exact equilibrium density profile for the considered excess free energy functional. However, this generic form holds only for the bulk profiles, because the periodic structure is essential for the validity of this expression. Therefore, this scheme cannot be extended to study interfacial problems, e.g., free interfaces, by using coexisting bulk phases as boundary conditions. This is unlike the first approach, which is applicable even at interfaces.

By comparing the two different approaches, one can analyze, how the modification leading to Eq. (3.3) quantitatively affects the exact bulk solution. It turns out, that for all

examined cases the two approaches lead to qualitatively equivalent results and, moreover, that the quantitative differences of both approaches are only minor (see Appendix B). It is worth mentioning, that for the particular case of isotropic fluids both solutions are identical, because for isotropic phases $\bar{\varrho}(\mathbf{r}, \boldsymbol{\omega}) = \varrho(\mathbf{r}, \boldsymbol{\omega})$.

3.2.2. Phase behavior

In order to study the phase behavior of ILCs within the present DFT approach, the first minimization scheme, discussed in Sec. 3.2.1, is applied. It is based on a modified expression (Eq. (3.3)) for the one-particle direct correlation function $\tilde{c}^{(1)}(\mathbf{r}, \boldsymbol{\omega}, [\varrho])$, in order to evaluate the Euler-Lagrange equation in Eq. (2.8). For given values of the chemical potential μ and temperature T the (bulk) solutions are described by a set of coefficients Q_i (Eqs. (2.13) and (2.14)) which is obtained by numerically solving Eqs. (2.8) and (3.3), thereby using the definition of the projected density $\bar{\varrho}(\mathbf{r}, \boldsymbol{\omega})$ in Eq. (2.12). The numerical evaluation is carried out by employing a Picard iteration with retardation (see [70]). Subsequently, the (approximate) equilibrium density profile $\varrho^{\text{eq}}(\mathbf{r}, \boldsymbol{\omega})$ is obtained by evaluating Eq. (2.8), using the set of coefficients Q_i of the solution. Note that $\varrho^{\text{eq}}(\mathbf{r}, \boldsymbol{\omega})$ exhibits the same functional form as the exact bulk solution in Eq. (3.1) and that the exact and the approximate solution of the Euler-Lagrange-equation yield only minor quantitative differences (see Appendix B and Table B.1).

In order to distinguish different types of bulk phases, the following four order parameters are defined:

$$\begin{aligned} n_0 &= \frac{1}{\mathcal{V}_d} \int_{\mathcal{V}_d} d^3r' n(\mathbf{r}'), \\ W_0 &= \frac{2}{\mathcal{V}_d} \int_{\mathcal{V}_d} d^3r' n(\mathbf{r}') \cos(2\pi z'/d), \\ S_{20} &= \frac{1}{\mathcal{V}_d} \int_{\mathcal{V}_d} d^3r' S_2(\mathbf{r}'), \\ W_2 &= \frac{2}{\mathcal{V}_d} \int_{\mathcal{V}_d} d^3r' S_2(\mathbf{r}') \cos(2\pi z'/d). \end{aligned} \quad (3.5)$$

The mean density n_0 in a volume of size \mathcal{V}_d and W_0 are the first two coefficients of a Fourier series expansion of the number density $n(\mathbf{r})$ (Eq. (2.19)), while the mean orientational order parameter S_{20} and W_2 are the first two coefficients of a Fourier series expansion of the (spatially varying) orientational order parameter $S_2(\mathbf{r})$ (Eq. (2.20)). For $S_2(\mathbf{r}) = 1$ the particles at position \mathbf{r} are perfectly aligned with the director, while for

$S_2(\mathbf{r}) = -0.5$ they are perfectly perpendicular to the director. In the case of $|S_2(\mathbf{r})| \ll 1$ particles at \mathbf{r} do not show orientational order. In the case of the three relevant bulk phases, $n(\mathbf{r})$ and $S_2(\mathbf{r})$ are periodic functions in z -direction and can be expanded in terms of the Fourier series

$$n(z) = a_0 + \sum_{k=1}^{\infty} a_{2k} \cos(2\pi kz/d) \quad (3.6)$$

and

$$S_2(z) = b_0 + \sum_{k=1}^{\infty} b_{2k} \cos(2\pi kz/d) \quad (3.7)$$

where the first two non-zero expansion coefficients, a_0 and a_2 and b_0 and b_2 , follow from n_0 and W_0 , and from S_{20} and W_2 , respectively (see Eq. (3.5)). Antisymmetric terms proportional to $\sin(2\pi kz/d)$, $k \in \mathbb{N}$, vanish, because $n(z)$ and $S_2(z)$ are even functions.

The four order parameters in Eq. (3.5) allow one to distinguish between the following distinct bulk phases:

- isotropic fluid: $n_0 \neq 0, S_{20} = W_0 = W_2 = 0$,
- nematic fluid: $n_0 \neq 0, S_{20} \neq 0, W_0 = W_2 = 0$,
- smectic-A fluid: $n_0 \neq 0, S_{20} \neq 0, W_0 \neq 0, W_2 \neq 0$.

State points within a stable bulk phase maximize $-\Omega[\varrho]$ so that for the pressure p one has $p = -\frac{1}{\mathcal{V}}\Omega[\varrho^{\text{eq}}] \geq -\frac{1}{\mathcal{V}}\Omega[\varrho]$. At phase coexistence distinct sets of order parameters give rise to the same value of the reduced pressure:

$$\begin{aligned} p^*(T, \mu, d) &:= -\frac{\beta\Omega[\varrho^{\text{eq}}]}{\mathcal{V}} \\ &= n_0 + \frac{1}{4\mathcal{V}_d} \int_{\mathcal{V}_d} d^3r n^{\text{eq}}(\mathbf{r}) [\zeta_0(\mathbf{r}) + S_2^{\text{eq}}(\mathbf{r})\zeta_2(\mathbf{r})] \\ &\quad - n_0 \frac{\partial_{Q_0}\mathcal{J}(Q_0)}{2\mathcal{V}_d} \int_{\mathcal{V}_d} d^3r' \int_{\mathcal{S}} d^2\omega' \bar{\varrho}(\mathbf{r}', \boldsymbol{\omega}') \times \\ &\quad \int_{\mathcal{V}} d^3r'' \int_{\mathcal{S}} d^2\omega'' \bar{\varrho}(\mathbf{r}'', \boldsymbol{\omega}'') f_M(\mathbf{r}' - \mathbf{r}'', \boldsymbol{\omega}', \boldsymbol{\omega}''), \end{aligned} \quad (3.8)$$

where ζ_l , $l = 0, 2$, are the coefficients in the expansion of the effective one-particle potential $\beta\psi$ (Eq. (2.18)) in terms of Legendre polynomials. The derivation of Eq. (3.8) is provided in Appendix C. The equilibrium value of d maximizes $p^*(T, \mu, d)$ for fixed

temperature and chemical potential, provided its value is larger than for any isotropic or nematic phase for the same state (T, μ) :

$$\left. \frac{\partial p^*(T, \mu, d)}{\partial d} \right|_{T, \mu} = 0. \quad (3.9)$$

Under these conditions a smectic phase with layer spacing d is the stable phase.

Later on dimensionless quantities are utilized in order to discuss the results of the present study in a convenient manner. Any state point (T^*, μ^*) is determined by the reduced temperature $T^* := kT/\varepsilon_0$, where ε_0 is the Gay-Berne interaction strength (see Eq. (2.4)), and the reduced chemical potential $\mu^* := \beta\mu - \ln(4\pi\Lambda^3)$. Any (number) density distribution $n(\mathbf{r})$ (Eq. (2.19)) is referred to by the packing fraction $\eta(\mathbf{r})$ via

$$\eta = n LR^2\pi/6. \quad (3.10)$$

Thus, the mean number density n_0 within one (bulk) smectic layer is represented by the corresponding mean packing fraction $\eta_0 = n_0 LR^2\pi/6$.

3.2.3. Crystallization

The DFT formalism, presented so far, captures isotropic, nematic, and smectic-A phases (see Secs. 2.2, 3.2.1 and 3.2.2). However, for sufficiently low temperatures and sufficiently high densities one expects crystallization to occur. As will be discussed in Sec. 3.3, the present DFT formalism predicts distinct variants of smectic-A phases to be stable at large densities (compare the phase diagrams in Figs. 3.2, 3.4, and 3.5). In order to assess the stability of those smectic-A-type phases with respect to crystallization, an approach similar to that used in investigations of melting and freezing in colloidal suspensions (see, e.g., Ref. [81] for a review) is followed. To this end, consider an expansion of the grand potential functional $\beta\Omega[\varrho]$ in terms of number density profiles ϱ around the value ϱ_N of a uniform nematic phase. Hence, the reference fluid is homogeneous but shows orientational order. For simplicity, all particles are perfectly aligned with the director, which, without loss of generality, points into the z -direction. Thus, the value of the grand potential around the homogeneous reference density ϱ_N of the nematic fluid is

given by the following expansion [5]:

$$\begin{aligned} \beta\Omega[\varrho] &= \beta\Omega[\varrho_N] + \int_{\mathcal{V}} d^3r \varrho(\mathbf{r}) \ln \left(\frac{\varrho(\mathbf{r})}{\varrho_N} \right) \\ &\quad - \frac{1}{2} \int_{\mathcal{V}} d^3r \int_{\mathcal{V}} d^3r' c^{(2)}(\mathbf{r} - \mathbf{r}') \Delta\varrho(\mathbf{r}) \Delta\varrho(\mathbf{r}') \\ &\quad + \mathcal{O}(\Delta\varrho^3), \end{aligned} \tag{3.11}$$

where $c^{(2)}(\mathbf{r} - \mathbf{r}')$ is the (two-particle) direct correlation function and $\Delta\varrho(\mathbf{r}) := \varrho(\mathbf{r}) - \varrho_N$ gives the deviation of the density at position \mathbf{r} from the homogeneous density ϱ_N . Note, that considering a perfectly aligned system allows one to disregard the orientational degrees of freedom in Eq. (3.11). In order to proceed the following substitution will be performed:

$$\begin{aligned} & - \frac{1}{2} \int_{\mathcal{V}} d^3r \int_{\mathcal{V}} d^3r' c^{(2)}(\mathbf{r} - \mathbf{r}') \Delta\varrho(\mathbf{r}) \Delta\varrho(\mathbf{r}') + \mathcal{O}(\Delta\varrho^3) \\ =: & - \frac{1}{2} \int_{\mathcal{V}} d^3r \int_{\mathcal{V}} d^3r' \bar{c}^{(2)}(\mathbf{r} - \mathbf{r}') \Delta\varrho(\mathbf{r}) \Delta\varrho(\mathbf{r}'), \end{aligned} \tag{3.12}$$

where the second order term, involving the direct correlation function $c^{(2)}$, and the higher order terms of Eq. (3.11) are replaced by an effective description of the direct correlation function $\bar{c}^{(2)}$. The motivation for using an effective direct correlation function $\bar{c}^{(2)}$ (Eq. (3.12)) is to avoid evaluating terms $\propto \mathcal{O}(\Delta\varrho^3)$ in Eq. (3.11). However, simply truncating the series at second order and using the direct correlation function $c^{(2)}(\mathbf{r} - \mathbf{r}') := -\frac{\delta^2 \mathcal{F}[\varrho]}{\delta\varrho(\mathbf{r})\delta\varrho(\mathbf{r}')}$ from Eqs. (2.10), (2.15), (2.17), and (2.18) leads to unphysical results (in particular one observes stable columnar phases, which in the present case of calamitic mesogenes [4] appear to be an artifact), due to the absence of the higher order terms. It turns out that using a second order approach in the spirit of Onsager [47] in order to incorporate the hard-core interactions cures this defect. It should be emphasized, that this approach is rather simplistic and not intended to yield quantitatively precise results. However, it allows one to estimate the onset of crystallization consistently with the DFT approach described in Secs. 2.2 and 3.2.1, because the Parsons-Lee approach used (Eq. (2.15)) can be understood as a modification of the Onsager functional. Thus the following form of the direct correlation function is chosen, in order to

keep the effective description consistent with the formalism of Sec. 2.2:

$$\begin{aligned} \bar{c}^{(2)}(\mathbf{r} - \mathbf{r}') &= -f_M(\mathbf{r} - \mathbf{r}', \hat{\mathbf{z}}, \hat{\mathbf{z}}) + \\ &(1 + f_M(\mathbf{r} - \mathbf{r}', \hat{\mathbf{z}}, \hat{\mathbf{z}}))\beta U(\mathbf{r} - \mathbf{r}', \hat{\mathbf{z}}, \hat{\mathbf{z}}). \end{aligned} \quad (3.13)$$

The crystalline density profile will be described by a superposition of Gaussians [81], which are centered at the sites $\mathbf{R} = \mathbf{R}_{\parallel} + \mathbf{R}_{\perp}$ of a three-dimensional hexagonal lattice \mathcal{R} :

$$\begin{aligned} \varrho(\mathbf{r}) &= \frac{\alpha_{\perp}}{\pi} \sqrt{\frac{\alpha_{\parallel}}{\pi}} \sum_{\mathbf{R} \in \mathcal{R}} \exp(-\alpha_{\perp}(\mathbf{r}_{\perp} - \mathbf{R}_{\perp})^2) \times \\ &\exp(-\alpha_{\parallel}(\mathbf{r}_{\parallel} - \mathbf{R}_{\parallel})^2), \end{aligned} \quad (3.14)$$

where \mathbf{r}_{\parallel} and \mathbf{R}_{\parallel} are the projection of the position \mathbf{r} and of the lattice site vector \mathbf{R} , respectively, onto the z -direction, while \mathbf{r}_{\perp} and \mathbf{R}_{\perp} are the respective projections onto the x - y -plane. The Gaussians are described by two parameters: $1/(2\alpha_{\parallel})$ is the mean-square displacement in z -direction, while $1/\alpha_{\perp}$ is the mean-square displacement in lateral direction (perpendicular to the z -direction and parallel to the x - y -plane). It is worth mentioning that the definitions of the mean-square displacements $1/(2\alpha_{\parallel})$ and $1/\alpha_{\perp}$ differ by a factor of $1/2$, due to the different dimensionality of the respective Gaussian contributions, which is one-dimensional for $1/(2\alpha_{\parallel})$ and two-dimensional for $1/\alpha_{\perp}$. The hexagonal lattice \mathcal{R} is defined by its primitive vectors $\mathbf{a}_1 = a(\sqrt{3}\hat{\mathbf{x}} + \hat{\mathbf{y}})/2$, $\mathbf{a}_2 = a(\hat{\mathbf{y}} - \sqrt{3}\hat{\mathbf{x}})/2$, and $\mathbf{a}_3 = L\hat{\mathbf{z}}$. The lateral nearest neighbor spacing a is related to the volume V_c of the elementary cell via $V_c = \sqrt{3}a^2L/2$. Note, that the height of the elementary cell is chosen to be equal to the particle length L , which leads to a smectic layer spacing $d = L$. This choice of the density profile allows one to represent the following four types of bulk phases:

- nematic fluid: $\alpha_{\parallel} = \alpha_{\perp} = 0$,
- smectic-A fluid: $\alpha_{\parallel} > 0, \alpha_{\perp} = 0$,
- hexagonal columnar phase: $\alpha_{\parallel} = 0, \alpha_{\perp} > 0$,
- hexagonal crystal: $\alpha_{\parallel} > 0, \alpha_{\perp} > 0$.

The motivation for choosing a three-dimensional hexagonal lattice structure is, on one hand, that the smectic-A phase as well as a crystalline structure can be recaptured by

tuning the parameters α_{\parallel} and α_{\perp} accordingly (see above). On the other hand, because the particles are taken to be perfectly aligned with the z -direction, their cross-sections parallel to the x - y -plane are circles. Therefore a hexagonal structure perpendicular to the x - y -plane appears to be a plausible candidate. In order to calculate $\beta\Omega[\varrho]$ in Eq. (3.11), Eq. (3.12) has to be evaluated, which can be written as

$$\begin{aligned} & -\frac{1}{2} \int_{\mathcal{V}} d^3r \int_{\mathcal{V}} d^3r' \bar{c}^{(2)}(\mathbf{r} - \mathbf{r}') \Delta\varrho(\mathbf{r}) \Delta\varrho(\mathbf{r}') = \\ & -\frac{1}{2} \varrho_N^2 \mathcal{V} \sum_{\mathbf{G} \in \mathcal{G} \setminus \{0\}} \hat{c}^{(2)}(\mathbf{G}) \exp\left(-\frac{\mathbf{G}_{\perp}^2}{2\alpha_{\perp}} - \frac{\mathbf{G}_{\parallel}^2}{2\alpha_{\parallel}}\right), \end{aligned} \quad (3.15)$$

where $\mathbf{G} = \mathbf{G}_{\parallel} + \mathbf{G}_{\perp}$ denotes a site of the reciprocal lattice \mathcal{G} of \mathcal{R} and $\hat{c}^{(2)}(\mathbf{G})$ is the Fourier transform of the direct correlation function (Eq. (3.13)). In Eq. (3.15) the Fourier representation of $\Delta\varrho(\mathbf{r})$ has been used:

$$\Delta\varrho(\mathbf{r}) = \varrho_N \sum_{\mathbf{G} \in \mathcal{G} \setminus \{0\}} \exp\left(i\mathbf{G} \cdot \mathbf{r} - \frac{\mathbf{G}_{\perp}^2}{4\alpha_{\perp}} - \frac{\mathbf{G}_{\parallel}^2}{4\alpha_{\parallel}}\right). \quad (3.16)$$

Note, that the mean density of the inhomogeneous fluid described by Eq. (3.14) is equal to the density ϱ_N of the homogeneous (nematic) reference fluid. In order to assess the stability of the four aforementioned types of phases for a given reduced temperature $T^* = kT/\varepsilon_0$, where ε_0 is the interaction strength of the Gay-Berne potential U_{GB} (see Eq. (2.4)), and density ϱ_N , i.e., for a given point in the phase diagrams shown in Figs. 3.2, 3.4, and 3.5, the difference of the grand potential density $\beta\Omega[\varrho]/\mathcal{V}$ (Eq. (3.11) with Eqs. (3.12) and (3.15)) from the value $\beta\Omega[\varrho_N]/\mathcal{V}$ of the homogeneous nematic reference fluid is evaluated for $\alpha_{\perp} \geq 0$ and $\alpha_{\parallel} \geq 0$:

$$\begin{aligned} \frac{\Delta\beta\Omega}{\mathcal{V}} & := \frac{\beta\Omega[\varrho] - \beta\Omega[\varrho_N]}{\mathcal{V}} = \frac{1}{\mathcal{V}} \int_{\mathcal{V}} d^3r \varrho(\mathbf{r}) \ln\left(\frac{\varrho(\mathbf{r})}{\varrho_N}\right) \\ & - \frac{1}{2} \varrho_N^2 \sum_{\mathbf{G} \in \mathcal{G} \setminus \{0\}} \hat{c}^{(2)}(\mathbf{G}) \exp\left(-\frac{\mathbf{G}_{\perp}^2}{2\alpha_{\perp}} - \frac{\mathbf{G}_{\parallel}^2}{2\alpha_{\parallel}}\right). \end{aligned} \quad (3.17)$$

In order to illustrate, how the onset of crystallization is determined, consider the following set of pair potential parameters: $L/R = 4$, $\varepsilon_R/\varepsilon_L = 2$, $D/R = 0.9$, $\lambda_D/R = 5$, and $\gamma/(R\varepsilon_0) = 0.045$. Eq. (3.17) is evaluated numerically for a set of four ther-

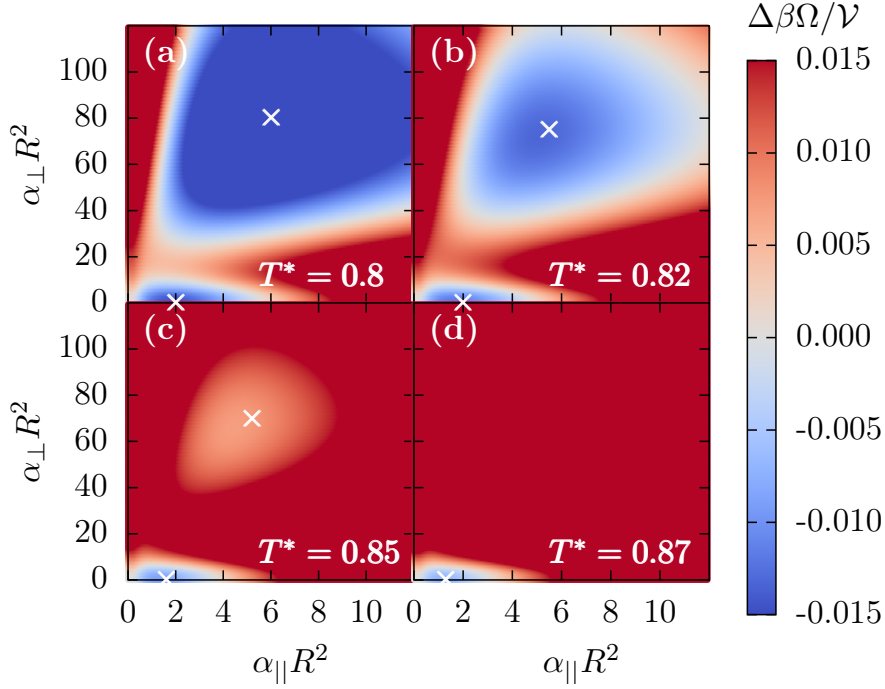


FIGURE 3.1.: Grand potential density $\Delta\beta\Omega/\nu$ (Eq. (3.17)) of spatially non-uniform structures (crystalline or smectic, Eq. (3.14)) in the range $\alpha_{\perp}R^2 \in [0, 120]$ and $\alpha_{\parallel}R^2 \in [0, 12]$ relative to that for a spatially uniform nematic fluid of the same density at packing fraction $\eta_N = 0.42$ and temperatures $T^* = 0.8, 0.82, 0.85$, and 0.87 . Crosses (\times) denote local minima of $\Delta\beta\Omega/\nu$. By construction one has $\Delta\beta\Omega/\nu = 0$ for $\alpha_{\parallel} = \alpha_{\perp} = 0$. For $T^* = 0.8$ (panel (a)) the global minimum of $\Delta\beta\Omega/\nu$ is at $(\alpha_{\parallel}R^2 \approx 6, \alpha_{\perp}R^2 \approx 80)$ which is a hexagonal crystal structure. The S_A phase with $(\alpha_{\parallel}R^2 \approx 2, \alpha_{\perp}R^2 = 0)$ is metastable. By increasing temperature one finds coexistence of the S_A phase and of the crystal to occur close to $T^* = 0.82$ (panel (b)) and for larger temperature $T^* = 0.85, 0.87$ (panels (c) and (d)) the S_A phase becomes stable.

modynamic state points with packing fraction $\eta_N = 0.42$ and reduced temperatures $T^* \in \{0.8, 0.82, 0.85, 0.87\}$. The values of $\Delta\beta\Omega/\nu$ for $\alpha_{\perp}R^2 \in [0, 120]$ and $\alpha_{\parallel}R^2 \in [0, 12]$ are shown in Fig. 3.1. For $T^* = 0.87$ and 0.85 the smectic-A phase is stable with respect to crystallization, while for $T^* = 0.8$ it becomes unstable with respect to a hexagonal crystalline phase. $T^* = 0.82$ is close to coexistence of the smectic-A phase and the hexagonal crystal, because in this case the grand potential $\beta\Omega[\rho]$ exhibits two almost equally deep local minima corresponding to these two phases. Repeating this procedure for various packing fractions η_N allows one to detect the phase transition from a stable

smectic-A phase to a stable crystal.

Alternatively, the location of the melting of the hexagonal lattice structure in lateral direction can be estimated by invoking a Lindemann criterion [82–84]. It states that if the scaled root mean square displacement $1/(a\sqrt{\alpha_\perp})$ of the (lateral) hexagonal lattice with lattice spacing $\frac{a}{R} = \sqrt{\frac{\pi}{3\sqrt{3}\eta_0}}$ and packing fraction η_0 exceeds a certain threshold value δ (the so-called critical Lindemann parameter) the lattice vibrations are sufficiently strong to destroy the (lateral) lattice structure. Evaluating $1/(a\sqrt{\alpha_\perp})$ from the minimum of $\Delta\beta\Omega/\mathcal{V}$ (Eq. (3.17)) corresponding to a three-dimensional hexagonal lattice structure (Fig. 3.1) along the (pink) melting curves in Figs. 3.4 and 3.5 yields for $\eta_0 \lesssim 0.4$ a lateral root mean square displacement $1/(a\sqrt{\alpha_\perp}) \gtrsim 0.1$ and for $\eta_0 \gtrsim 0.4$ a lateral root mean square displacement $1/(a\sqrt{\alpha_\perp}) \lesssim 0.1$. Thus, for the widely used, common critical Lindemann parameter $\delta \approx 0.1$ the (pink) melting curves shown in Figs. 3.4 and 3.5 lie below (above) those respective melting curves, which have been obtained by applying the Lindemann criterion, for packing fractions η_0 larger (smaller) than 0.4. Hence the Lindemann criterion $\delta \approx 0.1$ leads to the (pink) melting curves in Figs. 3.4 and 3.5 only for $\eta_0 \approx 0.4$; otherwise the critical Lindemann parameter has to be considered as (monotonically decreasing) function of the packing fraction: $\delta(\eta_0) \in [0.06, 0.2]$ for $\eta_0 \in [0.3, 0.49]$. This result leads to the conclusion that the Lindemann criterion, assuming a constant critical Lindemann parameter $\delta = \text{const.}$, is not applicable here.

3.2.4. Grand canonical Monte Carlo simulation

Grand canonical Monte Carlo (MC) simulations have been carried out, based on the molecular model introduced in Sec. 2.1. The simulations are performed in a cubic simulation box of side length $V^{1/3}/R \in \{12.75, 13.2, 15.0\}$, employing periodic boundary conditions. Standard Metropolis importance sampling of the grand canonical Boltzmann distribution $P(\chi) \propto \exp(\beta\mu N[\chi] - \beta H[\chi])$ with the chemical potential μ , the total number of ILC molecules $N[\chi]$, and the Hamiltonian

$$\beta H[\chi] = \sum_{\substack{i,j \\ j>i}}^N \beta U(\mathbf{r}_{ij}, \boldsymbol{\omega}_i, \boldsymbol{\omega}_j) \Theta(R_{\text{cut}} - |\mathbf{r}_{ij}|) \quad (3.18)$$

which governs the set $\{\chi\}$ of all configurations. The pair interaction $U(\mathbf{r}_{ij}, \boldsymbol{\omega}_i, \boldsymbol{\omega}_j)$ (Eq. (2.1)) is truncated at the cut-off distance $|\mathbf{r}_{ij}| = R_{\text{cut}} < V^{1/3}/2$. Each simulation run consists of $N^{\text{mon}} = 0.2 - 1 \times 10^6$ MC moves, from which the relevant observables

are monitored (see below). Additionally, between two consecutive monitoring moves ca. $N^{\text{relax}} = 500$ relaxation moves are included in order to reduce correlations between successive (monitored) configurations along the MC trajectory. Thus, a simulation consists of $N^{\text{tot}} = N^{\text{mon}} \times N^{\text{relax}} = 1 - 5 \times 10^8$ simulation moves in total. Each MC move can be either a translation and rotation of one particle (randomly chosen with probability $P_{\text{t\&r}}$), an insertion of one particle of orientation $\boldsymbol{\omega}$ at position \mathbf{r} (chosen with probability $(1 - P_{\text{t\&r}})/2$), or a removal of one particle (chosen with probability $(1 - P_{\text{t\&r}})/2$). In the case of translation and rotation, the trial orientation is chosen randomly within the interval $0 \leq \vartheta \leq \vartheta_{\text{max}}$ around the orientation of the particle under consideration. In order to optimize the acceptance rate of the trial configurations along the MC trajectory the displacement volume v , the maximum polar angle ϑ_{max} , and the probability $P_{\text{t\&r}}$ have been adapted accordingly. The initial configuration for each simulation is isotropic, such that the system can freely form any kind of structure.

The spatial arrangement of the particles can be investigated via the local number density

$$\rho^{\text{loc}}(\mathbf{r}) := l^{-3} \langle N^{\text{loc}}(\mathbf{r}, [\chi]) \rangle, \quad (3.19)$$

where $N^{\text{loc}}(\mathbf{r}, [\chi])$ is the number of particles for a given configuration χ in a cube-like partial volume l^3 of the simulation box located at position \mathbf{r} ; $\langle \dots \rangle$ denotes the thermal average. Upon monitoring the local density on a simple cubic lattice of sample points within the simulation box of volume V the structure of the fluid is inferred.

The degree of orientational order can be characterized by considering the local orientational order parameter

$$S_2^{\text{loc}}(\mathbf{r}) := \frac{3}{2} \left\langle \frac{\sum_{i=1}^{N^{\text{loc}}} (\boldsymbol{\omega}_i \cdot \hat{\mathbf{n}}[\chi])^2}{N^{\text{loc}}(\mathbf{r}, [\chi])} \right\rangle - \frac{1}{2}, \quad (3.20)$$

where, for a given configuration χ , $\boldsymbol{\omega}_i \cdot \hat{\mathbf{n}}$ is the projection of the long axis $\boldsymbol{\omega}_i$ of the i -th particle onto the global director $\hat{\mathbf{n}}[\chi]$. Here, ‘‘global’’ means that all particles within the simulation box V are considered, while ‘‘local’’ means that only particles in the relevant partial volume l^3 are considered. The director $\hat{\mathbf{n}}[\chi]$ corresponding to configuration χ is obtained by calculating the eigenvector corresponding to the largest eigenvalue of the orientational ordering matrix (i.e., the tensor order parameter) [4] for the considered configuration χ :

$$Q_{ab}[\chi] := \frac{3}{2N[\chi]} \sum_{i=1}^N (\boldsymbol{\omega}_i)_a (\boldsymbol{\omega}_i)_b - \frac{\delta_{ab}}{2}, \quad (3.21)$$

where $(\boldsymbol{\omega}_i)_a$ denotes the a -th component of vector $\boldsymbol{\omega}_i$. For $S_2^{\text{loc}}(\mathbf{r}) \lesssim 1$ particles located at \mathbf{r} are predominantly aligned with the director $\hat{\mathbf{n}}$, while for $S_2^{\text{loc}}(\mathbf{r}) \gtrsim -0.5$ the particles are predominantly perpendicular to the director. For $|S_2^{\text{loc}}(\mathbf{r})| \ll 1$, particles at \mathbf{r} do not exhibit orientational ordering.

3.3. Results

3.3.1. Phase diagrams

Comparison between OLCs and ILCs

The phase behavior of ionic liquid crystals (ILCs) and ordinary liquid crystals (OLCs) is studied by considering their respective phase diagrams in the (η_0, T^*) plane. In Fig. 3.2(a) uncharged ordinary liquid crystals (OLCs) of length-to-breadth ratio $L/R = 2$ and with Gay-Berne anisotropy parameter $\varepsilon_R/\varepsilon_L = 2$ are considered. In Fig. 3.2(b) the phase behavior of ILCs is shown, described by $L/R = 2, \varepsilon_R/\varepsilon_L = 2, D/R = 0.9, \lambda_D/R = 5$, and $\gamma/(R\varepsilon_0) = 0.0045$. In both cases, at low packing fractions and at low temperatures, coexistence of a dilute and a dense isotropic phase is observed, which is referred to as liquid (L)-vapor (V) coexistence. One finds that the critical temperature is lowered for the ILC fluid, which is a well-known observation for ionic systems [29]; here it is induced by the enhanced repulsion between the ILC molecules. Although low critical temperatures are a general feature of Coulombic systems, the precise location of the critical point is very sensitive to the details of the model and the method used [29]. For both types of fluids, increasing the mean packing fraction η_0 leads to a first-order phase transition to a smectic phase, in agreement with the corresponding results in Ref. [71]. Remarkably, at sufficiently low temperatures, before forming an ordinary smectic-A structure (S_A), a smectic phase appears in which the particles are oriented predominantly perpendicular to the director of the smectic phase, i.e., the z -direction along which the periodically oscillating density occurs. Since this behavior leads to a layer spacing which is comparable to the diameter R of the particles and therefore is *narrower* (N) than in an ordinary S_A phase, in which the layer spacing is comparable to the length L of the particles, this smectic structure is referred to as the S_{AN} phase. (Figure 3.3 provides a comparison of the structure of both types of smectic phases, S_{AN} and S_A , for particles with length-to-breadth ratio $L/R = 2$.) However, at high temperatures a first-order phase transition occurs directly from the liquid (L) to the S_A phase. The low- and the high-temperature

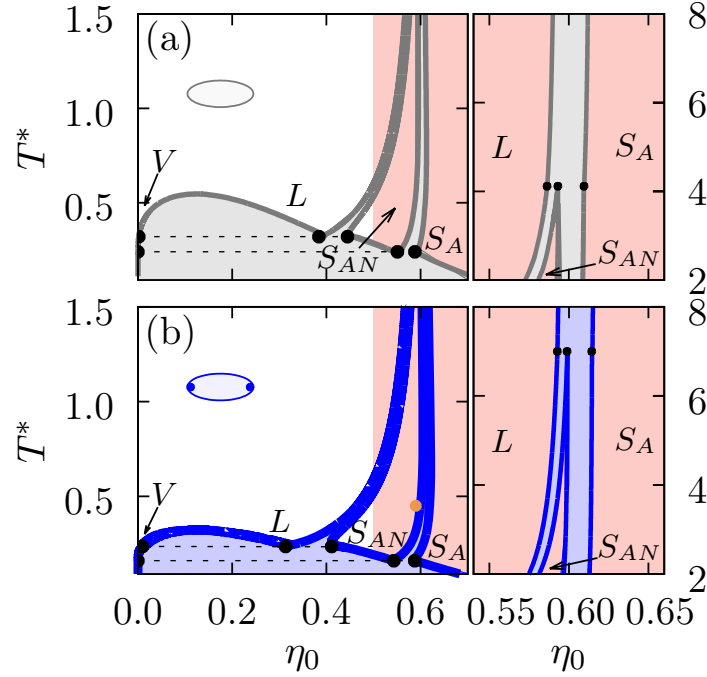


FIGURE 3.2.: Panel (a) shows the phase diagram for ordinary liquid crystals (OLCs) with $L/R = 2$ and $\varepsilon_R/\varepsilon_L = 2$. Panel (b) corresponds to ILCs described by $L/R = 2$, $\varepsilon_R/\varepsilon_L = 2$, $D/R = 0.9$, $\lambda_D/R = 5$, and $\gamma/(R\varepsilon_0) = 0.0045$. The black dots connected by a dashed line in the left panels indicate three-phase coexistence of the vapor (V), the liquid (L), and the narrow smectic S_{AN} phase, and three-phase coexistence of the vapor, the S_{AN} , and the ordinary smectic S_A phase, respectively. The black dots in the right panels indicate the location of L - S_{AN} - S_A three-phase coexistence (here the connection by dashed lines is omitted) which occurs at the triple point temperature $T_t^* \approx 4.11$ for the ordinary liquid crystals and at $T_t^* \approx 7.0$ for the ILC fluid. The orange dot (●) marks the state point ($T^* = 0.45$, $\mu^* = 20$) in the ILC phase diagram for which, cf., Fig. 3.7 provides the corresponding order parameter profiles. The salmon-colored area represents the region $\eta_0 \geq 0.5$ of the phase diagram for which the lateral spacing in between neighboring particles on a hexagonal lattice becomes less than 10% of the particle diameter R , i.e., $a/R \leq 1.1$. Thus, the particles are densely packed and previous simulations suggest the occurrence of crystallization in this high density regime [85]. According to the left panels the left bottom corner of the S_{AN} phase appears to be stable against crystallization.

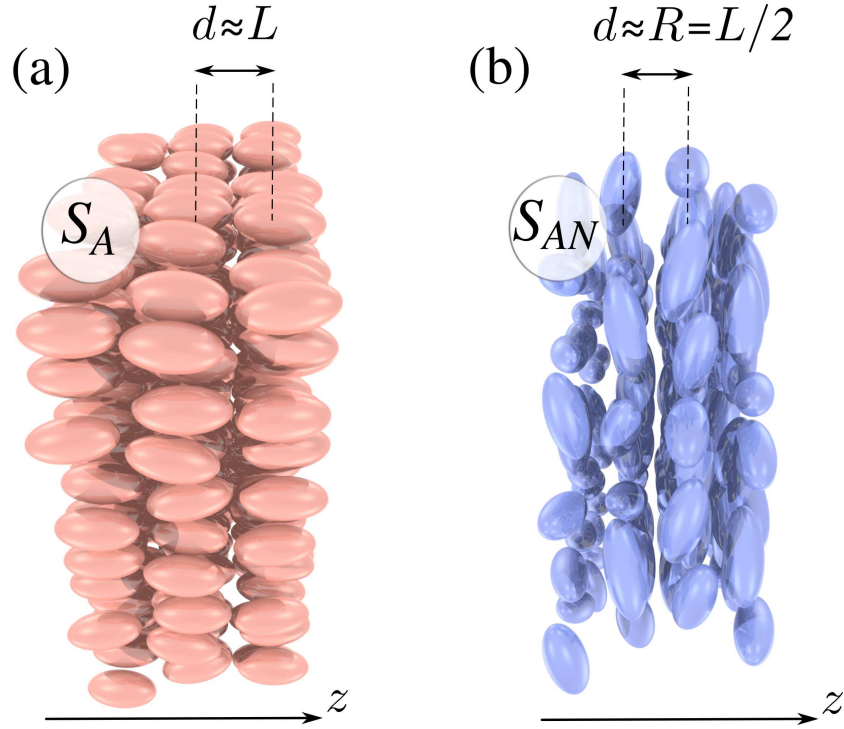


FIGURE 3.3.: Smectic configurations of particles with $L/R = 2$. Panel (a) depicts three layers of an ordinary smectic S_A phase for a system composed of particles of length-to-breadth ratio $L/R = 2$. The particles are mostly aligned with the layer normal (i.e., the z -direction), which leads to a smectic layer spacing comparable to the size of the particle length L , as expected for an ordinary S_A phase. Panel (b) represents a typical configuration of the S_{AN} phase for $L/R = 2$. Four smectic layers are shown in which the particles are oriented mainly perpendicular to the layer normal (i.e., the z -direction). However, they do not show a preferred orientation in the x - y -plane. This behavior leads to a layer spacing d which is comparable to the size of the particle diameter R . In order to clearly visualize the smectic layers of the S_{AN} phase, the diameter of the blue particles in panel (b) is reduced slightly. This leads to a small gap in between the smectic layers of this illustration. Note, that the phases shown in panel (a) and (b) could not be observed in simulations and thus the depicted configurations are not snapshots but have been composed artificially for illustration purposes.

regimes are separated by a triple point, indicated by the black dots in the respective plot of Fig. 3.2, at which the liquid (L), the narrow smectic (S_{AN}), and the ordinary smectic phase (S_A) coexist. For the ILC system the triple point temperature ($T_t^* \approx 7.0$)

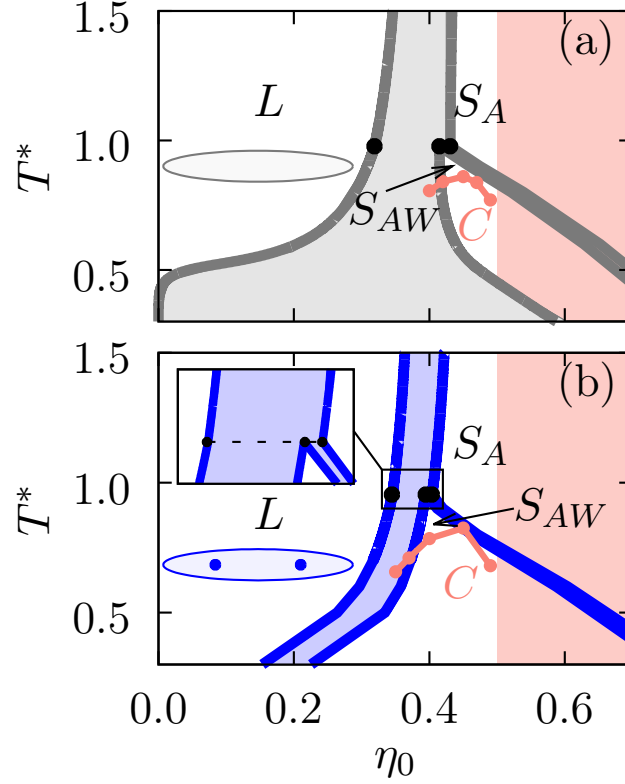


FIGURE 3.4.: Panel (a) shows the phase diagram for ordinary liquid crystals (OLCs) with $L/R = 4$, $\varepsilon_R/\varepsilon_L = 2$ and panel (b) for ionic liquid crystals described by $L/R = 4$, $\varepsilon_R/\varepsilon_L = 2$, $D/R = 0.9$, $\lambda_D/R = 5$, and $\gamma/(R\varepsilon_0) = 0.045$. The black dots visualize the location of L - S_{AW} - S_A three-phase coexistence. The inset in panel (b) gives an enlarged view of the vicinity of the triple point of the ILC fluid. The pink curve indicates the *onset* of crystallization (C), obtained by the method described in Sec. 3.2.3. Note, that this approach does not allow one to analyze two-phase regions involving the phase C , because it compares the grand potential minima associated with smectic-A and crystalline phases for given (η_0, T^*) . Like in Fig. 3.2, the salmon-colored area represents the region $\eta_0 \geq 0.5$ of the phase diagram for which the lateral spacing in between neighboring particles on a hexagonal lattice becomes less than 10% of the particle diameter R , i.e., $a/R \leq 1.1$. Hence, the particles are densely packed and previous simulations report the occurrence of a solid phase in this density regime [85].

is significantly higher than for the OLC ($T_t^* \approx 4.11$). Thus for ILCs the orientationally less-ordered smectic phase S_{AN} remains stable at temperatures which are higher than for

the (uncharged) ordinary liquid crystals. For large T^* the L - S_A coexistence curves coincide for ILCs and OLCs, because at high temperatures the (same) hard-core repulsion is the dominant interaction.

Since particles with length-to-breadth ratio $L/R = 2$ and Gay-Berne anisotropy parameter $\varepsilon_R/\varepsilon_L = 2$ exhibit a rather isotropic pair potential $U(\mathbf{r}_{12}, \boldsymbol{\omega}_1, \boldsymbol{\omega}_2)$, it is very likely that the occurrence of liquid-crystalline phases in such a system is an artifact of the DFT method described in Secs. 2.2 and 3.2.1, which is unable to capture the formation of genuine crystalline structures. For a hexagonal lattice structure the lateral lattice spacing $\frac{a}{R} = \sqrt{\frac{\pi}{3\sqrt{3}\eta_0}}$ (see Sec. 3.2.3) takes a value of $a/R \approx 1.1$ for $\eta_0 \approx 0.5$. Since this means that the free space $(a - R)/R$ in lateral direction in between neighboring particles on the hexagonal lattice is less than 10% of their diameter R , the particles are densely packed in the high density region $\eta_0 \geq 0.5$ and previous simulations [85] on systems of pure (i.e., uncharged) Gay-Berne particles of length-to-breadth ratio $L/R = 3$ report the occurrence of a solid phase for number densities $n_0 \gtrsim 0.32 R^{-3}$ (denoted as ϱ in Ref. [85]) which correspond to $\eta_0 = n_0 L R^2 \pi / 6 \gtrsim 0.5$ for $L/R = 3$. Thus, as is shown by the salmon-colored area in Fig. 3.2 the thermodynamically stable state points of the liquid crystalline phases S_A and S_{AN} lie almost completely inside this (expected) crystalline regime. The occurrence of two different types of “smectic” phases (i.e., S_A and S_{AN}) within the DFT approach of Secs. 2.2 and 3.2.1 can be a hint on the presence of several distinct kinds of crystalline phases in such systems, distinguishable either by their lattice structure or by the degree of orientational ordering. Within this interpretation of the phase diagrams in Fig. 3.2 the S_A phase would be the analogue of a crystalline phase with considerable orientational ordering of the lattice particles, while the S_{AN} phase mimics a crystalline phase with a lower degree of orientational ordering (i.e., a plastic crystal).

Figure 3.4 provides another comparison between (a) uncharged liquid crystal molecules and (b) ILC molecules with $D/R = 0.9$, $\lambda_D/R = 5$, $\gamma/(R\varepsilon_0) = 0.045$; both types of molecules share the same length-to-breadth ratio $L/R = 4$ and the ratio $\varepsilon_R/\varepsilon_L = 2$. These particles are twice as elongated as those in Fig. 3.2. In this case there is no L - V coexistence; however, for the uncharged liquid crystal (a) it is still metastable, giving rise to a shoulder-like shape of the left hand side of the liquid-smectic two-phase region indicated by the gray-colored area in Fig. 3.4(a). For the ILC fluid the liquid-smectic two-phase region (light-blue-colored area in Fig. 3.4(b)) is narrower compared to its counterpart for the ordinary liquid crystals. At low temperatures this gives rise to stability of smectic structures, with respect to the isotropic liquid phase, already at

smaller mean packing fractions η_0 . This is caused by the presence of the additional electrostatic repulsion which imposes an energetic penalty on a homogeneous liquid already at packing fractions which are smaller than the corresponding ones for ordinary liquid crystal fluids. Similar to the previous case of the shorter particles, two distinct types of smectic structures can be observed. At sufficiently low temperatures, before forming an ordinary smectic-A structure (S_A) upon increasing η_0 , a smectic phase is observed the layer spacing of which is considerably larger than in the high-temperature S_A phase. Remarkably, it shows an alternating structure in which a majority of the particles within the smectic layers is oriented predominantly parallel to the director and a minority of the particles is located in between the layers with an orientation which is predominantly perpendicular to the director. This novel structure shall be referred to as the S_{AW} phase, emphasizing the extraordinarily *wide* (w) layer spacing. Again three-phase coexistence occurs as indicated by black dots in the respective plots. It marks the transition to the high-temperature regime in which a first-order phase transition directly from the liquid to the S_A phase takes place. In both cases (Figs. 3.4(a) and (b)) the triple point temperature is about $T_t^* \approx 1.0$. Nevertheless, the S_{AW} phase has not been observed for ordinary liquid crystals in simulations or experiments, because commonly at low temperatures Gay-Berne fluids exhibit crystalline phases, as shown by previous studies [86]. In order to estimate the onset of crystallization in these systems, the coexistence of a S_A phase and a hexagonal lattice structure C , shown as pink curves in Fig. 3.4, has been calculated (by using the method of Sec. 3.2.3). It turns out that the onset of crystallization appears close to the S_A - S_{AW} transition for both cases in Fig. 3.4. This result suggests that at most in a small thermodynamic pocket the S_{AW} phase remains stable against crystallization. Considering the simplicity of the method used (see Sec. 3.2.3), which does not allow one to precisely determine the onset of crystallization, the stability of the S_{AW} for those two cases (a) and (b) seems to be an artifact of the approximations used. Thus, one cannot expect a genuine S_{AW} phase to occur for the two cases considered in Fig. 3.4, which is in agreement with previous findings. Nevertheless the S_{AW} phase can be stable for an ILC fluid, because the presence of the charges is capable to alter the bulk phase behavior significantly. In that regard, the influence of the location of the charges on the phase diagram is discussed in the next passage. It will be demonstrated that the stability of the S_{AW} phase is enhanced at higher temperatures for ILC molecules with charges at the tips. Moreover, the results of MC simulations will show that the S_{AW} phase is indeed observable for ILC fluids.

Finally it is worth mentioning that in order to study the onset of crystallization

quantitatively on a more precise level, one should consider a free energy functional which accounts for positional correlations more carefully than the present DFT approach. For instance, treating the hardcore interactions of anisotropic particles within *fundamental measure theory* [87–91] is an appropriate and promising approach.

Dependence on the location of the charges

In this passage the dependence of the ILC phase behavior on the position D of the particle charges for $L/R = 4$, $\varepsilon_R/\varepsilon_L = 2$, $\lambda_D/R = 5$, $\gamma/(R\varepsilon_0) = 0.045$ is investigated. Thus, compared to the case considered in Fig. 3.4(b) only the molecular charge distribution is changed, while all other model parameters are kept constant. Figure 3.5(a) shows the case of the two charges merged in the geometrical center of the molecule, i.e., $D/R = 0$. In Fig. 3.5(b) the two charges are located near the tips, i.e., $D/R = 1.8$. For $D/R = 0$ the phase diagram coincides almost quantitatively with the corresponding phase diagram in Fig. 3.4(b) for $D/R = 0.9$, besides a slight change in the location of the S_{AW} - S_A two-phase region. Thus, the change in the pair potential by moving the charges from the center to the moderate distance $D/R = 0.9$ turns out to be insufficient for a significant change of the phase behavior. However, moving the charges to the tips of the particles changes the shape of the pair potential significantly (Figs. 2.2(c) and (d)). This in turn leads to a considerable variation in the phase behavior. Figure 3.5(b) shows that for ILC molecules with charges at the tips ($D/R = 1.8$ and $L/R = 4$) the L - S_{AW} - S_A triple point (see the inset of Fig. 3.5(b) providing an enlarged view of the vicinity of the triple point) is shifted to a higher temperature $T_t^* \approx 1.22$. Thus the (low-temperature) wide smectic phase S_{AW} becomes stable at temperatures, which are higher than in the cases in Figs. 3.4 and 3.5(a). As before, the location of the onset of crystallization by employing the method of Sec. 3.2.3. The obtained results (pink curves in Fig. 3.5) show that, in the case of ILC molecules with charges being located right at the tips (panel (b)) the stable region of the S_{AW} phase is enhanced compared with the other cases (Figs. 3.4 and 3.5(a)), due to the higher L - S_{AW} - S_A triple point temperature. Hence, the S_{AW} phase can indeed be expected to occur for long thin ILC particles with charges located at the tips (Fig. 3.5(b)), whereas it is preempted by crystallization otherwise (Figs. 3.4 and 3.5(a)). If the charges are localized at the tips of the molecules, the smectic phase S_{AW} with wide layer spacing is stabilized in the intermediate temperature regime, i.e., in between the high temperature ordinary smectic S_A phase and crystalline structures C at low temperatures (at intermediate densities), which is due to the effective electro-

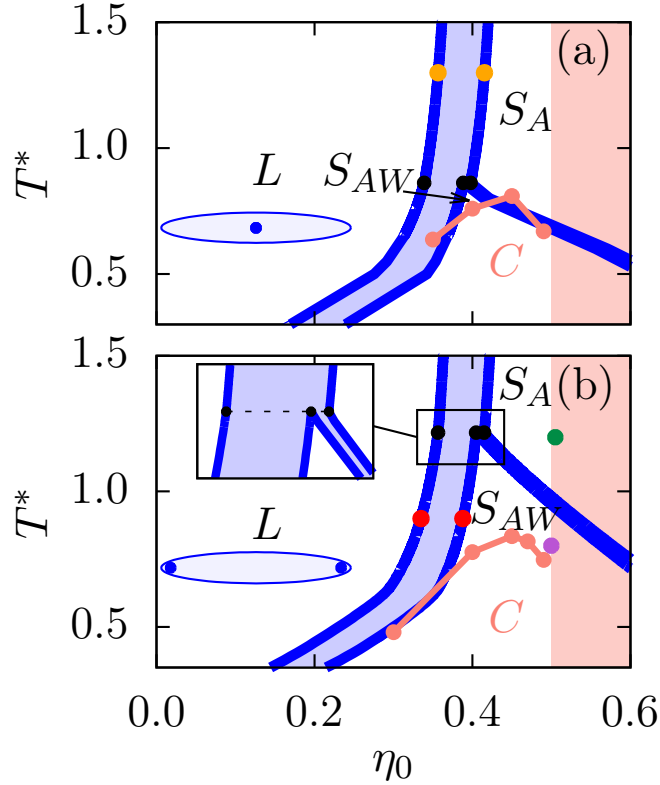


FIGURE 3.5.: Phase diagrams for ILCs with (a) $L/R = 4, \varepsilon_R/\varepsilon_L = 2, D/R = 0, \lambda_D/R = 5$, and $\gamma/(R\varepsilon_0) = 0.045$ and (b) $L/R = 4, \varepsilon_R/\varepsilon_L = 2, D/R = 1.8, \lambda_D/R = 5$, and $\gamma/(R\varepsilon_0) = 0.045$. The colored dots denote the state points $(T^*, \mu^*) = (0.8, 20)$ (\bullet , see, cf., Fig. 3.9) and $(1.2, 18)$ (\bullet , see, cf., Fig. 3.8), while the black dots indicate L - S_{AW} - S_A three-phase coexistence. The inset in panel (b) gives an enlarged view of the vicinity of the triple point. Like in Fig. 3.4, the pink curve indicates the onset of crystallization and the salmon-colored area represents the region $\eta_0 \geq 0.5$ of the phase diagram for which the lateral spacing in between neighboring particles on a hexagonal lattice becomes less than 10% of the particle diameter R , i.e., $a/R \leq 1.1$. Hence, the particles are densely packed and previous simulations report the occurrence of a solid phase in this density regime [85]. Note, that the orange dots (\bullet), respectively the red dots (\bullet), in panels (a) and (b) mark the coexisting states which are discussed in the context of isotropic-smectic interfaces in Chapter 4.

static repulsion of neighboring smectic layers. In the other cases, i.e., if the charges are localized close to the geometrical center or if there are no charges at all, the ordinary

smectic phase S_A with densely packed smectic layers ($d \approx L$) is entropically preferred over the wide smectic phase S_{AW} at intermediate temperatures (and intermediate packing fractions). Accordingly, in these cases, the S_{AW} phase is preferred over the ordinary smectic S_A phase only at temperatures below the freezing transition where the actually stable phase is the crystalline one.

Moreover, the latter case of ILCs with the charges at the tips has been studied by grand canonical Monte Carlo simulations. In Fig. 3.6 two configurations are shown which appear during simulations performed for $(T^*, \mu^*) = (0.6, 0.9)$ in panel (a), and for $(T^*, \mu^*) = (0.5, -2.6)$ in panel (b). Here the pair potential is described by $L/R = 4$, $\varepsilon_R/\varepsilon_L = 3$, $D/R = 1.8$, $\lambda_D/R = 5$, $\gamma/(R\varepsilon_0) = 0.045$, and $R_{\text{cut}}/R = 6$. The chemical potentials are chosen to be sufficiently large, such that in both cases the system forms a smectic structure. In panel (a), one observes an ordinary S_A phase according to which the particles are located in the smectic layers with a preferred orientation parallel to the director, which is parallel to the layer normal. Conversely, at the lower temperature $T^* = 0.5$ a different structure is observed, shown in panel (b), yielding an increased smectic layer spacing. The space in between the layers is populated by numerous particles which are preferentially oriented perpendicular to the layer normal. This is the same periodic structure which has been found within the present DFT analysis for the low-temperature S_{AW} phase (compare Fig. 3.5(b)). Furthermore, in agreement with the present theory, increasing the rescaled chemical potential μ^* at low but fixed temperature T^* , at sufficiently large packing fraction η_0 , a transition from the S_{AW} phase to the S_A phase is observed. By increasing μ^* the packing fraction is also increased and ultimately a dense packing of smectic layers, corresponding to the S_A phase, is preferred over the (wide) smectic S_{AW} phase. (More details about the simulational results are provided in the discussion in the next section.)

It is worth mentioning that a similar kind of structure has been reported for a system of hard discs interacting via an additional anisotropic Yukawa potential [92, 93]. In this canonical MC study a structure called *intergrowth texture* has been observed which shows a periodic structure of two alternating layers of particles. The directors of both layers are perpendicular to each other. Nevertheless, unlike the S_{AW} phase, the particles within each layer of an intergrowth texture are not localized. Thus they do not exhibit positional order in any direction and cannot be categorized as a smectic structure. In contrast to monodisperse systems, like in the present study, alternating smectic layer structures have already been observed in binary mixtures of particles with different geometries [94–97]. For such systems the alternating layer structure is driven by segregation of the two

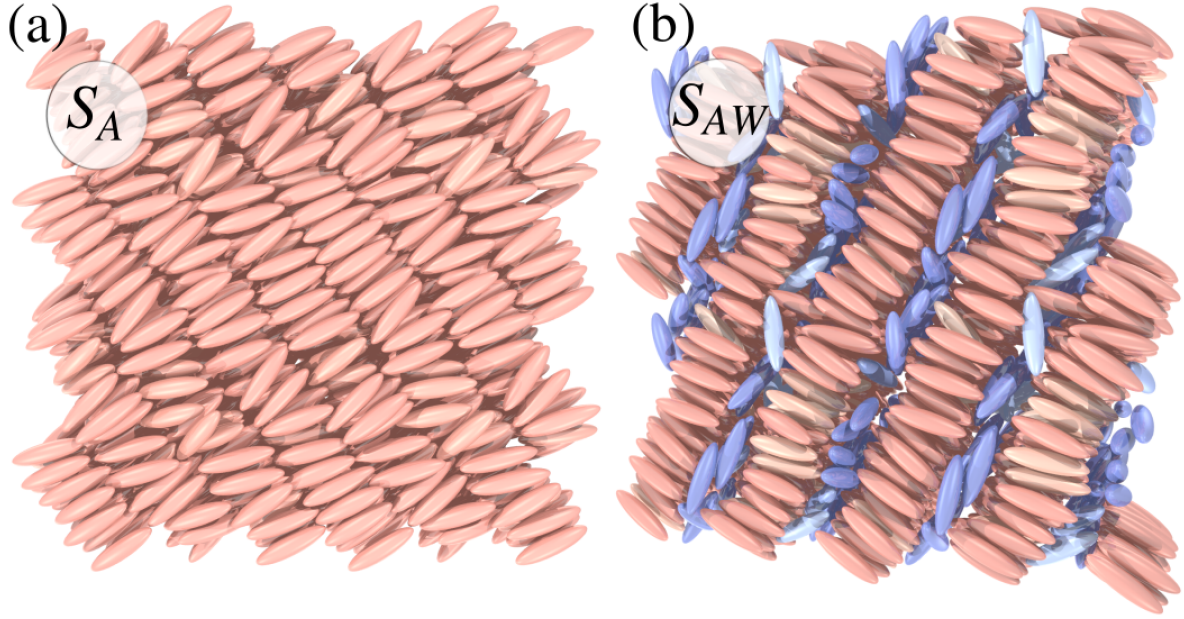


FIGURE 3.6.: Smectic configurations of ILCs with $L/R = 4$. Panel (a) shows a configuration appearing during a simulation performed at temperature $T^* = 0.6$; the chemical potential $\mu^* = 0.9$ is tuned such that $\eta_0 \approx 0.389$. Panel (b) depicts a configuration for $(T^*, \mu^*) = (0.5, -2.6)$ giving rise to $\eta_0 \approx 0.324$. For both (a) and (b) the parameters of the pair potential are given by $L/R = 4$, $\varepsilon_R/\varepsilon_L = 3$, $D/R = 1.8$, $\lambda_D/R = 5$, $\gamma/(R\varepsilon_0) = 0.045$, and $R_{\text{cut}}/R = 6$. At the higher temperature $T^* = 0.6$, one finds the ordinary smectic S_A phase, while for the lower temperature $T^* = 0.5$ the novel S_{AW} phase is observed. The latter is characterized by an alternating structure of particles such that within the smectic layers the particles are oriented parallel to the layer normal (pale pink particles) whereas the particles in between the layers are oriented perpendicularly to it but without lateral orientational order (blue particles).

particles species. It is worth mentioning, that due to fluctuations, even in the common S_A phase there is a non-vanishing probability to find particles in between the smectic layers with perpendicular orientation (see, e.g., Ref. [98]).

Finally, it is worth mentioning that particles with an electric quadrupole are known to form smectic S_C phases, in which the director is tilted with respect to the normal of the smectic layers (see, e.g., Ref. [99]). Such kind of liquid crystals are of particular interest for technological applications such as fast electro-optic displays, because those materials can be ferroelectric [100].

3.3.2. Variety of smectic structures

So far it has been illustrated how the ILC phase behavior varies as function of the parameters characterizing the pair potential. In particular, the occurring smectic phases show distinct layer spacings. In order to analyze the structures of the various smectic bulk phases in more detail, the density distributions in terms of the local packing fraction $\eta(z) = n(z)LR^2\pi/6$ and the spatially varying orientational order parameter $S_2(z)$ are discussed. (For the definitions of $\eta(z)$, $n(z)$ and $S_2(z)$, see Eqs. (2.19), (2.20), and (3.10).) Without loss of generality for bulk smectic-A phases the layer normal can be chosen to be parallel to the z -axis, i.e., $\hat{\mathbf{n}} = \hat{\mathbf{z}}$. Thus, $\mathbf{r} \cdot \hat{\mathbf{n}} = z$ and $\boldsymbol{\omega} \cdot \hat{\mathbf{n}} = \cos(\vartheta)$ with the polar angle ϑ . First, consider the smectic phase S_{AN} observed for $L/R = 2$, $\varepsilon_R/\varepsilon_L = 2$, $D/R = 0.9$, $\lambda_D/R = 5$, and $\gamma/(R\varepsilon_0) = 0.0045$ (compare Fig. 3.2(b)). In Fig. 3.7 the relevant profiles $\eta(z)$ and $S_2(z)$ are plotted for the state point $(T^*, \mu^*) = (0.45, 20.0)$ indicated in Fig. 3.2(b) (orange dot \bullet). The smectic layer spacing is $d/R \approx 1.2$; $S_2(z) \approx -0.4$ at $|z/d| \ll 1$ shows that within the smectic layers the particles are oriented mostly perpendicular to the layer normal $\hat{\mathbf{n}}$. This finding is plausible because $d/R \approx 1.2$ is much smaller than the length of the particles $L/R = 2$ which enforces the particles to tilt towards the smectic layers. The packing fraction profile $\eta(z)$ in Fig. 3.7 tells that the particles are strongly localized within the layers. The layer spacing does not vary significantly as function of temperature and of the chemical potential within the thermodynamic region of a stable smectic phase (according to the present DFT method). In the smectic S_{AN} phase the layer normal $\hat{\mathbf{n}}$ still points into the z -direction, so that the particles do not have a preferred lateral orientation, but they avoid an orientation parallel to the director. This behavior seems to be caused by the small length-to-breadth ratio $L/R = 2$ and the small value of the anisotropy parameter $\varepsilon_R/\varepsilon_L = 2$, which renders these particles relatively isotropic. This is even more pronounced in the case of the ILC fluid shown in Fig. 3.2(b) due to the additional electrostatic repulsion, which leads to a higher L - S_{AN} - S_A triple point temperature. For both smectic phases, S_A and S_{AN} , the layer spacing does not vary significantly as function of temperature and chemical potential within the thermodynamic region of a stable smectic phase. Again, it should be emphasized that for the shorter particles, described by $L/R = 2$ and $\varepsilon_R/\varepsilon_L = 2$, the stability of the liquid-crystalline phases S_A and S_{AN} is very likely to be an artifact of the method employed (see Sec. 2.2 and 3.2.1). The transition from an isotropic liquid phase to those mesophases occurs at large densities for which one already expects crystalline structures to emerge (see the discussion in Sec. 3.3.1).

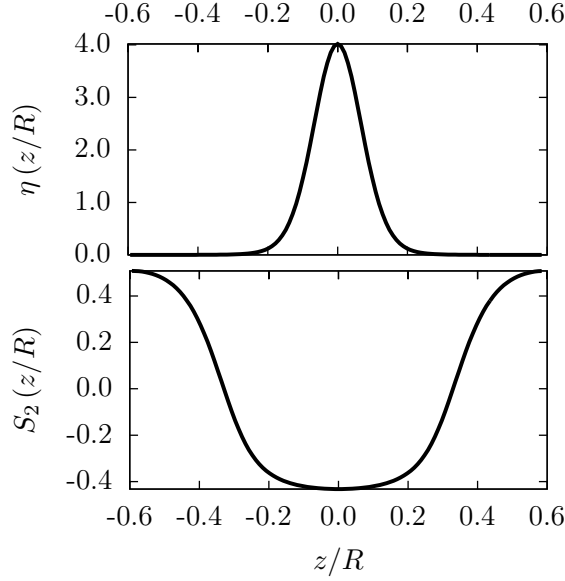


FIGURE 3.7.: Local packing fraction $\eta(z/R) = n(z/R)LR^2\pi/6$ and orientational order parameter $S_2(z/R) = \int_{\mathcal{S}} d^2\omega P_2(\cos(\vartheta))\varrho(z/R, \vartheta)/n(z/R)$ with the total number density $n(z/R) = \int_{\mathcal{S}} d^2\omega \varrho(z/R, \vartheta)$ displayed within one smectic layer of extent $d/R \approx 1.2$ for the state point $(T^*, \mu^*) = (0.45, 20)$ indicated in Fig. 3.2(a) (orange dot ●) for $L/R = 2, \varepsilon_R/\varepsilon_L = 2, D/R = 0.9, \lambda_D/R = 5$, and $\gamma/(R\varepsilon_0) = 0.0045$. The smectic layer spacing d is smaller than the length of the particles. At the center of the smectic layers the ILC molecules are oriented mainly perpendicular to the layer normal $\hat{\mathbf{n}}$ as one can infer from the negative value of the orientational order parameter $S_2(z = 0) \approx -0.4$ (S_{AN} phase). This is the same smectic structure as it has been sketched in Fig. 3.3(b). Note, without loss of generality for bulk smectic-A phases the layer normal can be chosen to be parallel to the z -axis, i.e., $\hat{\mathbf{n}} = \hat{\mathbf{z}}$.

Now, the ILC molecules described by the parameter set $L/R = 4, \varepsilon_R/\varepsilon_L = 2, D/R = 1.8, \lambda_D/R = 5$, and $\gamma/(R\varepsilon_0) = 0.045$ shall be considered, the phase diagram of which is shown in Fig. 3.5(b). In Fig. 3.5(b), at the state point $(T^*, \mu^*) = (1.2, 18)$ (green dot ●) the S_A phase is stable with a smectic layer spacing $d/R \approx 4.5$. The profiles of $\eta(z)$ and $S_2(z)$ are shown in Fig. 3.8. As expected for an ordinary smectic-A phase, the ILC molecules are located in the layers with an orientation predominantly parallel to the layer normal $\hat{\mathbf{n}}$. In contrast to the shorter particles discussed in Fig. 3.7, here the layer spacing $d/R \approx 4.5$ is comparable with the size of the length $L/R = 4$ of the particles and thus there is enough space for the particles to be aligned with the layer normal $\hat{\mathbf{n}} = \hat{\mathbf{z}}$.

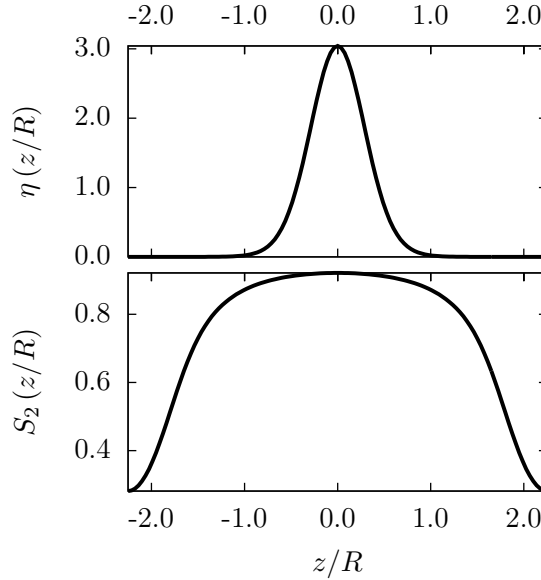


FIGURE 3.8.: Local packing fraction $\eta(z/R)$ and scalar orientational order parameter $S_2(z/R)$ within one period $d/R \approx 4.5$ at the state point $(T^*, \mu^*) = (1.2, 18)$ in Fig. 3.5(b) (green dot ●) for $L/R = 4$, $\varepsilon_R/\varepsilon_L = 2$, $D/R = 1.8$, $\lambda_D/R = 5$, and $\gamma/(R\varepsilon_0) = 0.045$. The ILC molecules are strongly localized in the center of the smectic layers where they are oriented mainly parallel to the smectic layer normal $\hat{\mathbf{n}} = \hat{\mathbf{z}}$ as indicated by the large positive value of the orientational order parameter $S_2(z = 0) \approx 0.9$ (ordinary S_A phase).

At low temperatures and large packing fractions, one finds the novel wide smectic S_{AW} phase. For $(T^*, \mu^*) = (0.8, 20)$ (magenta dot ● in Fig. 3.5(b)) this structure is shown in Fig. 3.9. The equilibrium layer spacing is $d/R \approx 7.7$, which is significantly larger than the one for the high-temperature ordinary smectic S_A phase (compare Fig. 3.8). The wide smectic S_{AW} phase shows an increased number of particles localized in between the layers, i.e., around $|z| \approx d/2$. They are oriented preferentially perpendicular to the layer normal $\hat{\mathbf{n}}$ (with no orientational ordering within the x - y -plane), while particles in the layers, i.e., for $|z/d| \ll 1$, are predominantly aligned with the normal $\hat{\mathbf{n}}$, like in the S_A phase. Up to this point, the structural properties of the various ILC smectic phases, as predicted by the present density functional theory have been discussed. For comparison, in Figs. 3.10, 3.11, and 3.12 the local packing fraction $\eta^{\text{loc}}(\mathbf{r}) = \rho^{\text{loc}}(\mathbf{r}) LR^2\pi/6$ and the local orientational order parameter S_2^{loc} , as obtained by Monte Carlo simulations of an ILC fluid with $L/R = 4$, $\varepsilon_R/\varepsilon_L = 3$, $\lambda_D = 5$, $D/R = 1.8$, $\gamma/(R\varepsilon_0) = 0.045$, and $R_{\text{cut}}/R = 6$, are shown on a simple cubic lattice of sample points within the cubic

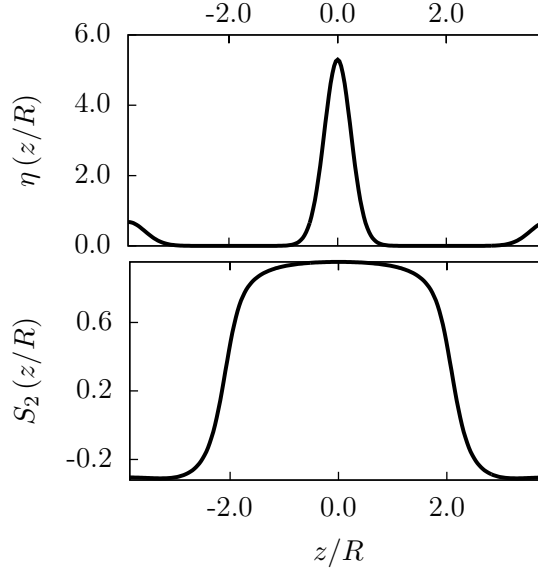


FIGURE 3.9.: Local packing fraction $\eta(z/R)$ and scalar orientational order parameter $S_2(z/R)$ within one period $d/R \approx 7.7$ at the state point $(T^*, \mu^*) = (0.8, 20)$ in Fig. 3.5(b) (magenta dot \bullet) for $L/R = 4$, $\varepsilon_R/\varepsilon_L = 2$, $D/R = 1.8$, $\lambda_D/R = 5$, and $\gamma/(R\varepsilon_0) = 0.045$. One observes an alternating structure with the majority of the particles being located at the center of the layers ($z \approx 0$) with an orientation parallel to the smectic layer normal $\hat{\mathbf{n}} = \hat{\mathbf{z}}$, while a significant minority of particles is located in between the layers (i.e., $|z|/R \approx d/(2R) \approx 3.85$) with preferentially perpendicular orientation (S_{AW} phase).

simulation box of side length $V^{1/3}/R = 13.2$. Figures 3.10 and 3.11 clearly show an ordinary smectic S_A phase, characterized by a periodic structure in which the particles are located inside the smectic layers, indicated by the red data points for large values of $\eta^{\text{loc}}(\mathbf{r})$ and a predominant alignment of particles along the layer normal, indicated by the large positive value of the local orientational order parameter $S_2^{\text{loc}}(\mathbf{r}) \geq 0.5$ for nearly all sample points \mathbf{r} . The data points of Fig. 3.10 are obtained for $(T^*, \mu^*) = (0.5, -1.2)$, i.e., $\eta_0 \approx 0.436$ and the data of Fig. 3.11 corresponds to $(T^*, \mu^*) = (0.6, 1.7)$, i.e., $\eta_0 \approx 0.394$. However, if the temperature is sufficiently low and the chemical potential is chosen such that the mean packing fraction is not too large, e.g., $(T^*, \mu^*) = (0.5, -2.6)$ so that $\eta_0 \approx 0.324$, one observes the novel smectic structure S_{AW} as shown in Fig. 3.12. The alternating orientation of particles gives rise to the alternating pattern of blue ($S_2^{\text{loc}}(\mathbf{r}) < 0$) and red ($S_2^{\text{loc}}(\mathbf{r}) > 0$) data points for the orientational order parameter along the layer normal (Fig. 3.12(b)). For these simulation results the layer normal and

the z -direction are not parallel, because the start configuration is isotropic, which in principle allows the system to form any structure without bias. (Without cost of free energy the sample can be rotated so that the layer normal is parallel to the z axis.) However, the layer normal tends to be parallel to one of the diagonals of the simulation box (compare Figs. 3.10-3.12), which is likely to be related to the cubic geometry of the simulation box and thus appears to be a finite-size effect. In agreement with the present DFT approach, the simulations tell that for the S_A phase the smectic layer spacing is of the size of the particle length $L/R = 4$ while for the S_{AW} phase d is significantly larger. In this phase there are small (local) maxima of the local packing fraction $\eta^{\text{loc}}(\mathbf{r})$ in between the layers (indicated in Fig. 3.12 by the light blue dots being surrounded by dark blue dots). Note that although some sample points in Fig. 3.10 show a negative value of the local orientational order parameter $S_2^{\text{loc}}(\mathbf{r}) < 0$ in between the smectic layers, this does not indicate a realization of the smectic S_{AW} phase, but is due to the well-known observation, that during the simulation some particles move out of the smectic layers and then turn perpendicular, because there is only a narrow gap in between the smectic layers of an ordinary S_A phase (see, e.g., Ref. [98]).

The present DFT predicts that the triple point temperature for an ILC fluid can be increased relative to the corresponding one for an ordinary liquid crystal, provided the location D of the charges, their interaction strength γ , and the screening length λ_D are chosen suitably (compare Figs. 3.4 and 3.5). Therefore the S_{AW} phase can occur for ILCs (see Fig. 3.6(b)) if the S_{AW} - S_A coexistence curve is shifted above the melting transition. In contrast, for ordinary liquid crystals (see Fig. 3.4(a)) the formation of the S_{AW} phase is preempted by crystallization, which is in agreement with the findings of previous studies, e.g., Ref. [86].

It is worth mentioning, that the so-called *intergrowth texture* structure observed in Refs. [92,93] can also be interpreted as an ionic liquid crystal phenomenon, because there hard discs have been considered which interact via an additional, anisotropic Yukawa potential.

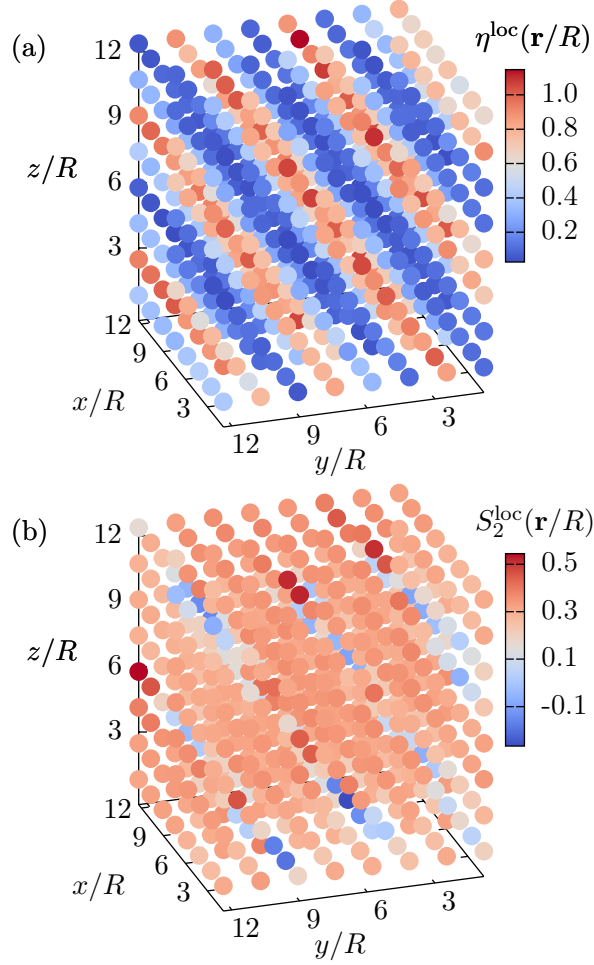


FIGURE 3.10.: Local packing fraction $\eta^{\text{loc}}(\mathbf{r}/R)$ (a) and scalar orientational order parameter $S_2^{\text{loc}}(\mathbf{r}/R)$ (b) obtained from grand canonical Monte Carlo simulations on a periodic cubic box of side length $V^{1/3}/R = 13.2$ at temperature $T^* = 0.5$ and chemical potential $\mu^* = -1.2$, giving rise to a global mean packing fraction $\eta_0 \approx 0.436$ in the simulation box. Each colored dot represents a site of a simple cubic lattice on which $\eta^{\text{loc}}(\mathbf{r}/R)$ and $S_2^{\text{loc}}(\mathbf{r}/R)$, are monitored along the MC trajectory. The color-coding of the dots can be inferred from the respective color key. The parameters of the pair potential are given by $L/R = 4, \varepsilon_R/\varepsilon_L = 3, D/R = 1.8, \lambda_D/R = 5, \gamma/(R\varepsilon_0) = 0.045$, and $R_{\text{cut}}/R = 6$. The ILC molecules are concentrated in the smectic layers which are oriented mainly parallel to the layer normal, which can be inferred from the positive value of $S_2^{\text{loc}}(\mathbf{r}/R) > 0.3$ for positions \mathbf{r} which correspond to large $\eta^{\text{loc}}(\mathbf{r}/R) > 0.6$; this corresponds to an ordinary smectic S_A phase. Some sample points \mathbf{r} yield a negative value of $S_2(\mathbf{r}/R) < 0$, corresponding to particles which eventually moved out of the smectic layers and then turned perpendicular. Here, in contrast to the DFT approach, the layer normal does not necessarily point into the z -direction, but it is tilted towards one of the edges of the simulation box.

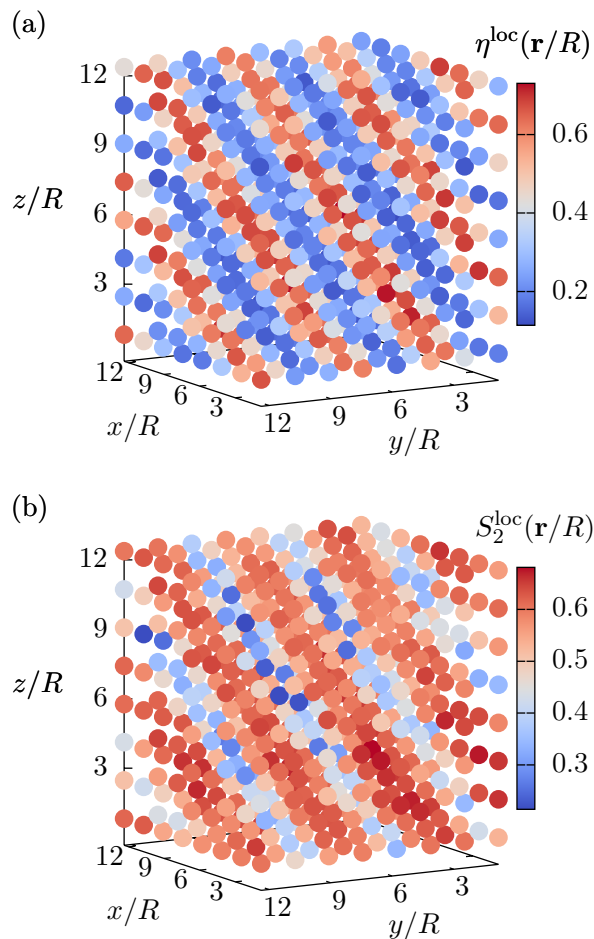


FIGURE 3.11.: Same as Fig. 3.10 but for $T^* = 0.6$ and $\mu^* = 1.7$ which corresponds to $\eta_0 \approx 0.394$. This state point belongs to an ordinary smectic S_A phase, which can be inferred from the positive value of $S_2^{\text{loc}}(\mathbf{r}/R) > 0.4$ for positions \mathbf{r} which correspond to large $\eta^{\text{loc}}(\mathbf{r}/R) > 0.6$. The temperature $T^* = 0.6$ is higher than for the state point $(0.5, -1.2)$ discussed in Fig. 3.10. Here the particles near the centers of the smectic layers are less localized leading to smaller maximum values of the local packing fraction $\eta_{\text{max}}^{\text{loc}}(\mathbf{r}/R) \approx 0.7$ (compare the maxima $\eta_{\text{max}}^{\text{loc}}(\mathbf{r}/R) \approx 1.1$ in Fig. 3.10). The layer normal points towards one of the diagonals of the simulation box.

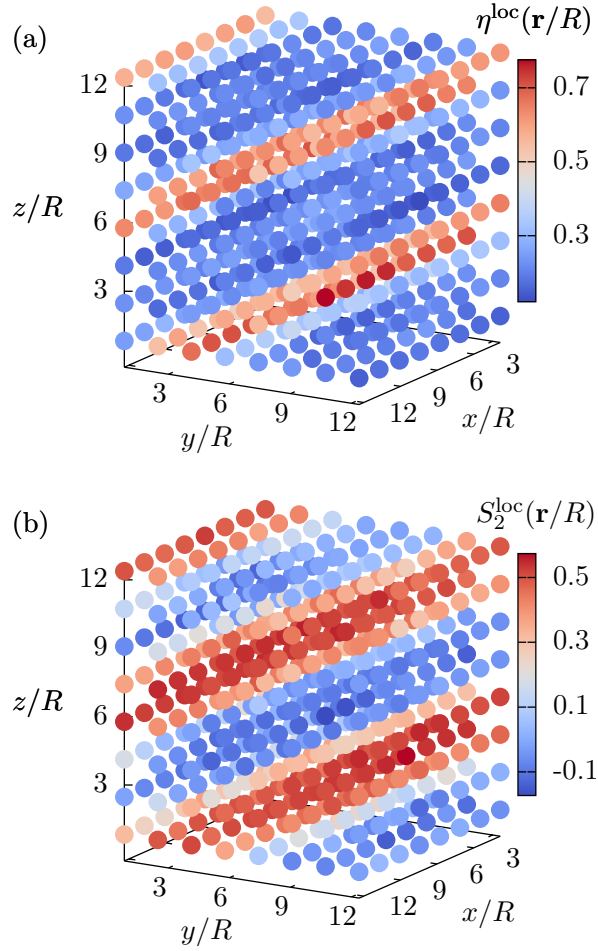


FIGURE 3.12.: Same as Figs. 3.10 and 3.11 but for $T^* = 0.5$ and $\mu^* = -2.6$ which corresponds to $\eta_0 \approx 0.324$. For this state point one observes an alternating structure of a majority of particles, which are strongly localized in the centers of the smectic layers with their orientations parallel to the layer normal, while a minor but considerable amount of the particles is located in between the layers with perpendicular orientation (S_{AW} phase). The layer normal points towards one of the edges of the simulation box.

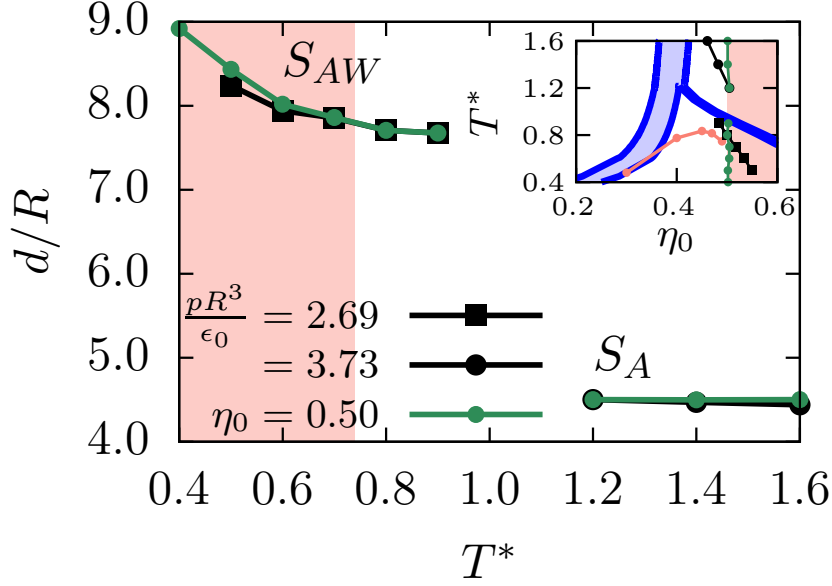


FIGURE 3.13.: Equilibrium layer spacing d/R , as obtained within the present DFT approach, as function of temperature T^* for the parameter set $L/R = 4$, $\varepsilon_R/\varepsilon_L = 2$, $D/R = 1.8$, $\lambda_D/R = 5$, and $\gamma/(R\varepsilon_0) = 0.045$. For $T^* > 1.0$ the ordinary smectic S_A phase is stable (see the inset, which shows the corresponding thermodynamic paths along which the layer spacing d/R has been evaluated). For the considered paths, the layer spacing depends only weakly on temperature. The pressure $p := \Omega[\varrho^{\text{eq}}]/\mathcal{V}$ is obtained by multiplying Eq. (3.8) by kT . For the low-temperature wide smectic S_{AW} phase the dependence on temperature is more pronounced. This is due to the free space in between the layers and the electrostatic repulsion, which becomes more effective upon decreasing temperature. However, this effect is prominent only in that region of the S_{AW} phase where it is metastable with respect to crystallization, i.e., for $T^* \lesssim 0.74$ (salmon-colored area). The pink curve in the inset indicates the onset of crystallization.

3.3.3. Temperature dependence of the layer spacing

The high-temperature phase S_A and the low-temperature phase S_{AW} exhibit distinct structural properties (Figs. 3.8 and 3.9). In particular the size of the layer spacing differs. It turns out that for the S_A phase, in which the layer spacing is about the size of the length L of the particles, the layer thickness varies only weakly as function of temperature (see Fig. 3.13). Along two thermodynamic paths within the domain of the stable S_A phase – one at fixed mean packing fraction $\eta_0 \approx 0.5$ (green dotted vertical path

in the corresponding phase diagram shown in the inset of Fig. 3.13; compare Fig. 3.5(b)) and the other one at fixed pressure $p = -\Omega[\varrho^{\text{eq}}]/\mathcal{V} = 3.73 \varepsilon_0/R^3$ (black dotted path) – the layer spacing does not change much and takes a value of about $d/R \approx 4.4 - 4.5$, which is a common finding for phases of the S_A -type. Interestingly, for both paths (black squared path with $p = 2.69 \varepsilon_0/R^3$ and green dotted path with $\eta_0 \approx 0.5$; $T^* \leq 0.9$) the low-temperature wide smectic phase S_{AW} , which, compared with the S_A phase, exhibits an increased layer spacing (compare Figs. 3.8 and 3.9), also does not show a considerable temperature dependence of the layer spacing within its region of thermodynamic stability (see white background in Fig. 3.13 for $T^* \in [0.74, 0.9]$). However, within the region of the S_{AW} phase being metastable with respect to crystallization, i.e., for $T^* \lesssim 0.74$ in Fig. 3.13 (salmon-colored area), for both paths there is a pronounced temperature dependence of the layer spacing. Since the smectic layers of the S_{AW} phase are not as densely packed as the layers of an ordinary S_A phase, the free space in between the layers allows for a certain softness of the layer spacing. The increase of the layer spacing with decreasing temperature can be understood intuitively, because upon lowering temperature the electrostatic repulsion becomes more efficient so that the smectic layers widen. Nevertheless, since this behavior is only observable within the metastable region of the S_{AW} phase, one expects only a weak temperature dependence of the layer spacing for the S_{AW} phase within its stable region, analogous to the S_A phase.

It is worth mentioning that for the shorter particles with $L/R = 2$, for both the narrow S_{AN} phase as well as for the ordinary S_A phase a very weak dependence of the layer spacing on temperature is observed (analogously to the high-temperature S_A phase in Fig. 3.13).

3.4. Conclusions

In this chapter ILCs have been investigated by means of density functional theory (Secs. 2.2, 3.2.1, and 3.2.3) and grand canonical Monte Carlo simulations (Sec. 3.2.4). To this end a coarse-grained description of the ILC molecules (Fig. 2.1) as rigid ellipsoids interacting via a molecular pair potential $U(\mathbf{r}_{12}, \boldsymbol{\omega}_1, \boldsymbol{\omega}_2)$ (Eq. (2.1) and Fig. 2.2) has been employed (see Sec. 2.1).

The study of the phase behavior demonstrates that ILC fluids show a rich bulk phenomenology. Beyond the qualitative differences in the phase behavior of ordinary and ionic liquid crystals, the dependence of the thermal and structural bulk properties of

ILC fluids on the length-to-breadth ratio of the molecules as well as on the molecular charge distribution has been examined in detail. This analysis leads to the following conclusions:

- (1) Comparing ordinary (uncharged) liquid crystals and ILCs, within the present DFT approach a lowering of the liquid-vapor critical point of the latter is observed (see Fig. 3.2). Additionally, for ILCs the liquid-smectic two-phase region becomes narrower, giving rise to a stable smectic structure at smaller packing fractions η_0 (see Fig. 3.4).
- (2) For the shorter particles with length-to-breadth ratio $L/R = 2$ there is an ordinary S_A phase stable at high temperatures and large mean packing fractions. At low temperatures and intermediate mean packing fractions a distinct smectic S_{AN} structure is observed in which the particles are oriented parallel to the smectic layers, i.e., perpendicular to the layer normal $\hat{\mathbf{n}}$ (see Fig. 3.7), and thus do not show a preferred orientation. (Figure 3.3 provides a comparison of the structure of both types of smectic phases, S_{AN} and S_A , for particles with length-to-breadth ratio $L/R = 2$.) This behavior seems to be related to the small length-to-breadth ratio $L/R = 2$ and to the small value of the anisotropy parameter $\varepsilon_R/\varepsilon_L = 2$ of the underlying Gay-Berne pair potential. This renders the particles rather isotropic, which is even more pronounced in the case of the ILC fluid (Fig. 3.2(b)) due to the additional electrostatic repulsion, and thus leads to a higher L - S_{AN} - S_A triple point temperature. However, considering the large packing fractions $\eta_0 \geq 0.5$ for which the liquid-crystalline phases are predicted to occur in these systems, for a hexagonal lattice structure this leads to a lateral lattice spacing of $a/R \leq 1.1$ (see Secs. 3.2.3 and 3.3.1). Hence, the particles are densely packed in this density regime and previous simulations [85] on systems of Gay-Berne particles of length-to-breadth ratio $L/R = 3$ report the onset of crystallization within that regime. On this basis, at least in parts, the thermodynamic stability of the liquid-crystalline phases S_A and S_{AN} can be expected to be an artifact of the method employed (see Secs. 2.2 and 3.2.1), which cannot capture crystalline phases. The prediction of the liquid-crystalline phases S_A and S_{AN} , which show an periodically varying density profile in z -direction, can be considered as a hint on the presence of various types of crystalline phases at large densities in these systems. The S_A phase can be interpreted as an analogue to a crystalline phase with additional orientational ordering, while the S_{AN} phase mimics a crystalline phase with a lower degree of

orientational ordering (i.e., plastic crystals).

- (3) For the longer particles of length-to-breadth ratio $L/R = 4$, besides the isotropic liquid (L) and the ordinary smectic S_A phase (Fig. 3.8), at low temperatures and sufficiently large packing fractions the novel S_{AW} phase (Fig. 3.9) occurs (see Figs. 3.4 and 3.5). It is characterized by a considerably larger layer spacing than in the ordinary S_A phase (compare Figs. 3.8 and 3.9). While the majority of particles is oriented mostly parallel to the layer normal, as indicated by a large value of the orientational order parameter $S_2(z = 0) > 0.8$ within the smectic layers, a significant number of particles is located in between the smectic layers. Those particles tend to be perpendicular to the layer normal, giving rise to $S_2(|z| \lesssim d/2) < 0$.
- (4) Concerning the phase behavior of ILCs as function of the location of the charges in the molecules, for the parameter set $L/R = 4$, $\lambda_D/R = 5$, $\varepsilon_R/\varepsilon_L = 2$, $\gamma/(R\varepsilon_0) = 0.045$ positioning the charges at an intermediate distance $D/R \leq 0.9$ from the geometric center does not alter the phase behavior much as compared to positioning the charges in the center (see Figs. 3.4(b) and 3.5(a)). However if the charges are located almost at the tips of the molecules ($L/R = 4$, $D/R = 1.8$, Fig. 3.5(b)) there is a significant change in the phase behavior. The coexistence of the phases S_{AW} and S_A is shifted towards higher temperatures. This shift for $D/R = 1.8$ stabilizes the S_{AW} phase in a temperature regime below the ordinary S_A phase but above the melting curve, unlike the other cases studied (Figs. 3.4 and 3.5(b)) for which our analysis, using the method discussed in Sec. 3.2.3, yields that the S_{AW} phase is expected to be preempted by crystallization (compare the pink curves in Figs. 3.4 and 3.5 which are obtained by the procedure outlined in Fig. 3.1). Accordingly, the S_{AW} phase is observed, within the present Monte Carlo simulations, for an ILC fluid the charges of which are located at the tips of the molecules. In qualitative agreement with DFT, the simulations yield an ordinary smectic S_A phase at high temperatures and large packing fractions (see Figs. 3.10 and 3.11); the layer spacing is of the size of the particles and nearly all of them are located within the smectic layers aligned with the layer normal (see Fig. 3.6(a)). At lower temperatures the novel S_{AW} smectic phase with wide layer spacings occurs, such that a considerable fraction of particles is located in between the smectic layers with mainly perpendicular orientation with respect to the layer normal (see Figs. 3.6(b) and 3.12).

- (5) Analyzing the dependence of the smectic layer spacing on temperature for the parameter set $L/R = 4, \varepsilon_R/\varepsilon_L = 2, \lambda_D/R = 5, D/R = 1.8, \gamma/(R\varepsilon_0) = 0.045$ reveals distinct behaviors of the smectic S_A and S_{AW} phases (see Fig. 3.13): While the layer spacing of the ordinary high-temperature smectic S_A phase does not vary notably as function of temperature, which is a common finding for ordinary S_A phases, increasing layer spacings for decreasing temperatures can be observed for the low-temperature smectic phase S_{AW} . This can be understood in terms of the free space in between the smectic layers which gives rise to a certain softness in the layer spacing. Due to the enhanced effective electrostatic repulsion at lower temperatures, the layers tend to widen upon lowering the temperature. However, this behavior is prominent only in the metastable region of the S_{AW} phase, while within the stable region of the S_{AW} phase, in analogy to the high-temperature S_A phase, there is no pronounced temperature dependence of the layer spacing.

Like the high-temperature S_A phase for long particles (see Fig. 3.13), the layer spacing of the smectic S_A and S_{AN} phases, observed for shorter particles with $L/R = 2$, does not exhibit a considerable temperature dependence.

Finally, it is important to mention, that the particular choice of the projected density distribution $\bar{\rho}(\mathbf{r}, \boldsymbol{\omega})$ (Eq. 2.12) with respect to our theoretical approach, is crucial, because the incorporation of second-order Fourier modes is indispensable for capturing the novel wide smectic S_{AW} phase.

A more realistic model description could be obtained by determining the Debye screening length λ_D in accordance with Eq. (2.6), instead of treating it as a control parameter with a fixed value $\lambda_D/R = 5$. Within this approach, the full range of the Debye screening length in the various density and temperature regimes could be incorporated into the model, which could lead to interesting new phase behaviors and structural phenomena. While for dilute electrolyte solutions one typically finds $\lambda_D/R \gg 1$, in dense ionic liquids the Debye screening length λ_D can become smaller than the particle diameter R . Thus, the value $\lambda_D/R = 5$ used throughout this study lays in between those two limiting cases.

The description of the reference hard-core system within an approach more sophisticated than Eq. (3.13), such as fundamental measure theory, would allow for a more reliable calculation of the transition towards crystalline phases. This can be considered as a necessary step in order to accurately predict the extent of S_{AW} stability at low temperatures.

FREE INTERFACES IN ILCs

Free interfaces between coexisting bulk phases of ionic liquid crystals are studied. In particular, the structure and orientational order at the interface of an isotropic liquid and two distinct types of smectic-A phases are analyzed in terms of the density distribution and the orientational order parameter.

4.1. Introduction

In the previous chapter the bulk phase behavior of ILCs has been discussed. Particular attention was drawn to the dependence of the (macroscopically observable) phase behavior on intrinsic (microscopic) molecular properties, such as the aspect-ratio or the charge distribution of the constituent molecules. Interestingly, a new smectic-A phase (S_{AW}) could be observed, the structure of which is built of alternating layers. In between layers of particles, which prefer to be parallel to the layer normal (analogously to the ordinary S_A phase), one observes secondary layers in which the particles prefer orientations perpendicular to the layer normal. In fact, the alternating structure of parallel and perpendicular orientations within the layers of the S_{AW} phase is stabilized by charges that are located at the tips of the ILC molecules and it shows in an exemplary way how the combination of liquid-crystalline and electrostatic properties in systems of ionic liquid crystals can lead to interesting novel bulk phenomena.

The goal of the present chapter is to go one step further, that is, studying inhomogeneous ILC systems. Investigating how the structures and orientational properties of the bulk phases are altered by the presence of an interface can lead to more insights on the microscopic mechanisms acting in the considered system. For instance, the variations of the density distribution and of the orientational order parameter at the interface can reveal the relevant molecular length scales, present in the system. Thereby, these length scales might be attributed to particular energetic contributions of the underlying pair interactions. Moreover, the analysis of the ILC phase behavior in Chapter 3 yielded, that both of the observed smectic phases, S_A and S_{AW} , can be in coexistence with the isotropic liquid L . This is interesting, because this allows to investigate interfaces characterized by a transition towards a structured and orientationally ordered (smectic) phase from an isotropic (homogeneous) fluid. On one hand, this type of a liquid-crystalline interface has not been studied intensively in the literature (e.g., Refs. [101–103]) so far and on the other hand the transition in both the structure and orientational order allows to study the interplay of both properties while they built up at the interface. Another interesting question addresses the equilibrium tilt angle between the interface normal and the smectic layer normal, because it may give insights to nucleation and growth phenomena which are affected by the dependence of the interfacial tension on the orientation of the considered structure [104, 105].

In order to study the above mentioned types of interfaces, first, in Sec. 4.2.1, the present DFT approach (see Sec. 2.2) is adopted to the study of interfacial systems

and the relevant thermodynamic quantities and observables, such as the Gibbs dividing surface (Sec. 4.2.2) and the interfacial tension (Sec. 4.2.3) are introduced. Subsequently, the results for free interfaces between the isotropic liquid L and the considered smectic-A phases S_A or S_{AW} are discussed in Sec. 4.3. Finally, in Sec. 4.4, conclusions based on these findings are drawn.

4.2. Methods

4.2.1. Free interfaces within the present DFT framework

The present chapter is devoted to the analysis of interfaces which are formed between coexisting bulk phases. In particular, planar interfaces between the isotropic liquid L and the two different types of smectic-A phases (S_A or S_{AW} , see Sec. 3.3.1, in particular Fig. 3.6) will be considered. Without loss of generality, the interface normal is set to be parallel to the z -axis (see Fig. 4.1). Due to the isotropy of the liquid phase L , the direction of the smectic layer normal

$$\hat{\mathbf{n}}(\alpha) := \sin(\alpha) \hat{\mathbf{x}} + \cos(\alpha) \hat{\mathbf{z}} \quad (4.1)$$

can be chosen to lay in the x - z -plane. Its orientation is fully determined by the tilt angle α . For $\alpha = 0$ the smectic layer normal $\hat{\mathbf{n}} = \hat{\mathbf{z}}$ points into the z -direction, like the interface normal, while for $\alpha = \pi/2$ it points into the x -direction and thus it is perpendicular to the interface normal. The interfacial systems considered here are translationally invariant in the y -direction and show a periodic structure in the x -direction with a periodicity $d_x = d/\sin(\alpha)$ (compare Fig. 4.1) where d is a multiple of the bulk smectic layer spacing. (Recall that the value of d is determined by the corresponding bulk density profile which minimizes the grand potential functional, i.e., maximizes the bulk pressure (see Eq. 3.9 in Sec. 3.2.2). It turns out that, for the S_{AW} phase the periodicity d equals the smectic layer spacing. However, for the S_A phase d equals two times the layer spacing, because for the S_A phase one obtains bulk solutions $\varrho^{(0)}(\mathbf{r}, \boldsymbol{\omega})$ with $Q_1 = Q_4 = 0$, (see, cf., Eqs. (2.12), (4.2), and (4.3)). Thus the periodicity d along the layer normal $\hat{\mathbf{n}}$ is two times the smectic layer spacing, i.e., the distance between neighboring layers.) For $\alpha = 0$, d_x diverges and the system exhibits translational invariance in the x -direction as well. In Sec. 2.2, the coefficients $Q_i(\mathbf{r})$ in Eq. (2.12) were introduced by expanding the density distribution $\varrho(\mathbf{r}, \boldsymbol{\omega})$ in a second-order Legendre and Fourier-series, leading to the

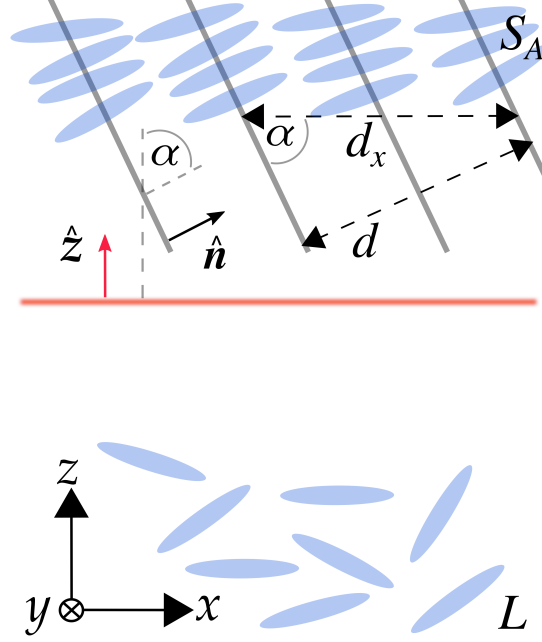


FIGURE 4.1.: Sketch of the interfaces under consideration. Consider a planar interface, illustrated by the horizontal red line, between the isotropic bulk liquid L , imposed as the boundary condition at $z \rightarrow -\infty$, and the smectic-A phase S_A (or S_{AW}); imposed as the boundary condition at $z \rightarrow +\infty$. Thus, the interface normal (red vertical arrow) points into the z -direction. At the top, the tails of four layers of particles of the (ordinary) smectic phase S_A are visible, which are well aligned with the layer normal $\hat{\mathbf{n}} := \sin(\alpha)\hat{\mathbf{x}} + \cos(\alpha)\hat{\mathbf{z}}$. In the bulk S_A phase, the system is periodic in the direction of the smectic layer normal $\hat{\mathbf{n}}$ with periodicity d which is a multiple of the smectic layer spacing (see Sec. 4.2.1 below Eq. (4.1)). Thus, for a given tilt angle α between the interface normal and the smectic layer normal $\hat{\mathbf{n}}$, the system is periodic in x -direction with periodicity $d_x = d/\sin(\alpha)$. Note that the interface system is translationally invariant in the y -direction for all angles $0 \leq \alpha \leq \pi/2$. For $\alpha = 0$ the system is translationally invariant in the x -direction, too.

projected density $\bar{\varrho}(\mathbf{r}, \boldsymbol{\omega}, [\varrho])$ (Eq. (2.12)):

$$Q_i(\mathbf{r}, [\varrho]) = \frac{1}{\mathcal{V}_d} \int_{\mathcal{V}} d^3r' \int_{\mathcal{S}} d^2\omega' \varrho(\mathbf{r}', \boldsymbol{\omega}') w_i(\mathbf{r}, \mathbf{r}', \boldsymbol{\omega}') \quad (4.2)$$

with

$$\begin{aligned}
w_0 &= \mathcal{T}(\mathbf{r} - \mathbf{r}'), \\
w_1 &= 2\mathcal{T}(\mathbf{r} - \mathbf{r}') \cos(2\pi(\mathbf{r}' \cdot \hat{\mathbf{n}})/d), \\
w_2 &= 2\mathcal{T}(\mathbf{r} - \mathbf{r}') \cos(4\pi(\mathbf{r}' \cdot \hat{\mathbf{n}})/d), \\
w_3 &= \mathcal{T}(\mathbf{r} - \mathbf{r}') P_2(\boldsymbol{\omega}' \cdot \hat{\mathbf{n}}), \\
w_4 &= 2\mathcal{T}(\mathbf{r} - \mathbf{r}') P_2(\boldsymbol{\omega}' \cdot \hat{\mathbf{n}}) \cos(2\pi(\mathbf{r}' \cdot \hat{\mathbf{n}})/d), \\
w_5 &= 2\mathcal{T}(\mathbf{r} - \mathbf{r}') P_2(\boldsymbol{\omega}' \cdot \hat{\mathbf{n}}) \cos(4\pi(\mathbf{r}' \cdot \hat{\mathbf{n}})/d),
\end{aligned} \tag{4.3}$$

where

$$\mathcal{T}(\mathbf{r} - \mathbf{r}') = \begin{cases} 1, & \mathbf{r} - \mathbf{r}' \in \mathcal{V}_d \\ 0, & \text{else.} \end{cases} \tag{4.4}$$

$\mathcal{T}(\mathbf{r} - \mathbf{r}')$ is a cut-off function which defines the integration domain $\mathcal{V}_d := \int_{\mathcal{V}} d^3r' \mathcal{T}(\mathbf{r} - \mathbf{r}')$ around position \mathbf{r} . For $0 < \alpha \leq \pi/2$ the considered interfaces between the isotropic liquid L and the smectic-A phases S_A or S_{AW} exhibit periodic structures in the x -direction with periodicity $d_x = d/\sin(\alpha)$. Here, \mathcal{V}_d is a slice of length d_x in x -direction with a vanishing extension in z -direction centered at position \mathbf{r} , i.e., $\mathcal{T}(\mathbf{r} - \mathbf{r}') = \Theta(d_x/2 - |x - x'|) \delta(z - z')$ where $\Theta(x)$ and $\delta(x)$ are the Heaviside step function and the Dirac delta function, respectively. The index d of the integration domain \mathcal{V}_d indicates that \mathcal{V}_d corresponds to a region which is specified by the periodicity d . Due to the translational invariance in y -direction the extension of the integration domain \mathcal{V}_d can be chosen arbitrarily in the y -direction. Due to the periodicity of $\varrho(\mathbf{r}, \boldsymbol{\omega})$ in the x -direction, this choice of the integration domain \mathcal{V}_d leads to coefficients $Q_i(z)$ (Eq. (4.2)) which depend only on z , i.e., on the coordinate parallel to the interface normal.

For $0 < \alpha \leq \pi/2$ one could also consider an integration domain which has a non-vanishing extent in z -direction. However, such a choice has at least two disadvantages: First, unlike d_x , which corresponds to the periodicity of the interfacial system in x -direction, for $0 < \alpha \leq \pi/2$ there is no obvious choice parallel to the interface normal. Moreover, there is no unique choice for the geometrical shape of the integration domains. Besides using a (simple) rectangular form, one could also use any other (two-dimensional) geometrical object as integration domain \mathcal{V}_d . In this sense the slice of length d_x perpendicular to the interface normal is a simple but consistent choice. Second, this choice renders the evaluation numerically less demanding, because it requires only a one-dimensional integration (exploiting the translational invariance in y -direction), instead

of evaluating a two-dimensional integral. Note, that an infinite extent of the integration domain parallel to the interface normal leads to coefficients Q_i which are independent of the position \mathbf{r} and therefore cannot be used to obtain interface profiles.

If $\alpha = 0$, i.e., the smectic layer normal $\hat{\mathbf{n}} = \hat{\mathbf{z}}$ is parallel to the interface normal, d_x diverges and the system is translationally invariant in x - and y -direction. In this case, the integration domain \mathcal{V}_d has an extent of length d in z -direction, i.e., $\mathcal{T}(\mathbf{r} - \mathbf{r}') = \Theta(d/2 - |z - z'|)$ and with arbitrary extent in the lateral dimensions x and y . As before, the coefficients $Q_i(z)$ depend only on the z -coordinate. It is worth mentioning, that for all tilt angles $0 \leq \alpha \leq \pi/2$ the correct (constant) bulk values of the coefficients Q_i are recovered, although for $0 < \alpha < \pi/2$ the orientation of the integration domain \mathcal{V}_d (recall that \mathcal{V}_d is a slice of width d_x in x -direction for all $\alpha \in (0, \pi/2]$) changes with respect to the direction of the smectic layer normal $\hat{\mathbf{n}}(\alpha)$. However, because the integration domain covers a full period d_x in x -direction, it gives the same values for the coefficients Q_i in the bulk phases, as for evaluating the coefficients Q_i with an integration domain parallel to the smectic layer normal $\hat{\mathbf{n}}$, which is the case for $\alpha = 0$ and $\pi/2$.

It is worth mentioning that odd Fourier-modes in the projected density $\bar{\varrho}(\mathbf{r}, \boldsymbol{\omega})$ vanish for the relevant bulk phases, in particular for smectic-A phases. If the coordinate system is chosen such that the origin is located at the center of one of the smectic layers due to the mirror symmetry of the smectic layers around their center. This is a direct consequence of the underlying point symmetry of the particles considered here (see Fig. 2.1). Considering additional terms, corresponding to the odd modes in the Fourier expansion of the density distribution $\varrho(\mathbf{r}, \boldsymbol{\omega})$, would only give rise to a shift of the location of the bulk smectic layers. However, for interfacial systems the odd modes in general do not vanish. Nevertheless, here, these contributions are neglected completely. The implications of additionally considering these odd terms (up to second order) are discussed in Appendix D. No qualitative differences could be observed for the cases which have been investigated. Note, that both approaches (considering or neglecting the odd terms) are weighted-density-like approximations of the exact free energy functional. A priori, it is not obvious which one leads to better results, because considering more terms of the Fourier series leads only to a more accurate representation of $\varrho(\mathbf{r}, \boldsymbol{\omega})$ via the projected density $\bar{\varrho}(\mathbf{r}, \boldsymbol{\omega})$. However, this does not imply that the resulting free energy functional $\beta\mathcal{F}[\bar{\varrho}]$ is closer to its exact form, because independent of the choice for $\bar{\varrho}(\mathbf{r}, \boldsymbol{\omega})$ the present free energy functional relies on the Parsons-Lee approach for its reference part and on the so-called modified mean-field approximation for the excess part (see Sec. 2.2). Nonetheless, considering in Eq. (2.12) only the even modes up to second order captures the three

types of bulk phases L , N , as well as S_A , S_{AW} , which are relevant for the present study in the same way as the full second-order Fourier expansion.

In order to evaluate the Euler-Lagrange equation (Eq. (2.8)), the one-particle direct correlation function has to be known. Analogously to the (modified) one-particle direct correlation function $\tilde{c}^{(1)}(\mathbf{r}, \boldsymbol{\omega}, [\varrho])$ (Eq. (3.3)), used for the analysis of the bulk phase behavior, the corresponding one-particle direct correlation function valid for interfacial systems can be written as:

$$\begin{aligned} c^{(1)}(\mathbf{r}, \boldsymbol{\omega}, [\varrho]) = & -\beta\psi(\mathbf{r}, \boldsymbol{\omega}, [\bar{\varrho}]) + \\ & \frac{1}{2\mathcal{V}_d} \int_{\mathcal{V}} d^3r' \int_S d^2\omega' \bar{\varrho}(\mathbf{r}', \boldsymbol{\omega}') \partial_{Q_0} \mathcal{J}(Q_0(\mathbf{r}')) \mathcal{T}(\mathbf{r} - \mathbf{r}') \times \\ & \int_{\mathcal{V}} d^3r'' \int_S d^2\omega'' \bar{\varrho}(\mathbf{r}'', \boldsymbol{\omega}'') f_M(\mathbf{r}' - \mathbf{r}'', \boldsymbol{\omega}', \boldsymbol{\omega}''). \end{aligned} \quad (4.5)$$

Importantly, here, the coefficients $Q_i(\mathbf{r})$ are functions of the position \mathbf{r} (unlike the bulk case, in which they are constants) and they are provided by Eq. (4.2). Note that in Eq. (4.5) $\frac{\delta Q_0(\mathbf{r}')}{\delta \bar{\varrho}(\mathbf{r}, \boldsymbol{\omega})}$ has been replaced by $\frac{\delta Q_0(\mathbf{r}')}{\delta \varrho(\mathbf{r}, \boldsymbol{\omega})} = \frac{\mathcal{T}(\mathbf{r} - \mathbf{r}')}{\mathcal{V}_d}$, which is exact only for bulk phases. However, the functional derivative $\frac{\delta Q_0(\mathbf{r}')}{\delta \bar{\varrho}(\mathbf{r}, \boldsymbol{\omega})} = \int_{\mathcal{V}} d^3r'' \int_S d^2\omega'' \frac{\delta Q_0(\mathbf{r}')}{\delta \varrho(\mathbf{r}'', \boldsymbol{\omega}'')} \frac{\delta \varrho(\mathbf{r}'', \boldsymbol{\omega}'')}{\delta \bar{\varrho}(\mathbf{r}, \boldsymbol{\omega})}$ cannot be calculated analytically in general. The evaluation of $\frac{\delta \varrho(\mathbf{r}'', \boldsymbol{\omega}'')}{\delta \bar{\varrho}(\mathbf{r}, \boldsymbol{\omega})}$ requires the functional derivative of the Euler-Lagrange equation, i.e., Eq. (2.8), which would again produce terms containing $\frac{\delta Q_0(\mathbf{r}')}{\delta \bar{\varrho}(\mathbf{r}, \boldsymbol{\omega})}$. Nevertheless, recall that the derivation of Eq. (4.5) incorporates a modification of the exact one-particle direct correlation such that the density profile $\varrho(\mathbf{r}, \boldsymbol{\omega})$ is replaced by the projected density $\bar{\varrho}(\mathbf{r}, \boldsymbol{\omega})$. In this respect, replacing $\frac{\delta Q_0(\mathbf{r}')}{\delta \bar{\varrho}(\mathbf{r}, \boldsymbol{\omega})}$ by $\frac{\delta Q_0(\mathbf{r}')}{\delta \varrho(\mathbf{r}, \boldsymbol{\omega})} = \frac{\mathcal{T}(\mathbf{r} - \mathbf{r}')}{\mathcal{V}_d}$ is consistent with the underlying assumptions. Moreover, it leads to the correct bulk limit of the interface profile $\varrho(\mathbf{r}, \boldsymbol{\omega})$ at the boundaries, i.e., $z \rightarrow \pm\infty$.

For obtaining the interfacial profiles, Eq. (2.8) has been solved numerically (utilizing a Picard scheme with retardation [70]) by using Eq. (4.5) as well as the (constant) bulk values of the coefficients $Q_{i,L} = Q_i(z \rightarrow -\infty)$ in the isotropic liquid phase L and $Q_{i,S} = Q_i(z \rightarrow \infty)$ in the smectic-A phase (S_A or S_{AW}) at coexistence $(T, \mu) = (T_{\text{coex}}, \mu_{\text{coex}})$. Like in the previous chapter, the structural properties and the orientational order are analyzed in terms of the interface profiles of the packing fraction $\eta(\mathbf{r}) = \frac{\pi}{6} LR^2 n(\mathbf{r})$ with the number density $n(\mathbf{r}) := \int_S d^2\omega \varrho(\mathbf{r}, \boldsymbol{\omega})$ (Eq. (2.19)), and in terms of the orientational order parameter $S_2(\mathbf{r}) := \int_S d^2\omega f(\mathbf{r}, \boldsymbol{\omega}) P_2(\boldsymbol{\omega} \cdot \hat{\mathbf{n}})$ (Eq. (2.20)). Recall, that $f(\mathbf{r}, \boldsymbol{\omega}) := \varrho(\mathbf{r}, \boldsymbol{\omega})/n(\mathbf{r})$ describes the orientational distribution.

4.2.2. Gibbs dividing surface

The position z_η of the interface is determined by the density distribution $\rho(\mathbf{r}, \boldsymbol{\omega})$ for which the notion of the *Gibbs dividing surface* is utilized [5]:

$$h_\eta(z_\eta) := \int_{-\infty}^{z_\eta} dz' (\eta_0(\mathbf{r}') - \eta_{0,L}) + \int_{z_\eta}^{\infty} dz' (\eta_0(\mathbf{r}') - \eta_{0,S_A}) = 0, \quad (4.6)$$

where $\eta_0(\mathbf{r}) = Q_0(\mathbf{r}) LR^2\pi/6$ is the mean packing fraction at position \mathbf{r} . The quantities $\eta_{0,L} = \eta(z \rightarrow -\infty)$ and $\eta_{0,S_A} = \eta(z \rightarrow \infty)$ are the bulk values of $\eta_0(\mathbf{r})$ in the isotropic liquid phase L and the smectic-A phase S_A (or S_{AW}), respectively. The interface position z_η in Eq. (4.6) corresponds to the location of a step-like profile such that the number of particles in excess and in deficit of the bulk values is the same on both sides of the interface. Taking the derivative of the left-hand side $h_\eta(z)$ of Eq. (4.6) with respect to z leads to $h'_\eta(z = z_\eta) := \eta_{0,S_A} - \eta_{0,L}$ which is a constant. Therefore $h_\eta(z) = (\eta_{0,S_A} - \eta_{0,L})z + h_\eta(0)$ is a linear function and one has to evaluate $h_\eta(0)$ only once in order to obtain

$$z_\eta = -h_\eta(0)/(\eta_{0,S_A} - \eta_{0,L}), \quad (4.7)$$

using Eq. (4.6), i.e., $h_\eta(z_\eta) = 0$. While z_η can be interpreted as the location of the *transition in the structure* from the isotropic liquid L to the smectic-A phase S_A (or S_{AW}), replacing η by S_2 in Eq. (4.6) defines a position

$$z_{S_2} = -h_{S_2}(0)/(S_{20,S_A} - S_{20,L}), \quad (4.8)$$

which corresponds to the *transition in the orientational order* from one phase to the other.

Note, that instead of using the mean packing fraction η_0 or the mean orientational order parameter S_{20} in Eq. (4.6), for determining the interface positions in principle, one could also use the profiles $\eta(\mathbf{r})$ and $S_2(\mathbf{r})$ directly. However, the disadvantage of this latter approach is that in the smectic-A bulk phase S_A (or S_{AW}) the profiles $\eta(\mathbf{r})$ and $S_2(\mathbf{r})$ are still functions of the position \mathbf{r} (via the projection $\mathbf{r} \cdot \hat{\mathbf{n}}$ onto the layer normal $\hat{\mathbf{n}}$). Typically, this prevents the use of the latter generalized Eqs. (4.7) and (4.8) for determining z_η and z_{S_2} . Instead, one has to solve Eq. (4.6) numerically, which requires many iterations depending on the desired accuracy.

Nevertheless, in the particular case $\alpha = \pi/2$ the interface normal and the smectic layer normal are perpendicular. Due to the translational invariance of the smectic phases per-

pendicular to their layer normal, here the density profile $\eta(z \rightarrow \infty)$ and the orientational order parameter profile $S_2(z \rightarrow \infty)$ do not depend on z for $z \rightarrow \infty$ in the smectic bulk, but they depend only on the x -coordinate. Thus, for $\alpha = \pi/2$ one can define interface contours $\tilde{z}_\eta(x)$ and $\tilde{z}_{S_2}(x)$, analogously to z_η and z_{S_2} :

$$\begin{aligned} \tilde{h}_m(\tilde{z}_m(x)) &:= \int_{-\infty}^{\tilde{z}_m(x)} dz' (m(\mathbf{r}') - m_L) + \\ &\quad \int_{z_m(x)}^{\infty} dz' (m(\mathbf{r}') - m_{S_A}) = 0, \\ \tilde{z}_m(x) &= -\tilde{h}_m(0)/(m_{S_A}(x) - m_L), \end{aligned} \quad (4.9)$$

where $m \in \{\eta, S_2\}$.

4.2.3. Interfacial tension

The interfacial tension Γ is a measure of the excess amount of work needed to form an interface between coexisting bulk phases [5]. Accordingly, it can be calculated by determining the increase in the grand potential $\beta\Omega[\rho]$ of the interfacial system in excess of the bulk grand potential $\beta\Omega_0 := -\beta p\mathcal{V}$ which is given by the bulk pressure p (Eq. (3.8)) times the system volume \mathcal{V} :

$$\Gamma^*(\alpha) := \beta\Gamma(\alpha) = \frac{\beta\Omega([\rho], \alpha) + \beta p_{\text{coex}}\mathcal{V}}{A}, \quad (4.10)$$

where A is the cross-sectional area of the system in lateral directions to the interface normal. Hence, $\Gamma^*(\alpha)$ has the dimension 1/area. The pressure $p_{\text{coex}} := p(T_{\text{coex}}, \mu_{\text{coex}}, d)$ at coexistence $(T, \mu) = (T_{\text{coex}}, \mu_{\text{coex}})$ is the same in the isotropic liquid L and the smectic-A phase S_A or S_{AW} with the equilibrium layer spacing d . The equilibrium tilt angle α_{eq} minimizes the interfacial tension $\Gamma^*(\alpha = \alpha_{\text{eq}})$ (see Sec. 4.3.4).

4.3. Results

In this section the present results for interfaces formed between the isotropic liquid L and the smectic-A phase S_A or S_{AW} are discussed. The analysis focuses on two particular kinds of ionic liquid crystals (ILCs): First, ILCs with charges in the center, i.e., $D = 0$ (see Figs. 2.1 and 2.2, as well as Eq. (2.5)), and second, ILCs with charges at the tips, i.e., $D/R = 1.8$. The structural and orientational properties of the interfaces are discussed

in terms of the packing fraction $\eta(\mathbf{r})$ and the orientational order parameter $S_2(\mathbf{r})$ for various relative orientations between the interface normal and the smectic layer normal, i.e., for different tilt angles α (see Fig. 4.1). All results presented in this chapter are obtained via the density functional approach described in Secs. 2.2 and 4.2.1.

4.3.1. Interface normal parallel to the smectic layer normal

$$(\alpha = 0)$$

First, consider the case that the interface normal is parallel to the smectic layer normal, i.e., $\alpha = 0$ and $\hat{\mathbf{n}} = \hat{\mathbf{z}}$ (see Eq. (4.1) and Fig. 4.1). Due to translational invariance in the x - and y -directions, the packing fraction $\eta(z)$ and the orientational order parameter $S_2(z)$ are functions solely of the spatial coordinate z . Recall that for the case of an ILC with $L/R = 4$, $\varepsilon_R/\varepsilon_L = 2$, $\gamma/(R\varepsilon_0) = 0.045$, $\lambda_D/R = 5$, and $D = 0$, i.e., the charges are localized in the center of the molecule. The corresponding bulk phase behavior is shown in the phase diagram of Fig. 3.5(a). Within the temperature range $T^* \in [0.9, 1.65]$ solely a first-order phase transition from the isotropic liquid phase L to the ordinary smectic-A phase S_A occurs. (Recall, that for temperatures $T^* < 0.9$ crystallization sets in, thus no considerable stable thermodynamic region of the S_{AW} phase is expected for $D = 0$ (see the discussion in Sec. 3.3.1).) The S_A phase is characterized by a layer structure with a smectic layer spacing $d/R \approx 4.3$, which is comparable to the particle length $L/R = 4$. The smectic layers are composed of ILC molecules which are well aligned with the smectic layer normal $\hat{\mathbf{n}}$.

The L - S_A interface profiles are shown in Fig. 4.2 for $T^* = 1.3$. In Fig. 3.5(a) the corresponding two coexisting bulk states are marked by orange dots (•). Panels (a) and (b) show the packing fraction profile $\eta(z)$ along the interface normal and the orientational order parameter profile $S_2(x)$, respectively. The black dashed vertical line in panel (a) marks the position z_η of the Gibbs dividing surface, which is defined by Eq. (4.7). Correspondingly, the black dashed vertical line in panel (b) marks the position z_{S_2} (Eq. (4.8)). Apparently, the two interface positions z_η and z_{S_2} , which are related to the interfacial transition in the structure and in the orientational order, respectively, differ from each other. In Fig. 4.3, these differences $(z_\eta - z_{S_2})/R$ are plotted as function of the reduced temperature T^* for three different kinds of (liquid-crystalline) materials. The violet curve corresponds to ILCs with all charges concentrated in the molecular centers, i.e., $D = 0$, while the green curve shows data points for $D/R = 1.8$. The blue curve corresponds to a system of (uncharged) ordinary liquid crystals (OLCs) described by

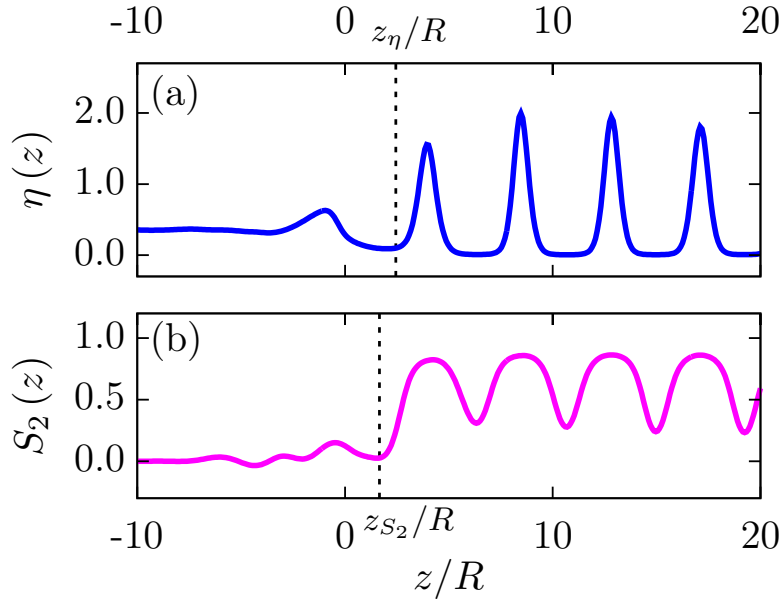


FIGURE 4.2.: The L - S_A interface profile of the packing fraction $\eta(z)$, panel (a), and the orientational order parameter $S_2(z)$, panel (b), are shown for ILCs with $L/R = 4$, $\varepsilon_R/\varepsilon_L = 2$, $\gamma/(R\varepsilon_0) = 0.045$, $\lambda_D/R = 5$, and $D = 0$, i.e., the charges are concentrated in the center of the molecules. The free interface between the isotropic liquid L (imposed as boundary condition for $z \rightarrow -\infty$) and the ordinary smectic-A phase S_A (i.e., $z \rightarrow \infty$) is considered for the reduced temperature $T^* = 1.3$. The coexisting bulk states are marked by the orange dots (\bullet) in the corresponding phase diagram shown in Fig. 3.5(a). The tilt angle is $\alpha = 0$, i.e., the smectic layer normal $\hat{\mathbf{n}} = \hat{\mathbf{z}}$ is parallel to the interface normal (see Eq. (4.1) and Fig. 4.1). For $z/R > 0$ the last layers of the S_A phase are visible, in which the particles are still well aligned with the z -axis, indicated by large values of the orientational order parameter $S_2(z/R) > 0.8$ within these layers. For $z/R < 0$ the layer structure of the density dies out rapidly and the orientational order vanishes as well. Ultimately, the isotropic bulk limit will be approached for $z \rightarrow -\infty$. However, already for $z/R < -10$ the profiles have de facto reached their bulk limits in the isotropic liquid L . The black dashed lines refer to the interface positions z_η and z_{S_2} , respectively, calculated via Eqs. (4.7) and (4.8). The difference $(z_\eta - z_{S_2})/R \approx 2.45 - 1.66 = 0.79$ between the two interface positions is considerably smaller than the smectic layer spacing $d/R \approx 4.28 \gtrsim L/R = 4$. Therefore the orientational order of the S_A phase vanishes within the last smectic layer while approaching the isotropic liquid L .

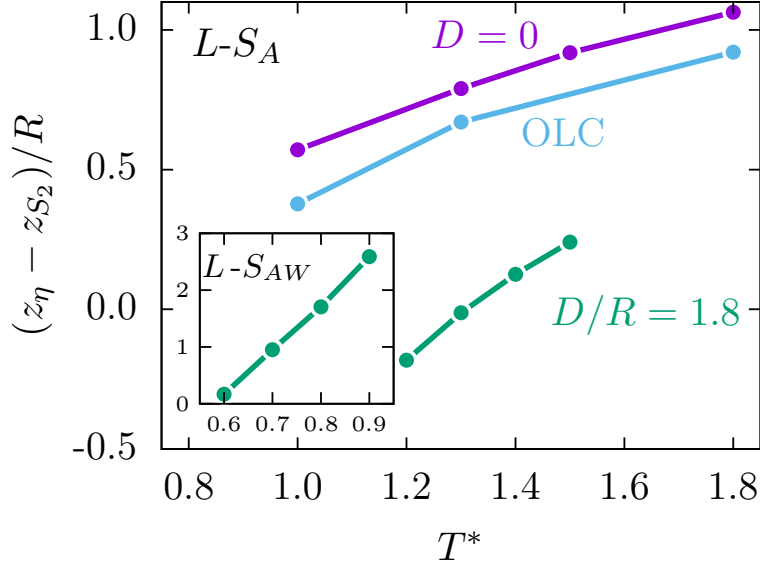


FIGURE 4.3.: The difference $(z_\eta - z_{S_2})/R$ between the Gibbs dividing surface position z_η (Eq. (4.7)), and the surface position z_{S_2} (Eq. (4.8)), which corresponds to the transition of the orientational order at the interface, are shown for three cases. First, an ordinary (uncharged) liquid crystal (OLC; blue curve); second, ILCs with charges in their center, i.e., $D = 0$ (violet curve); and, third, ILCs with charges at the tips, i.e., $D/R = 1.8$ (green curve). The smectic layer normal $\hat{\mathbf{n}} = \hat{\mathbf{z}}$ is parallel to the interface normal, i.e., $\alpha = 0$. In all cases studied, the differences $(z_\eta - z_{S_2})/R$ are smaller than the smectic layer spacing $d \gtrsim L$, which for the S_A phase is comparable to the particle length $L/R = 4$. Thus, the loss of orientational order occurs within the last smectic layer before approaching the isotropic liquid L . The inset shows data for the $L-S_{AW}$ interface, for $D/R = 1.8$, at sufficiently low temperatures T^* . Although the difference $(z_\eta - z_{S_2})/R$ is enlarged for $0.7 < T^* \leq 0.9$, it is still considerably smaller than the smectic layer spacing $d/R \approx 7.5$ and decreases rapidly upon decreasing the temperature T^* . Hence, for $\alpha = 0$, the orientational order of the smectic-A phase, either S_A or S_{AW} , vanishes directly with the disappearance of the layer structure at the interface.

$L/R = 4$, $\varepsilon_R/\varepsilon_L = 2$, and $\gamma/(R\varepsilon_0) = 0$. (compare Fig. 3.4(a) for the relevant phase diagram). Within the considered temperature ranges, in all three cases the differences are at most as large as the length of the particle diameter R , which in turn is much smaller than the smectic layer spacing $d/R \approx 4.3$ which is comparable to the particle

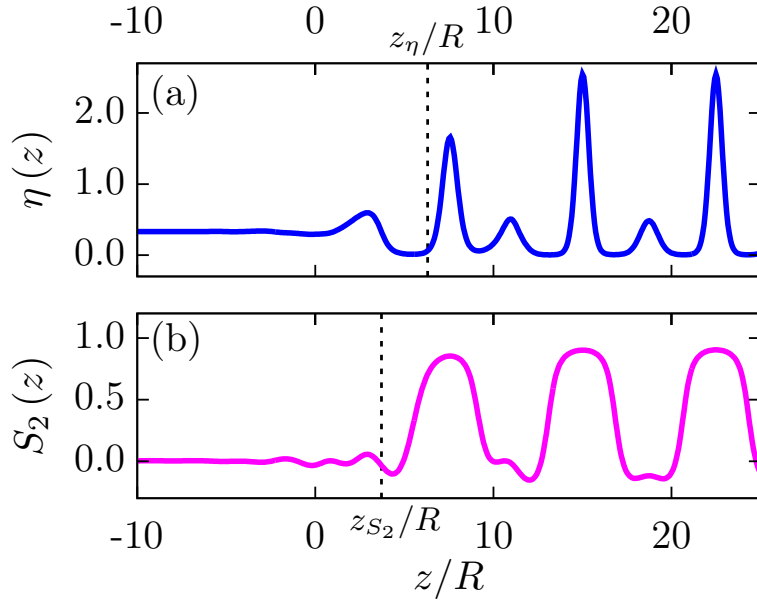


FIGURE 4.4.: For $\alpha = 0$, the L - S_{AW} interface profiles $\eta(z)$ and $S_2(z)$ are shown for ILCs with charges at the tips ($L/R = 4$, $\varepsilon_R/\varepsilon_L = 2$, $\gamma/(R\varepsilon_0) = 0.045$, $\lambda_D/R = 5$, and $D/R = 1.8$) at the reduced temperature $T^* = 0.9$ (see the red dots (•) in Fig. 3.5(b)). For $z \rightarrow -\infty$ the isotropic liquid bulk L is approached whereas for $z \rightarrow \infty$ the S_{AW} bulk is attained. The difference $(z_\eta - z_{S_2})/R \approx 6.31 - 3.72 = 2.59$ between the two interface positions is larger than the one of the L - S_A interface (compare Figs. 4.2 and 4.3) but it is still smaller than the smectic layer spacing $d/R = 7.5$. Therefore the orientational order of the S_{AW} phase also vanishes within the range of the last smectic layer at the interface.

length L , because the particles within the smectic layers are well aligned with the z -direction, indicated by $S_2(z) > 0.8$ in the centers of the smectic layers. Thus, the small size of the differences shows that in these cases the transition in the orientational order and in the fluid structure go along with each other. As soon as the smectic layer structure dies out, the orientational order vanishes as well.

While for ILCs molecules with charges in their center only L - S_A coexistence is expected to occur (because for $D = 0$ the thermodynamic region of the S_{AW} phase is almost completely embedded by the stable regime of crystalline structures; see Fig. 3.5(a)), for ILCs with charges at the tips ($L/R = 4$, $\varepsilon_R/\varepsilon_L = 2$, $\gamma/(R\varepsilon_0) = 0.045$, $\lambda_D/R = 5$, and $D/R = 1.8$), the bulk phase behavior changes significantly at low temperatures,

i.e., for $T^* < 1.23$. The phase diagram for $D/R = 1.8$ (Fig. 3.5(b)) shows that in this case the distinct smectic-A phase S_{AW} in fact occurs in a thermodynamic region below, i.e., at lower temperatures than the ordinary smectic S_A phase and above, i.e., at higher temperatures than genuine crystalline phases. The S_{AW} phase is characterized by an alternating layer structure of smectic layers with a majority of particles being oriented parallel to the smectic layer normal and a minority of particles localized in secondary layers which prefer orientations perpendicular to the layer normal. Due to this alternating layer structure the layer spacing $d/R \approx 7.5$ is increased compared to the S_A phase.

In Fig. 4.4 the L - S_{AW} interface profiles $\eta(z)$ and $S_2(z)$ are shown for $T^* = 0.9$ and $\alpha = 0$. (In the phase diagram in Fig. 3.5(b) the coexisting bulk states are marked by red dots (•).) On the right hand side of Fig. 4.4 the alternating layer structure of the bulk S_{AW} phase is evident. In the main layers the majority of the particles ($\eta(z) > 2$) has orientations parallel to the z -axis ($S_2(z) > 0.8$) and in the secondary layers, formed by less of them ($\eta(z) \approx 0.6$), the particles prefer orientations perpendicular to the z -axis ($S_2(z) < 0$). For the L - S_{AW} interface the difference $(z_\eta - z_{S_2})/R \approx 2.6$ of the two interface positions is increased compared to the L - S_A interface (see Fig. 4.3), because the smectic layer spacing $d/R \geq 7.5$ in the S_{AW} phase is enlarged, too. As before, the orientational order directly vanishes with the disappearance of the layer structure. Furthermore, the inset in Fig. 4.3 shows that $(z_\eta - z_{S_2})/R$ decreases upon lowering the temperature. Thus the difference in the structural and orientational transition becomes smaller relative to the layer spacing d , such that the direct vanishing of the orientational order associated with the disappearance of the layer structure is observable for the whole temperature range considered here.

4.3.2. Interface normal perpendicular to the layer normal

$$(\alpha = \pi/2)$$

For $\alpha = \pi/2$ the (bulk) smectic layer normal and the interface normal are perpendicular to each other. The layer normal points into the x -direction and the interface normal into the z -direction (see Fig. 4.1). The associated L - S_A interface at $T^* = 1.3$ for ILC molecules with their charges concentrated at the center, i.e., $D = 0$, is shown in Fig. 4.5. (The state points of the coexisting bulk phases are marked by orange dots (•) in the phase diagram in Fig. 3.5(a).) Figure 4.5(a) shows the packing fraction $\eta(x, z)$ and (b) the orientational order parameter $S_2(x, z)$. The red areas at the top of panel (a) show

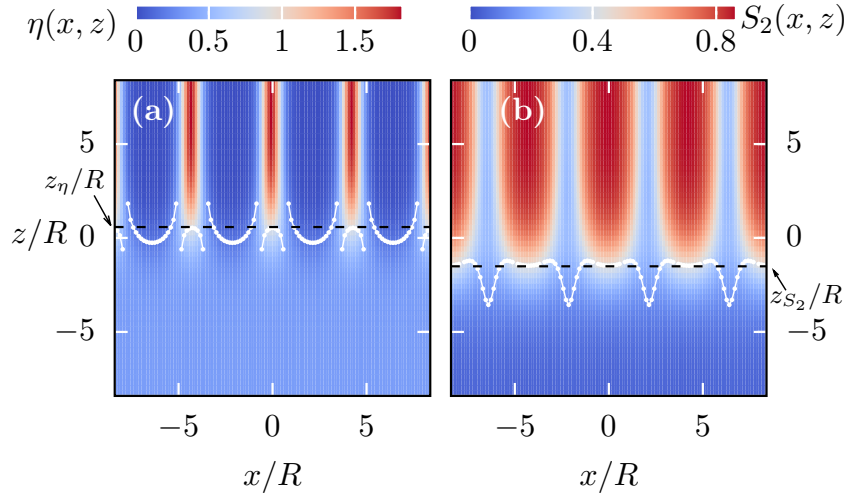


FIGURE 4.5.: The L - S_A interface profiles $\eta(x, z)$, panel (a), and $S_2(x, z)$, panel (b), are shown for $T^* = 1.3$ and $\alpha = \pi/2$. Thus, the smectic layer normal $\hat{\mathbf{n}} = \hat{\mathbf{x}}$ and the interface normal (which is parallel to the z -axis) are perpendicular. Here, ILC molecules with charges at the center are considered, described by the parameter set $L/R = 4$, $\varepsilon_R/\varepsilon_L = 2$, $\gamma/(R\varepsilon_0) = 0.045$, $\lambda_D/R = 5$, and $D = 0$. For $z \rightarrow -\infty$ the isotropic bulk liquid L and for $z \rightarrow \infty$ the bulk of the S_A phase is approached (see the orange dots (•) in Fig. 3.5(a)). The decaying red stripes at the upper part of these plots show the tails of the smectic layers located at $x/R \approx 0, \pm d/R, \pm 2d/R$ where $d/R \approx 4.28$ is the smectic layer spacing. The black dashed lines mark the interface positions z_η and z_{S_2} calculated via Eqs. (4.7) and (4.8), while the white dotted lines mark the interface contours $\tilde{z}_\eta(x)$ and $\tilde{z}_{S_2}(x)$ calculated via Eq. (4.9). The difference $(z_\eta - z_{S_2})/R \approx 0.58 - (-1.51) = 2.09$ is larger than the particle diameter R , which is the relevant geometrical property of the particles at this interface, because for $\alpha = \pi/2$ the ILC particles in the S_A layers are well aligned with the x -axis. Thus, they are oriented preferentially perpendicular to the direction of the interface normal. The orientational order of the S_A phase persists up to a few particle diameters into the liquid phase, unlike the case $\alpha = 0$, considered in Sec. 4.3.1, in which the vanishing of the layer structure causes a direct disappearing of the orientational order within the last considerable smectic layer (see Figs. 4.2-4.4).

the tails of four smectic layers of the S_A phase located at $x/R = \pm d/(2R) \approx \pm 2.14$ and $x/R = \pm 3d/(2R) \approx \pm 6.42$ where $d/R \approx 4.28$ is the (bulk) layer spacing. The particles are well aligned with the smectic layer normal $\hat{\mathbf{n}} = \hat{\mathbf{x}}$ indicated by large values of the orientational order parameter $S_2(x, z) > 0.8$ in the layers.

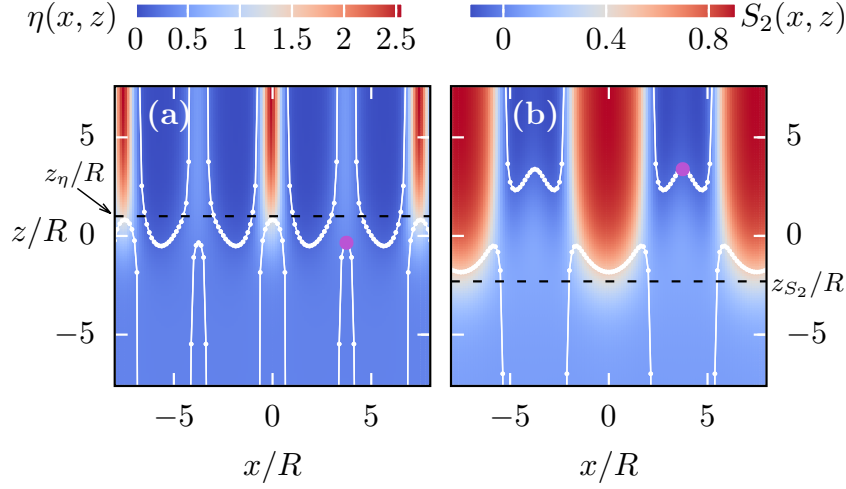


FIGURE 4.6.: The interface profiles $\eta(x, z)$ and $S_2(x, z)$ for $T^* = 0.9$ and $\alpha = \pi/2$. Here the L - S_{AW} interface (see the red dots (•) in Fig. 3.5(b)) for an ILC with the charges at the tips ($L/R = 4$, $\varepsilon_R/\varepsilon_L = 2$, $\gamma/(R\varepsilon_0) = 0.045$, $\lambda_D/R = 5$, and $D/R = 1.8$) is considered. The thin red areas in panel (a) for lateral positions $x/R = 0, \pm d/R = \pm 7.5$ show the tails of the smectic (main) layers where the particles prefer an orientation parallel to the smectic layer normal $\hat{\mathbf{n}} = \hat{\mathbf{x}}$. This is indicated by the large value of $S_2(x, z) > 0.8$ within these layers. In panel (a) the secondary layers of the S_{AW} phase are shown as light blue areas in panel (a) located at $x/R = \pm d/(2R) = \pm 3.75$. There, the orientational order parameter $S_2(x, z)$, shown in panel (b), is negative. The black dashed lines mark the interface positions z_η and z_{S_2} calculated via Eqs. (4.7) and (4.8), while the white dotted lines mark the interface contours $\tilde{z}_\eta(x)$ and $\tilde{z}_{S_2}(x)$, which have been calculated via Eq. (4.9). The differences $(z_\eta - z_{S_2})/R \approx 1.0 - (-2.3) = 3.3$, respectively $(\tilde{z}_\eta(x) - \tilde{z}_{S_2}(x))/R \approx 0.81 - (-1.83) = 2.64$ at the lateral positions $x/R \approx 0, \pm 7.5$, exhibit a persisting orientational order for the main layers, similar to the findings for the L - S_A interface (compare Fig. 4.5). Interestingly, at the secondary layers ($x/R = \pm d/(2R) = \pm 3.75$) the orientational order vanishes ahead of the disappearance of the layer structure, i.e., $\tilde{z}_{S_2}(x/R = \pm 3.75)/R \approx 3.39 > -0.34 \approx \tilde{z}_\eta(x/R = \pm 3.75)/R$. In order to guide the eye, the magenta dots (•) mark the positions $(x/R, \tilde{z}_\eta/R) \approx (3.75, -0.34)$ and $(x/R, \tilde{z}_{S_2}/R) \approx (3.75, 3.39)$.

The black dashed lines in Fig. 4.5 show the interface positions z_η and z_{S_2} calculated from Eqs. (4.7) and (4.8), while the white dotted lines show the interface contours $\tilde{z}_\eta(x)$ and $\tilde{z}_{S_2}(x)$ obtained from Eq. (4.9). The contour lines $\tilde{z}_\eta(x)$ and $\tilde{z}_{S_2}(x)$ at the centers

of the tails of the smectic layers, e.g., at $x/R \approx 2.14$, are very close to z_η and z_{S_2} , respectively. This suggests that the two distinct definitions of the interface positions, i.e., using either Eqs. (4.7) and (4.8) or Eq. (4.9), are consistent with each other, because the majority of the ILC molecules in the smectic phase are located close to the centers of the smectic layers. In Fig. 4.5(a) the packing fraction interface contour $\tilde{z}_\eta(x)$ exhibits discontinuities for lateral positions \tilde{x} at which the packing fraction in the smectic bulk $\eta_{S_A}(\tilde{x}) := \eta(\tilde{x}, z \rightarrow \infty)$ takes the same value $\eta_L = \eta(\tilde{x}, z \rightarrow -\infty)$ as in the liquid L , i.e., $\eta_{S_A}(\tilde{x}) = \eta_L$. Thus, the numerical calculation of the Gibbs dividing surface via Eq. (4.9) leads to a divergence due to the vanishing denominator. Nonetheless this artifact occurs only at the particular lateral positions \tilde{x} . Nevertheless, the benefit of considering $\tilde{z}_\eta(x)$ and $\tilde{z}_{S_2}(x)$ as interface positions is elucidated in the discussion of the last paragraph of this section. For the particular case of the L - S_{AW} interface it is necessary to consider $\tilde{z}_\eta(x)$ and $\tilde{z}_{S_2}(x)$ in order to study the interface at the distinct lateral positions x of the tails of the main layers and of the secondary layers separately.

Interestingly, if the layer normal and the interface normal are perpendicular, one observes a significant difference $(z_\eta - z_{S_2})/R \approx 0.72 - (-1.76) = 2.48$ between the interface position z_η , corresponding to the structural transition, and z_{S_2} corresponding to the transition in the orientational order between the coexisting phases. Hence, the alignment of the particles with the x -axis persists a few particle diameters deeper into the liquid phase L than the layer structure of the S_A phase is maintained – unlike in the case $\alpha = 0$, i.e., in which the smectic layer normal is parallel to the interface normal. For $\alpha = 0$ the orientational order directly vanishes when the smectic layers disappear (see Sec. 4.3.1). It is worth mentioning, that the vanishing of the orientational order significantly after (upon approaching the interface from the orientational ordered phase) the structural transition associated with the density distribution, has already been observed previously [103] in the case of the interface between an isotropic liquid and a plastic-triangular crystal (PTC).

For ILCs with the charges at the tips, at low temperatures the wide smectic-A phase S_{AW} can be observed (see Fig. 3.5(b)). It is characterized by an alternating structure of layers in which the particles are predominantly parallel to the layer normal $\hat{\mathbf{n}} = \hat{\mathbf{x}}$ (like in the S_A phase) and layers of particles which are preferentially perpendicular to the layer normal. The free interface formed between the isotropic liquid L and the S_{AW} phase is shown in Fig. 4.6 for $\alpha = \pi/2$ and $T^* = 0.9$. The red regions in panel (a) show the layers of particles (at $x = 0$ and $x/R \approx \pm d/R = \pm 7.5$) being parallel to the smectic layer normal, while in between (at $x/R \approx \pm d/(2R) = \pm 3.75$) in light blue color the

secondary layers are visible. The dark blue color at $x/R \approx \pm d/(2R) = \pm 3.75$ in panel (b) shows that the orientational order parameter $S_2(x, z)$ is negative at the location of the secondary layers, because there the particles are preferentially perpendicular to the layer normal. The interface at the parallel layers behaves very much like the L - S_A interface, as can be inferred from the (white) interface contours $\tilde{z}_\eta(x/R = 0, \pm 7.5)/R \approx 0.81$ and $\tilde{z}_{S_2}(x/R = 0, \pm 7.5)/R \approx -1.83$ which show that the orientational ordering of the S_{AW} phase persists into the liquid phase L for a few particle diameters. This is also apparent from the interface positions $z_\eta/R \approx 1.0$ and $z_{S_2}/R \approx -2.3$, depicted by the black dashed lines in Fig. 4.6. Conversely, at lateral positions $x/R \approx d/(2R) = \pm 3.75$ associated with the centers of the intermediate layers, it turns out that the orientational order disappears before the layer structure vanishes if one approaches the interface from the S_{AW} side ($\tilde{z}_{S_2}(x/R = \pm 3.75)/R \approx 3.39$ and $\tilde{z}_\eta(x/R = \pm 3.75)/R \approx -0.34$; in order to guide the eye the magenta dots (\bullet) in Fig. 4.6 mark these two positions). This observation is opposite to the aforementioned one and is presumably related to the fact, that the secondary layers consist of ILC particles being preferentially perpendicular to the layer normal; unlike the particles in the main layers of the S_{AW} phase (or the particles in the S_A layers). In the secondary layers of the S_{AW} phase, the particles do not align with the layer normal $\hat{\mathbf{n}} = \hat{\mathbf{x}}$. Instead they are avoiding an orientation parallel to it. For instance the transition across the L - S_A interface – from alignment with the layer normal towards an isotropic orientational distribution – results in an *increase* of the effective particle diameter in the y - and z -direction, however, for the secondary S_{AW} layers the effective diameter is *decreased* from the S_{AW} phase towards the isotropic liquid L . Analogously to Fig. 4.5, in Fig. 4.6, there are discontinuities in the (white) interface contour lines $\tilde{z}_\eta(x)$ and $\tilde{z}_{S_2}(x)$. These occur at lateral positions \tilde{x} at which the packing fraction $\eta(\tilde{x}, z \rightarrow \pm\infty)$ or the orientational order parameter $S_2(\tilde{x}, z \rightarrow \pm\infty)$ take the same value in the isotropic bulk, i.e., for $z \rightarrow -\infty$, as in the S_{AW} bulk, i.e., for $z \rightarrow \infty$.

4.3.3. Asymptotic behavior

In the following section the asymptotic behaviors of the interface profiles of the packing fraction $\eta(\mathbf{r})$ and the orientational order parameter $S_2(\mathbf{r})$ are analyzed. In particular the discussion unrolls how $\eta(\mathbf{r})$ and $S_2(\mathbf{r})$ attain their respective values η_L and $S_{2,L}$ in the bulk liquid L . In Fig. 4.7 the asymptotic behavior is discussed in terms of $\ln|\eta(x, z) - \eta_L|$ and $\ln|S_2(x, z) - S_{2,L}|$ for $T^* = 10$ and $\alpha = \pi/2$, considering ILC molecules with charges in the center, i.e., $D = 0$ (panels (a) and (b)), and with charges

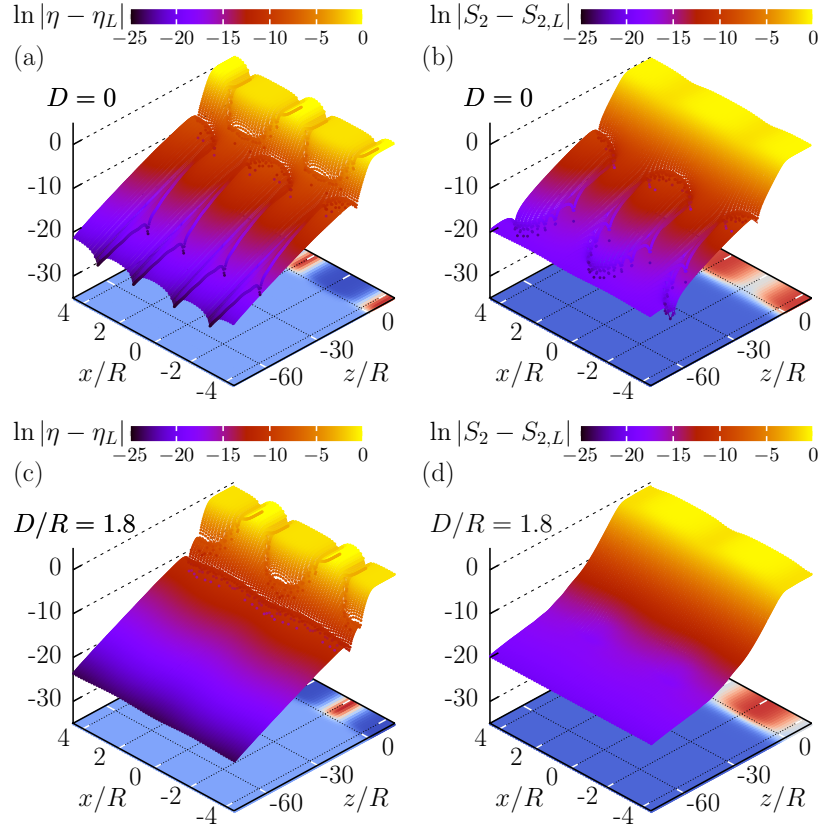


FIGURE 4.7.: L - S_A interface profiles of $\eta(x, z)$ and $S_2(x, z)$ for $T^* = 10$ and $\alpha = \pi/2$. Accordingly, the smectic layer normal $\hat{\mathbf{n}} = \hat{\mathbf{x}}$ and the interface normal (parallel to the z -axis) are perpendicular. Panels (a) and (b) show the logarithmic variations $\ln|\eta(x, z) - \eta_L|$ and $\ln|S_2(x, z) - S_{2,L}|$ of the packing fraction and the orientational order parameter from their bulk values in the isotropic liquid L for an ILC with the charges concentrated at the center of the molecule, i.e., for $D = 0$. Panels (c) and (d) show $\ln|\eta(x, z) - \eta_L|$ and $\ln|S_2(x, z) - S_{2,L}|$ for an ILC with the charges at the tips, i.e., for $D/R = 1.8$. Note that on the base of each plot the interface profiles $\eta(x, z)$ and $S_2(x, z)$ are shown in order to elucidate the viewing angle on the interface. The local height of the manifold above the base corresponds to the given color code. Interestingly, for $D = 0$ the periodic structure is apparent even far away from the L - S_A interface, i.e., $z/R < -20$, unlike the case $D/R = 1.8$, for which the profiles are flat in lateral direction x . This might be a feature caused by the strong localization of the charges in the centers of the smectic layers for $D = 0$, pronouncing the periodic structure, while for $D/R = 1.8$ the charge sites are spread and less localized along the x -direction.

at the tips, i.e., $D/R = 1.8$ (panels (c) and (d)). In order to elucidate the view angle on these 3-dimensional logarithmic plots, the interface profiles $\eta(x, z)$ and $S_2(x, z)$ are also shown as contour plots (compare Fig. 4.5) at the base of the respective plot.

Interestingly, while for $D = 0$ the periodic structure of $\eta(x, z)$ and $S_2(x, z)$ in x -direction is clearly apparent in the decays $\ln |\eta(x, z) - \eta_L|$ and $\ln |S_2(x, z) - S_{2,L}|$ far away from the L - S_A interface ($z/R < -20$ in Figs. 4.7(a) and (b)), for $D/R = 1.8$ (panels (c) and (d)) the decays vary only little as function of x . This distinct behavior can be a signature of the respective molecular charge distributions: if the charges are localized at the centers of the molecules, due to the layer structure in the S_A phase the charges are localized at the centers of the smectic layers, too. However, for $D/R = 1.8$, the charges are less localized along the lateral direction x causing less pronounced (periodic) variations in lateral direction x . Close to the interface ($z/R > -20$) the structure is very similar in both cases and, as will be discussed later, it is the hard-core repulsion which is the dominant contribution here.

Turning the view parallel to the x -axis, one obtains projected representations of the logarithmic plots in Fig. 4.7, which are shown in Fig. 4.8 keeping the order of panels the same as in Fig. 4.7. Hence, Figs. 4.8(a) and (b) correspond to the case $D = 0$ presenting $\ln |\eta(x, z) - \eta_L|$ and $\ln |S_2(x, z) - S_{2,L}|$, respectively. Similarly, Figs. 4.8 (c) and (d) show the case $D/R = 1.8$. In both cases, at large distances, i.e., $z/R < -20$, the decay of the density profiles is dominated by the electrostatic contribution $U_{\text{es}}(\mathbf{r}_{12}, \boldsymbol{\omega}_1, \boldsymbol{\omega}_2)$ to the total interaction potential $U(\mathbf{r}_{12}, \boldsymbol{\omega}_1, \boldsymbol{\omega}_2)$ (see Figs. 4.8(a) and (c)). Accordingly, the decay of the envelope is determined by the Debye screening length $\lambda_D/R = 5$, highlighted by orange lines in Fig. 4.8. Note that a theoretical study [106] of the asymptotic behavior of the liquid-vapor interface, based on DFT, has yielded a decay length l_b larger than the Debye screening length λ_D – unlike the present findings – for a hard sphere system with additional Yukawa interaction. Nonetheless, while in the present study the Yukawa potential is purely repulsive, in Ref. [106] using an attractive Yukawa potential is indispensable, because a sufficiently strong attraction is needed for liquid-vapor coexistence.

Interestingly, the asymptotic behavior of the orientational order parameter at far distances, i.e., for $z/R < -60$, differs from the electrostatic decay, characterized by the decay length $\lambda_D/R = 5$. In fact, another regime (highlighted by blue lines in Fig. 4.8) with larger decay length $\xi_{\text{GB}}/R \approx 10$ sets in. This longer-ranged decay is due to the Gay-Berne interaction $U_{\text{GB}}(\mathbf{r}_{12}, \boldsymbol{\omega}_1, \boldsymbol{\omega}_2)$. This is verified by calculating the interface profile for an (uncharged) ordinary liquid crystal (compare the insets of panels (a) and (b) of

Fig. 4.8). For the OLC, at far distances, i.e., $z/R < -30$, the same large decay length $\xi_{\text{GB}}/R \approx 10$ is observed. However, the amplitudes of the decay of the packing fraction and of the orientational order parameter differ significantly. (The blue line in panel (a) intersects the ordinate at $\ln|\eta - \eta_L| \approx -25$, whereas the blue line in (b) intersects the ordinate at $\ln|S_2 - S_{2,L}| \approx -20$.) For $D = 0$, it turns out that for the orientational order parameter the crossover from the electrostatic decay towards the Gay-Berne decay occurs at $z/R \approx -67$ (in order to guide the eye, this position is marked by the red arrow in Fig. 4.8(b)), whereas for the case $D/R = 1.8$ the crossover occurs at $z/R \approx -45$ (red arrow in Fig. 4.8(d)). Ultimately, the larger Gay-Berne decay length $\xi_{\text{GB}}/R \approx 10$ will become apparent in the decay profile of the packing fraction, too. However, due to the smaller amplitude of the Gay-Berne decay of the density distribution compared with the decay of the orientational order parameter (compare the insets in Figs. 4.8(a) and (b)), in the present cases, the crossover occurs further away from the interface (in Fig. 4.8(a) the intersection of the orange line and the blue line is located at $z/R \approx -121$ (not visible) and in Fig. 4.8(c) at $z/R \approx -97$ (also not visible)). However, at very far distances $z/R < -80$, the magnitudes $\ln|\eta - \eta_L| \lesssim -25$ are very small and cannot be resolved numerically. For this reason, in Figs. 4.8(a) and (c) crossovers from the electrostatic regime to the Gay-Berne regime are not shown.

Note that, although the Gay-Berne potential $U_{\text{GB}}(\mathbf{r}_{12}, \boldsymbol{\omega}_1, \boldsymbol{\omega}_2)$ decays algebraically $\propto (r_{12}/R)^{-6}$ (see Eq. (2.2)), here the Gay-Berne decay is exponential, because solving the Euler-Lagrange equation in Eq. (2.8) requires the evaluation of the ERPA contribution $\beta\psi_{\text{ERPA}}$ of the effective one particle potential $\beta\psi$ (see Eqs. (2.17) and (4.5)). The numerical calculation of this integral (which extends over the whole volume \mathcal{V} of the system) requires a truncation in terms of a cut-off distance of the integral which leads to an exponential decay of this contribution, instead of the expected power law decay $\propto (z/R)^{-3}$ [106–108]. (The exponent 3 arises because the asymptotic behavior of an interfacial density profile, generated by long-ranged forces, varies proportional to the corresponding (total) potential, which acts on a test particle at a distance z from the interface and which is due to the pair interaction between the particles in one of the two coexisting phases (which are separated by the considered interface) and the test particle. Thus, via an integration of the Gay-Berne pair interaction, which decays $\propto (r_{12}/R)^{-6}$ over a half-space, one obtains the corresponding total potential decaying $\propto (z/R)^{-3}$ [107–109].)

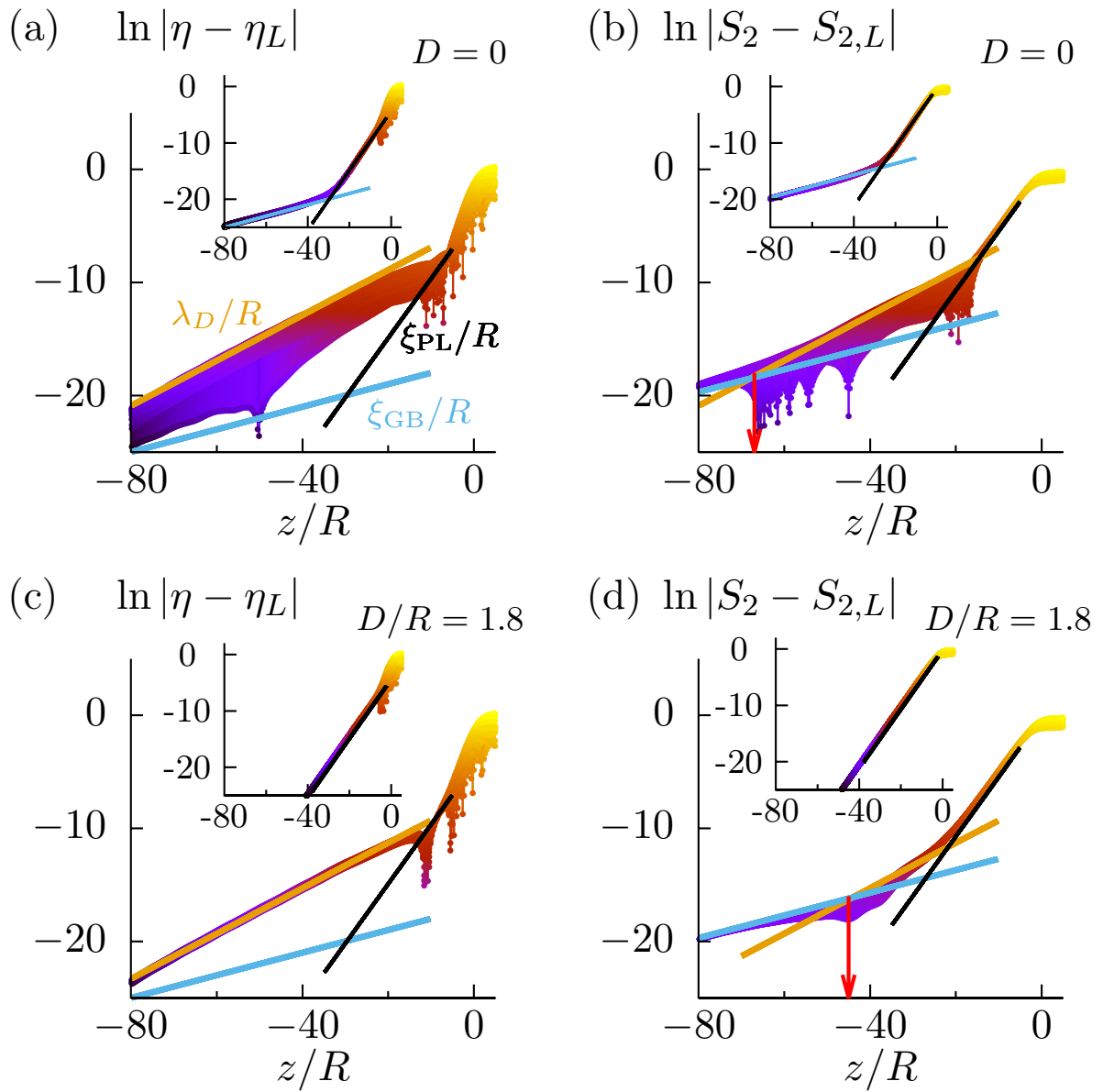


FIGURE 4.8.

FIGURE 4.8.: The same quantities as shown in Fig. 4.7. Panels (a) and (b) correspond to the case $D = 0$ presenting $\ln |\eta(x, z) - \eta_L|$ and $\ln |S_2(x, z) - S_{2,L}|$, respectively, whereas panels (c) and (d) correspond to the case $D/R = 1.8$. However, here the direction of view is parallel to the x -axis so that the manifold from Fig. 4.7 is projected onto the plane spanned by the vertical axis and the z -axis. Away from the interface, i.e., for $z/R < -20$, the decay length for $\ln |\eta(x, z) - \eta_L|$ can be identified as the Debye screening length $\lambda_D/R = 5$ for both cases (a) $D = 0$ and (c) $D/R = 1.8$. From the inset in panel (a), which shows $\ln |\eta(x, z) - \eta_L|$ for the corresponding (uncharged) ordinary liquid crystal (OLC) with $L/R = 4$ and $\varepsilon_R/\varepsilon_L = 2$, it is apparent that the contributions due to the Gay-Berne potential (the asymptotics of which is indicated by the blue line) and due to the hard-core interaction (the asymptotics of which is depicted by the black line) are much weaker than the (screened) electrostatic contribution. They do not play a role within the range of $\ln |\eta(x, z) - \eta_L|$ considered here. (In order to guide the eye, the blue and black lines are also shown in the main plots. Apparently, in (a) and (c) the blue and black lines are far below the respective profiles.) However, for $\ln |S_2(x, z) - S_{2,L}|$, i.e., for panels (b) and (d), one observes crossovers – indicated by the intersection of the orange and blue lines at $z/R \approx -67$ in (b) and $z/R \approx -45$ in (d) (compare the red arrows in the respective plots) – from the electrostatic regime towards the decay governed by the Gay-Berne contribution with decay length $\xi_{\text{GB}}/R \approx 10$. Such crossovers occur within the considered range $z/R \in [-80, 0]$, because for the orientational order parameter the amplitude of the decay, due to the Gay-Berne interaction, is larger than for the packing fraction (compare the intersections of the blue lines with the ordinates in panels (a) and (b)). Due to the hard-core interaction, for $z/R > -20$ the decay length $\xi_{\text{PL}}/R \approx 1.9$ (Parsons-Lee, black lines) is visible for the OLC in the insets of (a) and (b) as well as for $\ln |S_2(x, z) - S_{2,L}|$ of the two considered ILCs. (Due to the small amplitudes of the hard-core contributions to $\ln |\eta(x, z) - \eta_L|$, for the ILCs, this decay has not been observed.) In order to confirm, that the decay length $\xi_{\text{PL}}/R \approx 1.9$ is indeed due to the hard-core interaction, the insets of the panels (c) and (d) show $\ln |\eta(x, z) - \eta_L|$ and $\ln |S_2(x, z) - S_{2,L}|$ of the pure hard-core system ($\beta\psi := \beta\psi_{\text{PL}}$). Interestingly, $\ln |\eta(x, z) - \eta_L|$ and $\ln |S_2(x, z) - S_{2,L}|$ behave very similarly close to the interface, i.e., $z/R > -10$, for all three kinds of systems. This suggests that the structure and the orientational properties close to the interface are governed by the hard-core interaction which enters into the present DFT approach (see Secs. 2.1 and 2.2).

Close to the interface, i.e., for $-20 < z/R < -5$, in the insets of Fig. 4.8 one can observe an exponential decay with a decay length $\xi_{\text{PL}}/R \approx 1.9$ (depicted by the black lines) which arises from the pure hard-core Parsons-Lee contribution $\beta\psi_{\text{PL}}$. Thus ξ_{PL} can be identified as the isotropic-liquid bulk correlation length of the pure hard-core system. Interestingly, while the hard-core correlation length ξ_{PL} is observable in OLCs – within both the η and the S_2 profiles (at distances $z/R \in [-20, -5]$ the respective decays closely follow the black lines which depict the hard-core decay in the insets of Figs. 4.8(a) and (b)) –, for ILCs this decay is visible only within the S_2 profile. Only for the S_2 profile the amplitude of the hard-core decay is large enough, such that the hard-core correlation length ξ_{PL} is observable before the electrostatic decay becomes dominant. In order to verify that the decay close to the interface, i.e., for $-20 < z/R < -5$, is governed by the hard-core interaction, the insets in Figs. 4.8(c) and (d) show the interface profiles calculated for the pure hard-core system, i.e., $\beta\psi := \beta\psi_{\text{PL}}$.

Finally, it is worth mentioning that for all cases shown in Fig. 4.8, the structural and orientational properties close to the interface, i.e., for $z/R > -10$, agree very well. Thus, it is the hard-core interaction which determines the structural and orientational properties close to the interface, while the electrostatic and the Gay-Berne contributions gain significance further away from the interface. At first, at intermediate distances, the electrostatic energy contribution dominates the decay of the interface profiles. However, ultimately, the attractive Gay-Berne interaction determines the decay far away from the interface. Furthermore, the positions of the crossovers between these regimes are distinct for the packing fraction profile and the orientational order parameter profile.

4.3.4. Tilted interfaces

The dependence of the structural and orientational properties of the liquid-smectic interface on the tilt angle α (see Eq. (4.1) and Fig. 4.1) between the smectic layer normal and the interface normal is discussed. In Fig. 4.9 the L - S_A interface profiles $\eta(x, z)$ and $S_2(x, z)$ are shown for the reduced temperature $T^* = 1.3$ (see the orange dots (●) in Fig. 3.5(a)) and $\alpha = \pi/4$. ILCs with the charges localized in the center ($L/R = 4, \varepsilon_R/\varepsilon_L = 2, \gamma/(R\varepsilon_0) = 0.045, \lambda_D/R = 5$, and $D = 0$) are considered. Similar to the case $\alpha = \pi/2$, i.e., the interface normal and the smectic layer normal $\hat{\mathbf{n}} = \hat{\mathbf{x}}$ are perpendicular (see Sec. 4.3.2), a persisting orientational order can be observed at the interface: The structural transition occurs at $z_\eta/R \approx 5.56$, whereas the transition in the orientational order between the two phases takes place at $z_{S_2}/R \approx 2.79$ which is a few

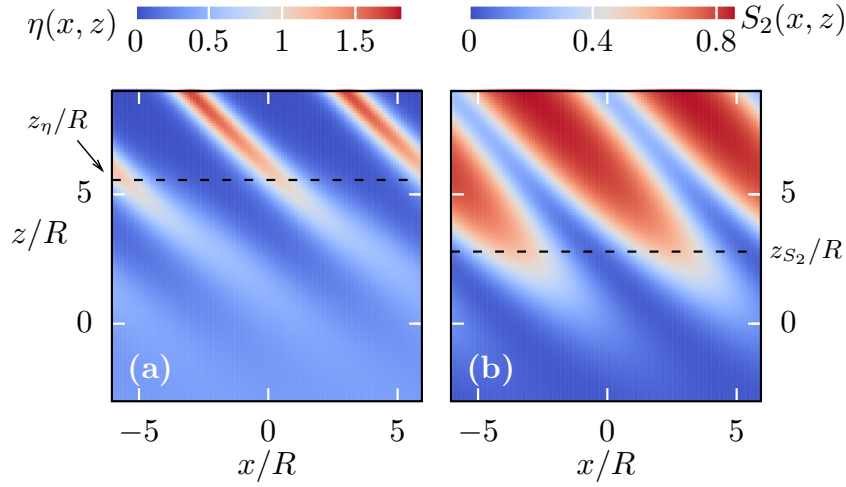


FIGURE 4.9.: The L - S_A interface profiles $\eta(x, z)$ (Eq. (2.19)) and $S_2(x, z)$ (Eq. (2.20)) for $T^* = 1.3$ and $\alpha = \pi/4$. The interface normal is parallel to the z -axis. ILC molecules with charges localized in their centers are considered ($L/R = 4$, $\varepsilon_R/\varepsilon_L = 2$, $\gamma/(R\varepsilon_0) = 0.045$, $\lambda_D/R = 5$, and $D = 0$). For $z \rightarrow -\infty$ the isotropic liquid bulk L is approached and for $z \rightarrow \infty$ the bulk of the S_A phase is attained (compare the orange dots (•) in Fig. 3.5(a)). The red stripes at the top of the contour plots show the tails of the smectic layers. The black dashed lines mark the interface positions $z_\eta/R \approx 5.56$ and $z_{S_2}/R \approx 2.79$ calculated via Eqs. (4.7) and (4.8). Similar to the case $\alpha = \pi/2$ (see Fig. 4.5), to a certain extent the orientational order persists into the liquid phase L .

diameters deeper in the isotropic liquid.

In Fig. 4.10 the interfacial tension $\Gamma^*(\alpha)$ given by Eq. (4.10) and the distance $z_\eta - z_{S_2}$ between the interface positions associated with the mean packing fraction $\eta_0(x)$ and the mean orientational order parameter $S_{20}(x)$ are shown as function of the tilt angle α . In Fig. 4.10(a) the case of the L - S_A interface for ILCs with the charges at their center is considered for $T^* = 1$. Both the interfacial tension $\Gamma^*(\alpha)$ (black dots, •) and the distance $z_\eta - z_{S_2}$ (orange dots, •) exhibit a global minimum at $\alpha = 0$ and a second, local minimum at $\alpha = \pi/2$. Thus, the equilibrium tilt angle $\alpha_{\text{eq}} = 0$ corresponds to the configuration in which the interface normal and the smectic layer normal $\hat{\mathbf{n}} = \hat{\mathbf{z}}$ are parallel, whereas the perpendicular orientation $\alpha = \pi/2$ is metastable. This increase in the interfacial tension Γ^* below $\alpha = \pi/2$ suggests that the configuration, in which the interface normal and the layer normal are orthogonal, should be observable without resorting to any external stabilizing field which could be provided, e.g., by a suitably structured substrate. This

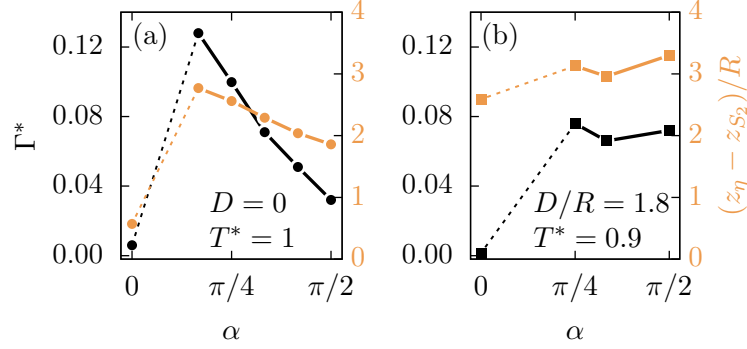


FIGURE 4.10.: The reduced interfacial tension $\Gamma^*(\alpha)$ (Eq. (4.10), black line) and the distance $z_\eta - z_{S_2}$ between the transition in the structural and the orientational order (orange line) as function of the tilt angle α are shown. In panel (a) the L - S_A interface at $T^* = 1$ is considered for ILCs with their charges localized at the center ($L/R = 4, \varepsilon_R/\varepsilon_L = 2, \gamma/(R\varepsilon_0) = 0.045, \lambda_D/R = 5$, and $D = 0$). There are two minima: the global minimum at the equilibrium tilt angle $\alpha_{\text{eq}} = 0$ (i.e., interface normal and smectic layer normal are parallel) and a local minimum at $\alpha = \pi/2$ which shows that the orthogonal orientation of the smectic layer normal and the interface normal is a metastable configuration. The increase of the interfacial tension below $\alpha = \pi/2$ is accompanied by an increase of the distance $z_\eta - z_{S_2}$. This suggests that maintaining the local orientational order to an extent of a few particle diameters into the isotropic liquid costs free energy. For technical reasons small tilt angles $\alpha > 0$ have not been studied. Hence a discussion of the functional form of $\Gamma^*(\alpha)$ for $0 < \alpha < \pi/6$ in the case $D/R = 0$ or for $0 < \alpha < \pi/4$ in the case $D/R = 1.8$ cannot be provided (see the discussion in the main text of Sec. 4.3.4). This is indicated by connecting the data points at $\alpha = 0$ and $\pi/6$ by dashed lines in (a). In panel (b) the L - S_{AW} interface, which is accessible for ILCs with their charges at the tips ($L/R = 4, \varepsilon_R/\varepsilon_L = 2, \gamma/(R\varepsilon_0) = 0.045, \lambda_D/R = 5$, and $D/R = 1.8$), is considered for $T^* = 0.9$. Again the equilibrium tilt angle $\alpha_{\text{eq}} = 0$ corresponds to the parallel orientation of the interface normal and the smectic layer normal. Below $\alpha = \pi/2$, as function of α the interfacial tension is rather flat, taking the value $\Gamma^* \approx 0.07$. Thus, for the L - S_{AW} interface the perpendicular orientation of the interface normal and of the smectic layer normal corresponds to a labile configuration. (Analogously to panel (a), the data points at $\alpha = 0$ and $\pi/4$ in (b) are connected by a dashed line.) Note that $\Gamma^*(\alpha)$ is symmetric around $\alpha = \pi/2$, due to the mirror-symmetry of the considered ILC particles.

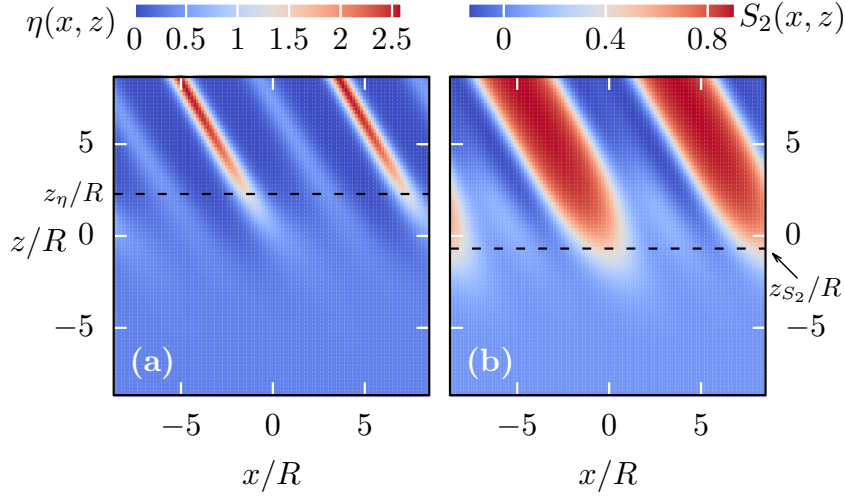


FIGURE 4.11.: Same as Fig. 4.9. Here, the L - S_{AW} interface profiles $\eta(x, z)$ (Eq. (2.19)) and $S_2(x, z)$ (Eq. (2.20)) are shown for $\alpha = \pi/3$ and $T^* = 0.9$. To this end, ILC particles with charges at the tips are considered ($L/R = 4$, $\varepsilon_R/\varepsilon_L = 2$, $\gamma/(R\varepsilon_0) = 0.045$, $\lambda_D/R = 5$, and $D/R = 1.8$). For $z \rightarrow -\infty$ the isotropic liquid bulk L is approached and for $z \rightarrow \infty$ the bulk of the S_{AW} phase (compare the red dots (\bullet) in Fig. 3.5(b)). The transition in the structure occurs at $z_\eta/R \approx 2.28$ and the transition in the orientational order does so at $z_{S_2}/R \approx -0.68$.

metastability of the tilt angle $\alpha = \pi/2$ can be checked also via computer simulations. Interestingly, the increase of the interfacial tension below $\alpha = \pi/2$ is accompanied by an increase in the distance $z_\eta - z_{S_2}$, suggesting that maintaining the local orientational order in the isotropic liquid beyond the smectic layers costs free energy. Consistently, in the case $\alpha = \alpha_{\text{eq}} = 0$, for which the orientational order vanishes directly with the disappearance of the smectic layers, the cost in free energy is lowest.

Apparently, for $\alpha = 0$ the interfacial tension $\Gamma^*(\alpha = 0) \approx 0.006$ is significantly smaller than for all other angles α shown in Fig. 4.10(a). For technical reasons small tilt angles $\alpha > 0$ are not studied. Hence, no discussion of the functional form of $\Gamma^*(\alpha)$ for $0 < \alpha < \pi/6$ in the case $D/R = 0$ or for $0 < \alpha < \pi/4$ in the case $D/R = 1.8$ can be provided. This is indicated by connecting the data points at $\alpha = 0$ and $\pi/6$ by dashed lines. (For the same reason, in (b) the data points at $\alpha = 0$ and $\pi/4$ are connected by dashed lines.) Due to the crossover at the tilt angle $\alpha = 0$ from a periodic system towards one which is translationally invariant in lateral direction x , the integration domain \mathcal{V}_d for evaluating the coefficients $Q_i(\mathbf{r})$ (see Eq. (4.2)) is not continuously evolving at $\alpha = 0$.

Recall that for $\alpha > 0$ it is a slice of length $d_x = d/\sin(\alpha)$ in x -direction, while for $\alpha = 0$ it is the subsystem of length d in z -direction at position \mathbf{r} (see Sec. 4.2.1). (For $\alpha = 0$ the extent in x - and y -direction is arbitrary due to the translational invariance in lateral direction.) In order to describe a continuous variation of the interfacial tension $\Gamma^*(\alpha)$ for all tilt angles $\alpha \in [0, \pi/2]$, one needs to consider a different approach, which does not rely on a projected density and thereby on the direction of the bulk smectic layer normal $\hat{\mathbf{n}}$ throughout the whole interface structure. Nonetheless, the present approach still allows one to compare the interfacial tension $\Gamma^*(\alpha)$ for the extreme cases $\alpha = 0$ and $\pi/2$, thus predicting which one of the two is preferred. Furthermore, the approach provides an understanding of the local increase in $\Gamma^*(\alpha)$ below $\alpha = \pi/2$, as one observes an increasing distance $z_\eta - z_{S_2}$ between the transition in the structural and the orientational order at the interface.

Figure 4.10(b) shows data for the L - S_{AW} interface at $T^* = 0.9$ for ILCs with charges located at the tips. Around $\alpha = \pi/2$ the interfacial tension (black squares, \blacksquare) is a rather flat function of α taking values around $\Gamma^* \approx 0.07$. The slight variations in Γ^* for $\alpha \in [\pi/4, \pi/2]$ might be caused by the numerical evaluation of Eq. (2.8) which has to be done separately for each tilt angle α . Consistently, the distance $z_\eta - z_{S_2}$ (orange squares, \blacksquare) does not vary much as function of the tilt angle α . As above, the equilibrium tilt angle $\alpha_{\text{eq}} = 0$ corresponds to the configuration in which the interface normal and the smectic layer normal $\hat{\mathbf{n}} = \hat{\mathbf{z}}$ are parallel. In Fig. 4.11, the contour plot of the L - S_{AW} interface for $\alpha = \pi/3$ and $T^* = 0.9$ for an ILC system with $D/R = 1.8$ is shown, in order to illustrate the structure of this type of interface.

4.4. Conclusions

In this chapter free interfaces in systems composed of ionic liquid crystals (ILCs) have been studied within density functional theory (see Sec. 2.2 and 4.2.1). In particular, the discussion has been focused on two particular kinds of ionic liquid crystals: first, ILC molecules with the charges localized at their centers, i.e., $D = 0$ (see Figs. 2.1 and 2.2), and, second, ILCs with the charges at the tips of the molecules, i.e., $D/R = 1.8$. All other model parameters, i.e., $L/R = 4$, $\varepsilon_R/\varepsilon_L = 2$, $\gamma/(R\varepsilon_0) = 0.045$, $\lambda_D/R = 5$, are identical in both cases. Therefore the two kinds differ solely by the charge distribution within the molecules.

For $D = 0$ coexistence between the isotropic liquid L and the ordinary smectic-A

phase S_A can be observed at sufficiently large mean packing fraction η_0 and temperatures $T^* > 0.9$ (see Fig. 3.5(a)). The S_A phase is characterized by a layered structure in the direction of the smectic layer normal $\hat{\mathbf{n}}$ with a smectic layer spacing $d \approx L$ comparable to the particle length L . Within the smectic layers the particles are well aligned with the smectic layer normal. The phase behavior of ILCs is altered by varying the molecular charge distribution, as can be inferred from comparing the case $D = 0$ (i.e., charges at the center) and $D/R = 1.8$ (i.e., charges at the tips, see Fig. 3.5(b)). For $D/R = 1.8$ at temperatures $T^* < 1.23$ a new smectic-A phase has been observed, which is referred to as the S_{AW} phase (see Sec. 3.3.1). The S_{AW} phase shows an alternating structure of layers with the majority of the particles being oriented parallel to the smectic layer normal $\hat{\mathbf{n}}$ and the minority of the particles localized in secondary layers which prefer orientations perpendicular to $\hat{\mathbf{n}}$. Due to the alternating layer structure, the smectic layer spacing $d/R \approx 7.5$ in the S_{AW} phase is increased compared with the layer spacing in the S_A phase.

For a parallel orientation of the smectic layer normal $\hat{\mathbf{n}} = \hat{\mathbf{z}}$ and the L - S_A interface normal, i.e., for $\alpha = 0$ (see Fig. 4.1), it turns out that the interface locations z_η and z_{S_2} , associated with the transition in the structural and in the orientational order, respectively, are very close to each other (see Fig. 4.2). In fact, Fig. 4.3 shows that for the whole temperature range considered, the difference $z_\eta - z_{S_2} < d$ in the two interface positions is smaller than the smectic layer spacing d . Hence, for $\alpha = 0$ the orientational order vanishes within the last smectic layer at the L - S_A interface. Concerning the interface positions, Fig. 4.3 demonstrates that ILCs with $D/R = 1.8$ and ordinary (uncharged) liquid crystals with $L/R = 4$ and $\varepsilon_R/\varepsilon_L = 2$ exhibit qualitatively the same results. Considering the L - S_{AW} interface (see Fig. 4.4) one observes an increase in $z_\eta - z_{S_2}$, but it remains significantly smaller than the smectic layer spacing $d/R \approx 7.5$. Thus, it turns out that, if the layer normal is parallel to the interface normal, the loss of orientational order coincides with the disappearance of the layer structure of the respective smectic-A phase at the interface. This holds for all parameter values studied.

Interestingly, for $\alpha = \pi/2$, i.e., changing the relative orientation of the smectic layer normal and the interface normal such that they are perpendicular to each other, leads to qualitative changes in the interfacial properties: a periodic structure of the interface in lateral direction x can be observed, which is a direct consequence of the periodicity in the bulk smectic-A phase with the smectic layer spacing d (see Figs. 4.1, 4.5, and 4.6). For the L - S_A interface (see Fig. 4.5) one observes considerable differences $(z_\eta - z_{S_2})/R \gtrsim 2$ between the interface positions. Thus, the preferred parallel orientation of particles in

the S_A layers persists for a few particle diameters R into the liquid phase L , unlike the case $\alpha = 0$, for which the orientational order vanishes directly with the disappearance of the S_A layer structure at the interface. Due to the periodicity in the x -direction, in the case $\alpha = \pi/2$ one indeed observes a qualitative change in the structure of the L - S_{AW} interface compared to the L - S_A interface. While at the tails of the S_{AW} main layers the interface also features an orientational order which continues further into the liquid phase L than the layer structure ($(\tilde{z}_\eta(x) - \tilde{z}_{S_2}(x))/R \approx 2.6$), for the secondary layers it is the (layer) structure that persists deeper into the L phase than the orientational order ($(\tilde{z}_\eta(x) - \tilde{z}_{S_2}(x))/R \approx -3.73$). The opposite behavior at the main, respectively secondary, layers is presumably driven by their orientational properties: in the main layers the particles are well aligned with the smectic layer normal $\hat{\mathbf{n}} = \hat{\mathbf{x}}$ and therefore show an effective diameter in the y - z -plane which is comparable to the particle diameter R . However, in the secondary layers the particles avoid orientations parallel to the x -axis (recall that $S_2(x, z) < 0$ at the secondary layers), giving rise to an considerably larger effective radius. Upon approaching the liquid phase L , this effective radius *increases* for the main layers of the S_{AW} phase, whereas it *decreases* for the secondary layers.

In Sec. 4.3.3 the asymptotic behavior of the interface profiles has been studied. In particular, in Figs. 4.7 and 4.8 the L - S_A interface for $\alpha = \pi/2$ has been considered for the two ILC systems with $D/R = 0$ and 1.8. For $D = 0$, i.e., ILC molecules with the charges being localized at the center, the periodic structure of the interface is apparent from the quantities $\ln |\eta(x, z) - \eta_L|$ and $\ln |S_2(x, z) - S_{2,L}|$, showing the logarithmic deviations of the profiles $\eta(x, z)$ and $S_2(x, z)$ from their respective liquid bulk values η_L and $S_{2,L}$ (Figs. 4.8(a) and (b)), which can be resolved even at far distances $z/R < -20$ from the L - S_A interface. Conversely, for $D/R = 1.8$, i.e., the charges being fixed at the tips, far from the interface $\ln |\eta(x, z) - \eta_L|$ and $\ln |S_2(x, z) - S_{2,L}|$ vary only marginally as function of the lateral coordinate x . While for $D = 0$ the charges are strongly localized at the centers of the smectic layers, thus promoting the periodic structure, for $D/R = 1.8$ the charges are less localized and fairly distributed along the x -direction.

The asymptotic decays of the interface profiles towards the isotropic liquid L yield an interesting and rich behavior. Three distinct spatial regimes, each of them associated to one of the three respective contributions to the underlying pair potential (Eq. (2.1)). Although the presence of charges is the distinctive feature of ILCs, compared to other liquid-crystalline materials, the (screened) electrostatic contribution to the interaction (Eq. (2.5)) governs the asymptotic decay only at intermediate distances from the interface (see Fig. 4.8). In this regime, the decay length is given by the Debye screening

length, here $\lambda_D/R = 5$. Ultimately, it is the attractive Gay-Berne contribution to the interaction (Eq. (2.2)) which dominates the outermost asymptotic behavior; for the system studied here a considerably large decay length $\xi_{GB}/R \approx 10$ is observed, which is due to the truncated power law decay of the GB potential. Close to the interface, the hard-core interaction, incorporated by the Parsons-Lee contribution (Eq. (2.15)), dominates the profiles $\eta(x, z)$ and $S_2(x, z)$. The corresponding decay length $\xi_{PL}/R \approx 1.9$ is comparable to the particle diameter R . This is plausible, because for the case considered here the tilt angle is $\alpha = \pi/2$, i.e., the smectic layer normal is perpendicular to the interface normal, and thus the particles in the S_A layers are oriented preferentially perpendicular to the interface normal as well. The crossovers between these three different regimes occur at distances characteristic for the packing fraction $\eta(x, z)$ and the orientational order parameter $S_2(x, z)$. While for both types of ILCs considered in Fig. 4.8 all three decay lengths ξ_{PL} , ξ_{GB} , and λ_D are apparent from $\ln |S_2(x, z) - S_{2,L}|$, from $\ln |\eta(x, z) - \eta_L|$ only the decay length λ_D can be inferred within the considered range $z/R > -80$. This is caused by the relative magnitudes of the respective decay amplitudes: for the packing fraction profile the decay amplitudes due to the Gay-Berne and the hard-core interaction are too small, compared to the corresponding amplitude due to the electrostatic interaction, to be observable.

Since the structural and orientational properties directly at the interface are determined by the hard-core interaction, i.e., the Parsons-Lee contribution $\beta\psi_{PL}$ (Eq. (2.15)), to the effective one-particle potential $\beta\psi$, close to the interface the profiles for ordinary liquid crystals (OLCs) and ILCs with the same length-to-breadth ratio L/R are very similar. This observation includes particularly the interface positions z_η and z_{S_2} (Fig. 4.3) associated with the transitions in the structural and orientational order. Nevertheless the asymptotic behavior, as discussed above, is distinct for the different kinds of particles (hard ellipsoids, OLCs, and ILCs) and shows a rich phenomenology, specifically for ILCs, due to the crossovers between the distinct spatial regimes corresponding to the various contributions to the pair potential. At this point it is worth recalling that, the bulk phase behavior is also different for the three types of particles; in particular only for the ILCs with charges at the tips, the S_{AW} is found to be stable in a considerable thermodynamic region (see Sec. 3.3.1).

Finally, the dependence of the structural and orientational properties of liquid-smectic interfaces on the tilt angle α between the interface normal and the smectic layer normal has been discussed. For the L - S_A interface (Fig. 4.10(a)), it turns out, that the parallel orientation of the interface normal and the smectic layer normal is the one in

thermal equilibrium, i.e., $\alpha_{\text{eq}} = 0$. The perpendicular orientation $\alpha = \pi/2$ is metastable. Interestingly, the increase in the interfacial tension below $\alpha = \pi/2$ is accompanied by an increase in the distance $z_\eta - z_{S_2}$ between the structural and orientational interface position. This result suggests that maintaining the local orientational order beyond the smectic layers towards the (isotropic) liquid phase costs free energy. Consistently, in the case $\alpha = \alpha_{\text{eq}} = 0$, for which the orientational order vanishes directly with the disappearance of the smectic layers, the cost of free energy for forming the interface is lowest. For the L - S_{AW} interface (Fig. 4.10(b)) again the equilibrium tilt angle $\alpha_{\text{eq}} = 0$ corresponds to the parallel orientation of the interface and smectic layer normal. However, around $\alpha = \pi/2$, the interfacial tension $\Gamma^*(\alpha)$ varies only weakly so that in this case the perpendicular orientation is labile.

CONCLUSIONS AND OUTLOOK

The present findings are reviewed in the light of the initial motivation of this dissertation and the contribution it provides to the field of ionic liquid crystals. Potential starting points and related subjects for future investigations based on the present results will be discussed as well.

In this dissertation ionic liquid crystals (ILCs) have been investigated by means of density functional theory (DFT) and Monte Carlo simulations. To this end an effective one-species model (Chapter 2) has been employed in which one of the ionic species (i.e., either the anions or the cations) is not explicitly accounted for. Instead, these so-called *counterions* are incorporated as a structureless background medium giving rise to screening of the charges of the cations, respectively of the anions, (called *coions*) on the length scale of the Debye screening length λ_D . The coions are modeled as rigid hard ellipsoids of length-to-breadth ratio L/R and as to carry two charge sites, each located at a distance D from the molecular center along the coion long axis (Fig. 2.1). Besides the hard-core repulsion and the screened electrostatic repulsion, two coions interact via the Gay-Berne potential, incorporating (mainly attractive) van der Waals forces (see Eq. (2.1) and Fig. 2.2). Consequently, the occurrence of liquid-crystalline behavior, i.e., the emergence of mesophases, is exclusively driven by the orientational and structural ordering of the coions. This can be considered as a reasonable approximation for ILCs with a considerable difference in size of the two ionic species, e.g., 1-dodecyl-3-methylimidazolium (cation) and iodide (anion) [2, 36, 80]. For this particular ILC the structural and orientational properties of its mesophases are primarily due to the formation of nanostructures by the cations, while the anions are not contributing to these structures, because they are much smaller in size. Yet, they can be used for charge transport through the nanostructures of the cations [39].

Such a simplistic model is naturally limited to materials – like the aforementioned ILC – which exhibit these specific properties in order to give quantitatively reliable predictions. Nonetheless, the comprehensibility and transparency of this simple theoretical description allow one to study the relation between intrinsic properties of the molecules and the resulting macroscopic material properties, because within this model microscopic parameters can easily be varied. In this regard, first, the dependence of the bulk phase behavior of ILCs on the length-to-breadth ratio and on the loci of the charges of the underlying molecules has been investigated (Chapter 3). The emergence of different types of smectic-A phases, depending on these parameters, has been observed (see Figs. 3.2, 3.3, 3.5, and 3.6). Interesting and new kinds of smectic-A phases have been observed, among those the peculiar S_{AW} phase, which emerges for the case of ILC molecules of length-to-breadth ratio $L/R = 4$ and with charges located at their tips, i.e., $D/R = 1.8$. The S_{AW} phase is characterized by a wider smectic layer spacing as compared to the one for the ordinary smectic-A phase S_A (Fig. 3.8). Moreover the S_{AW} phase shows an alternating layer structure of particles being oriented parallel to

the layer normal and particles preferring orientations perpendicular to it (Fig. 3.9). This structure is indeed promoted by the charges located at the tips, which lead to a repulsion of neighboring smectic layers of parallel particles. The opened space in between is then filled by particles with orientations mostly perpendicular to the layer normal. It turns out that, only for this particular ILC system (among those which have been studied within the scope of this dissertation, including in particular ordinary, i.e., uncharged, liquid crystals) the S_{AW} phase is stable in a considerably large thermodynamic region of the temperature versus density phase diagram, i.e., below the ordinary S_A phase and above the crystalline phases (Fig. 3.5). This sensitive dependence of the phase behavior on the particular values of the molecular parameters stresses the exceptional properties of ILC materials. Moreover, the stability of the S_{AW} phase originates from the interplay between the (anisotropic) liquid-crystalline properties and the electrostatic interactions of the ILC molecules. This underscores that – although technically demanding – a theoretical approach covering both aspects is in fact necessary in order to describe such phenomena.

While the present Monte Carlo simulations confirm the existence of the S_{AW} phase for the present molecular model (Fig. 3.12), it would be interesting to investigate whether for ILC systems the S_{AW} phase can be observed experimentally. In particular the nonvanishing size and the distribution of the counterions could affect the stability of the S_{AW} phase. In order to investigate this stability theoretically, the present approach could be extended by explicitly incorporating counterions into the model, for example as charged spheres of nonzero radius. Such an enhancement implies a significant increase in the complexity of the theory as it represents not only a two-species description, but in addition one would need to account for the unscreened electrostatic Coulomb potential acting between the ions, which leads to further technical subtleties. (Further details concerning these technical features are provided in the discussion of theoretical approaches describing ionic fluids in Chapter 1.) Nevertheless, a more sophisticated theoretical description could lead to interesting insights on how the smectic structures, observed within the present approach, are altered by the nonvanishing size of the counterions and how they are distributed among the smectic layers formed by the coions.

Another modification of the present model would be to consider different kinds of charge distributions. For instance, instead of assuming symmetric charge distributions like in the present case, studying, e.g., a single charge site located on one side of the ILC molecules. This would extend the model to a wider class of ILC materials, for which additional types of mesophases might occur.

Having analyzed carefully the bulk properties, a natural extension of theoretical studies of soft matter systems consists of investigating spatially inhomogeneous systems, such as free interfaces between coexisting bulk phases. First of all, one can directly make use of the obtained bulk results, because they are needed as boundary conditions for the analysis of the corresponding interface. Furthermore studying inhomogeneous systems can provide deeper insights into the structure formation and the orientational properties at interfaces between these anisotropic systems. In particular, in Chapter 4, interfaces between the isotropic liquid L and the ordinary smectic-A phase S_A , respectively the wide smectic-A phase S_{AW} phase, have been discussed. An interesting aspect, which can be studied at isotropic-smectic interfaces, is, how the structure and the orientational ordering within the smectic phases disappears upon approaching the isotropic liquid. For varying the tilt angle α between the interface normal and the smectic layer normal, quantitatively distinct profiles of the density and the orientational order parameter have been observed. If the interface normal is parallel to the layer normal, i.e., $\alpha = 0$, the orientational order vanishes directly along with the disappearance of the smectic layers at the isotropic-smectic interface (see Figs. 4.2 and 4.4). On the contrary, if the layer normal and interface normal are perpendicular, i.e., $\alpha = \pi/2$, an orientational order has been found to penetrate into the isotropic liquid (see Figs. 4.5 and 4.6). At the same time the interfacial tension is found to be lowest for $\alpha = 0$, i.e., the parallel orientation of the interface and the smectic layer normal is the stable configuration. These results suggest that the persistence of the orientational order in the isotropic liquid phase increases the free energy. Thus the present theory provides a microscopic understanding of the observable interfacial tension in terms of the underlying structural and orientational behavior of the molecules at the interface. The analysis of the decays of the interfacial profiles of the density and of the orientational order parameter has shown, that all distinct energy contributions, i.e., the hard-core, the Gay-Berne, and the electrostatic interaction, to the pair interaction potential can precisely be identified from the decays of these profiles towards their bulk values. Interestingly, while the bulk phase behavior depends very sensitively on the microscopic parameters, the interfacial properties are found to be rather robust upon varying the model parameters.

The S_A - S_{AW} interface is another remarkable type of a free interface. In the phase diagram in Fig. 3.5(b), a first-order phase transition from the S_{AW} to the S_A phase has been observed by increasing the density at sufficiently low temperature. However, the current DFT approach is not appropriate for studying this interface. For the L - S_A interface, respectively the L - S_{AW} interface, considered here, the value of the (bulk)

layer spacing, which is determined by the periodicity of the bulk density profiles, is used throughout the whole interfacial system in order to calculate the non-local coefficients $Q_i(\mathbf{r}, [\varrho])$ (Eq. (4.2)) of the projected number density $\bar{\varrho}(\mathbf{r}, \boldsymbol{\omega})$. This is possible due to the homogeneity for all degrees of freedom of the isotropic liquid phase L , which therefore does not require a specific value for the periodicity. However, for the S_A - S_{AW} interface the smectic layer spacings differ in both bulk states. Thus, a different approach is necessary, which either allows for a free adjustment of the layer spacing at each position \mathbf{r} or requires a free energy functional which is not based on the (phenomenological) introduction of the projected density, which is designed to obtain (bulk) profiles which are periodic in one dimension, i.e., isotropic, nematic, and smectic phases. Instead, such a description would rather rely on geometrical properties of the underlying particles, as it is the case for the free energy functionals of the *fundamental measure theory* class. Nonetheless, due to the anisotropy of the particles this is a significant increase of the complexity of the theory and the development of such free energy functionals is still an ongoing process [88–91, 110].

In addition, an ILC system close to an electrode is an interesting subject to study, because it is of relevance for technological applications of ILCs as electrolyte materials, e.g., in dye-sensitized solar cells [2, 39] (see Sec. 3.1). In this respect, the present approach can be utilized by introducing an external potential into Eq. (2.7), which describes the interaction of the ILC particles with the electrode. In this context also wetting phenomena can be studied.

Appendix A

Derivation of Eq. (3.1)

As explained below Eq. (2.14), for bulk phases one has $Q_i = \text{const.}$ Accordingly, Eq. (2.15) reduces to

$$\beta\psi_{\text{PL}}(\mathbf{r}, \boldsymbol{\omega}, [\bar{\varrho}]) = -\mathcal{J}(Q_0) \times \int_{\mathcal{V}} d^3r' \int_S d^2\omega' \bar{\varrho}(\mathbf{r}', \boldsymbol{\omega}') f_M(\mathbf{r} - \mathbf{r}', \boldsymbol{\omega}, \boldsymbol{\omega}'). \quad (\text{A.1})$$

Using the definition in Eq. (2.12) of the projected density $\bar{\varrho}(\mathbf{r}, \boldsymbol{\omega})$, with $Q_i = \text{const}$ for bulk phases, one obtains six terms in the integrand of Eq. (A.1), one for each Q_i , $i = 0, \dots, 5$. Changing the integration variable from \mathbf{r}' to $\tilde{\mathbf{r}} = \mathbf{r}' - \mathbf{r}$ yields

$$\begin{aligned} \beta\psi_{\text{PL}}(\mathbf{r}, \boldsymbol{\omega}, [\bar{\varrho}]) = & -\frac{\mathcal{J}(Q_0)}{4\pi} \left[Q_0 \int_{\mathcal{V}} d^3\tilde{r} \int_S d^2\omega' f_M(\tilde{\mathbf{r}}, \boldsymbol{\omega}, \boldsymbol{\omega}') \right. \\ & + Q_1 \cos(2\pi z/d) \int_{\mathcal{V}} d^3\tilde{r} \int_S d^2\omega' f_M(\tilde{\mathbf{r}}, \boldsymbol{\omega}, \boldsymbol{\omega}') \cos(2\pi\tilde{z}/d) \\ & + Q_2 \cos(4\pi z/d) \int_{\mathcal{V}} d^3\tilde{r} \int_S d^2\omega' f_M(\tilde{\mathbf{r}}, \boldsymbol{\omega}, \boldsymbol{\omega}') \cos(4\pi\tilde{z}/d) \\ & + Q_3 \int_{\mathcal{V}} d^3\tilde{r} \int_S d^2\omega' f_M(\tilde{\mathbf{r}}, \boldsymbol{\omega}, \boldsymbol{\omega}') 5P_2(\cos(\vartheta')) \\ & + Q_4 \cos(2\pi z/d) \int_{\mathcal{V}} d^3\tilde{r} \int_S d^2\omega' f_M(\tilde{\mathbf{r}}, \boldsymbol{\omega}, \boldsymbol{\omega}') 5P_2(\cos(\vartheta')) \cos(2\pi\tilde{z}/d) \\ & \left. + Q_5 \cos(4\pi z/d) \int_{\mathcal{V}} d^3\tilde{r} \int_S d^2\omega' f_M(\tilde{\mathbf{r}}, \boldsymbol{\omega}, \boldsymbol{\omega}') 5P_2(\cos(\vartheta')) \cos(4\pi\tilde{z}/d) \right], \quad (\text{A.2}) \end{aligned}$$

where the relation $\cos(x + y) = \cos(x)\cos(y) - \sin(x)\sin(y)$ has been utilized. Note that the integration domains \mathcal{V} (associated with \mathbf{r}') and $\tilde{\mathcal{V}}$ (associated with $\tilde{\mathbf{r}}$) become equal and approach the three-dimensional space \mathbb{R}^3 . Unlike in the case of dipolar flu-

ids [111], due to the absence of long-ranged interactions, here the free energy functional does not depend on the sample shape. Thus, asymptotically the replacement of $\tilde{\mathcal{V}}$ by \mathcal{V} is valid. The integrals involving terms proportional to $\sin(y)$ vanish because the Mayer f-function f_M is even in $\tilde{\mathbf{r}}$. Note that via $f_M(\tilde{\mathbf{r}}, \boldsymbol{\omega}, \boldsymbol{\omega}')$ the integrals in Eq. (A.2) still carry a non-trivial dependence on the polar angle ϑ . However, the effective one-particle potential $\beta\psi[\bar{\varrho}]$ follows from integrating Eq. (A.2) over $\boldsymbol{\omega}$ and inserting this into Eq. (2.18), rendering the corresponding Legendre expansion coefficients $\zeta_l(\mathbf{r})$. Using Eqs. (A.2) and (2.18), one finds that $\beta\psi[\bar{\varrho}]$ has the same dependence on z and ϑ as the projected density. Note, that for the contribution $\beta\psi_{\text{ERPA}}[\bar{\varrho}]$ to the effective one-particle potential, due to interactions beyond the contact distance $|\mathbf{r}_{12}| \geq R\sigma$ (Eq. (2.17)), one obtains the same result concerning the spatial and the orientational dependence, because $(1 + f_M(\tilde{\mathbf{r}}, \boldsymbol{\omega}, \boldsymbol{\omega}'))\beta U(\tilde{\mathbf{r}}, \boldsymbol{\omega}, \boldsymbol{\omega}')$ is an even function of $\tilde{\mathbf{r}}$, too.

The dependence on \mathbf{r} and $\boldsymbol{\omega}$ of the integral in Eq. (2.11) involves, inter alia, the functional derivative $\frac{\delta\bar{\varrho}(\mathbf{r}'', \boldsymbol{\omega}'', [\varrho])}{\delta\varrho(\mathbf{r}, \boldsymbol{\omega})}$. Again using the definition of the projected density (Eqs. (2.12)-(2.14)) one finds

$$\begin{aligned} \frac{\delta\bar{\varrho}(\mathbf{r}'', \boldsymbol{\omega}'', [\varrho])}{\delta\varrho(\mathbf{r}, \boldsymbol{\omega})} &= \frac{1}{4\pi} \Theta(d/2 - |z - z''|) \left[1 + \right. \\ &2 \cos(2\pi z/d) \cos(2\pi z''/d) + 2 \cos(4\pi z/d) \cos(4\pi z''/d) + \\ &5P_2(\cos(\vartheta))P_2(\cos(\vartheta''))(1 + 2 \cos(2\pi z/d) \cos(2\pi z''/d) + \\ &\left. 2 \cos(4\pi z/d) \cos(4\pi z''/d)) \right]. \end{aligned} \quad (\text{A.3})$$

Thus, the second summand in Eq. (2.11) shares the same type of dependence on z and ϑ like the first summand. Finally, the equilibrium profile follows from solving Eq. (2.8), which indeed exhibits the generic form given by Eq. (3.1). Note, that concerning the bulk phases the Heaviside step function $\Theta(d/2 - |z - z'|)$ acts only as to confine the spatial integration domain to a single periodic cell, but does not generate a further dependence on the position z , because the bulk phases are considered to have a periodic structure only.

It is worth mentioning that the same line of argument holds for the solution following from the modified one-particle direct correlation function $\tilde{c}^{(1)}$ in Eq. (3.3), because here the first term is again given by the effective one-particle potential $\beta\psi[\bar{\varrho}]$ and the second term is constant for periodic bulk phases (see above). Thus, this solution has the same functional form as Eq. (3.1).

Appendix B

Comparison between the exact and the approximate bulk solution

Consider an ILCs described by the parameter set $L/R = 4, D/R = 1.8, \lambda_D/R = 5, \varepsilon_R/\varepsilon_L = 2$, and $\gamma/(R\varepsilon_0) = 0.045$ (see Sec. 2.1). The corresponding phase diagram, obtained by the modified Euler-Lagrange equation (Eqs. (2.8) and (3.3)), is shown in Fig. 3.5(b). In order to compare the exact solution and the solution of the modified Euler-Lagrange equation, three thermodynamic state points (T^*, μ^*) are considered in the phase diagram. For $(T^*, \mu^*) = (0.8, 20)$, the modified Euler-Lagrange equation yields a stable, (wide) smectic phase S_{AW} with $\eta_0 \approx 0.5002, \tilde{W}_0 := W_0 LR^2\pi/6 \approx 0.7059, S_{20} \approx 0.3646, W_2 \approx 0.7605$ (Eq. (3.5)), and smectic layer spacing $d/R \approx 7.71$. For the same state point the exact solution also belongs to the S_{AW} phase with $\eta_0 \approx 0.5002, \tilde{W}_0 \approx 0.7058, S_{20} \approx 0.3657, W_2 \approx 0.7603$ and smectic layer spacing $d/R \approx 7.70$. Choosing a state point at a higher temperature $(T^*, \mu^*) = (1.2, 18)$, which corresponds to the same mean packing fraction η_0 (hence, the two considered state points lie on a vertical line in the corresponding phase diagram (Fig. 3.5(b))), one finds that for these values the solution of the modified Euler-Lagrange equation belongs to the high-temperature smectic S_A phase with $d/R \approx 4.50, \eta_0 \approx 0.5045, \tilde{W}_0 \approx 0.9207, S_{20} \approx 0.7418, W_2 \approx 0.2680$, as the exact solution does (with $d/R \approx 4.52, \eta_0 \approx 0.5049, \tilde{W}_0 \approx 0.9218, S_{20} \approx 0.7373, W_2 \approx 0.2774$). At the state point $(T^*, \mu^*) = (0.8, 29)$ the mean packing fraction is increased to $\eta_0 \approx 0.59$ for which both schemes predict a transition from the S_{AW} to the S_A phase (compare Table B.1). Although the exact location of the phase transition between the observed bulk phases might be slightly shifted, both minimization schemes give rise to the same qualitative phase behavior. Moreover, for the considered cases a good agreement even on a quantitative level has been found. Finally, Table B.1 summarizes the

results for the order parameters and the smectic layer spacing d for the stable smectic phases as predicted by both solutions at the considered state points $(T^*, \mu^*) = (0.8, 20)$, $(0.8, 29)$, and $(1.2, 18)$.

method	(T^*, μ^*)	stable phase	d/R	η_0	\tilde{W}_0	S_{20}	W_2
I	(0.8, 20)	S_{AW}	7.70	0.5002	0.7058	0.3657	0.7603
I	(0.8, 29)	S_A	4.55	0.5858	1.1138	0.8063	0.2307
I	(1.2, 18)	S_A	4.52	0.5049	0.9218	0.7373	0.2774
II	(0.8, 20)	S_{AW}	7.71	0.5002	0.7059	0.3646	0.7605
II	(0.8, 29)	S_A	4.60	0.5862	1.1147	0.7885	0.2645
II	(1.2, 18)	S_A	4.50	0.5045	0.9207	0.7418	0.2680

TABLE B.1.: Comparison of the results for the exact solution of the Euler-Lagrange equation (method I, Eqs. (2.8)-(2.11)) and the solution obtained from the modified one-particle direct correlation function $\tilde{c}^{(1)}$ given by Eq. (3.3) (method II) for three thermodynamic state points (T^*, μ^*) . The results of both methods for the layer spacing d/R , the mean packing fraction η_0 , the first Fourier mode $\tilde{W}_0 = W_0 LR^2 \pi/6$ of the local packing fraction $\eta(z)$, the mean scalar orientational order parameter S_{20} , and the first Fourier mode W_2 of the scalar orientational order parameter profile $S_2(z)$ are compared (see Eq. (3.5)).

Appendix C

Derivation of Eq. (3.8)

In order to calculate the reduced pressure $p^* = -\beta\Omega[\varrho^{\text{eq}}]/V$, the grand potential functional $\beta\Omega[\varrho]$ (see Eq. (2.7)) is evaluated for the bulk solution $\varrho^{\text{eq}}(\mathbf{r}, \boldsymbol{\omega})$ of the modified Euler-Lagrange equation, which solves Eq. (2.8) with the modified one-particle direct correlation function $\tilde{c}^{(1)}$ given by Eq. (3.3):

$$\begin{aligned}
p^* &= -\frac{\beta\Omega[\varrho^{\text{eq}}]}{\mathcal{V}} \\
&= -\frac{\beta\mathcal{F}[\varrho^{\text{eq}}]}{\mathcal{V}} - \frac{1}{\mathcal{V}} \int_{\mathcal{V}} d^3r \int_S d^2\omega \varrho^{\text{eq}}(\mathbf{r}, \boldsymbol{\omega}) \left[\tilde{c}^1(\mathbf{r}, \boldsymbol{\omega}, [\varrho^{\text{eq}}]) - 1 \right] \\
&= \frac{1}{\mathcal{V}} \int_{\mathcal{V}} d^3r \int_S d^2\omega \varrho^{\text{eq}}(\mathbf{r}, \boldsymbol{\omega}) \left[\frac{1}{2} \beta\psi(\mathbf{r}, \boldsymbol{\omega}, \bar{\varrho}[\varrho^{\text{eq}}]) + 1 \right. \\
&\quad \left. - \frac{\partial_{Q_0}\mathcal{J}(Q_0)}{2\mathcal{V}_d} \int_{\mathcal{V}} d^3r' \int_S d^2\omega' \bar{\varrho}(\mathbf{r}', \boldsymbol{\omega}') \Theta(d/2 - |z - z'|) \times \right. \\
&\quad \left. \int_{\mathcal{V}} d^3r'' \int_S d^2\omega'' \bar{\varrho}(\mathbf{r}'', \boldsymbol{\omega}'') f_M(\mathbf{r}' - \mathbf{r}'', \boldsymbol{\omega}', \boldsymbol{\omega}'') \right]. \tag{C.1}
\end{aligned}$$

In the third step of Eq. (C.1), the definition of the excess free energy functional (Eq. (2.10)) has been used. Since the last two terms of Eq. (C.1) depend on the position \mathbf{r} and the orientation $\boldsymbol{\omega}$ only via $\varrho^{\text{eq}}(\mathbf{r}, \boldsymbol{\omega})$, the integrals over \mathbf{r} and $\boldsymbol{\omega}$ can be carried out:

$$\begin{aligned}
p^* &= \frac{1}{2\mathcal{V}_d} \int_{\mathcal{V}_d} d^3r \int_S d^2\omega \varrho^{\text{eq}}(\mathbf{r}, \boldsymbol{\omega}) \beta\psi(\mathbf{r}, \boldsymbol{\omega}, \bar{\varrho}[\varrho^{\text{eq}}]) + \\
&\quad + n_0 - n_0 \frac{\partial_{Q_0}\mathcal{J}(Q_0)}{2\mathcal{V}_d} \int_{\mathcal{V}_d} d^3r' \int_S d^2\omega' \bar{\varrho}(\mathbf{r}', \boldsymbol{\omega}') \times \\
&\quad \int_{\mathcal{V}} d^3r'' \int_S d^2\omega'' \bar{\varrho}(\mathbf{r}'', \boldsymbol{\omega}'') f_M(\mathbf{r}' - \mathbf{r}'', \boldsymbol{\omega}', \boldsymbol{\omega}''), \tag{C.2}
\end{aligned}$$

using $n_0 = \int_{\mathcal{V}} d^3r \int_{\mathcal{S}} d^2\omega \varrho^{\text{eq}}(\mathbf{r}, \boldsymbol{\omega})$. In the first term \mathcal{V} has been replaced by \mathcal{V}_d because the entire (bulk) system of volume \mathcal{V} can be considered to be composed of a set of periodic cells of volume \mathcal{V}_d (see Sec. 2.2 below Eq. (2.14)). In order to simplify the first term of Eq. (C.2), it is convenient to rewrite the equilibrium density profile $\varrho^{\text{eq}}(\mathbf{r}, \boldsymbol{\omega}) = n^{\text{eq}}(\mathbf{r})f^{\text{eq}}(\mathbf{r}, \boldsymbol{\omega})$ as the product of the total number density $n(\mathbf{r})$ and the orientational distribution function $f(\mathbf{r}, \boldsymbol{\omega})$. Additionally using the definition of the effective one-particle potential $\beta\psi(\mathbf{r}, \boldsymbol{\omega})$ (given as a Legendre polynomial series up to second order with the expansion coefficients $\zeta_l(\mathbf{r})$, $l = 0, 2$, see Eq. (2.18)) leads to

$$\begin{aligned}
p^* = & n_0 + \frac{1}{4\mathcal{V}_d} \int_{\mathcal{V}_d} d^3r n^{\text{eq}}(\mathbf{r}) [\zeta_0(\mathbf{r}) + S_2^{\text{eq}}(\mathbf{r})\zeta_2(\mathbf{r})] \\
& - n_0 \frac{\partial_{Q_0} \mathcal{J}(Q_0)}{2\mathcal{V}_d} \int_{\mathcal{V}_d} d^3r' \int_{\mathcal{S}} d^2\omega' \bar{\varrho}(\mathbf{r}', \boldsymbol{\omega}') \times \\
& \int_{\mathcal{V}} d^3r'' \int_{\mathcal{S}} d^2\omega'' \bar{\varrho}(\mathbf{r}'', \boldsymbol{\omega}'') f_M(\mathbf{r}' - \mathbf{r}'', \boldsymbol{\omega}', \boldsymbol{\omega}''), \tag{C.3}
\end{aligned}$$

which coincides with Eq. (3.8).

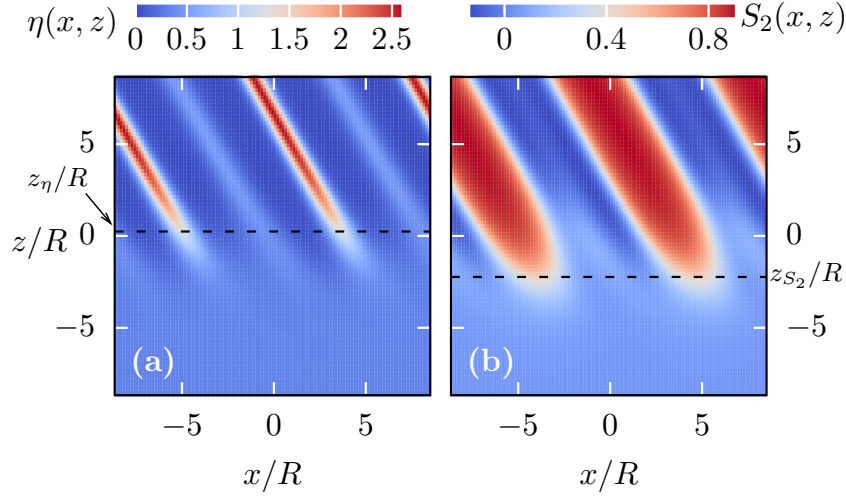


FIGURE D.1.: Same as Fig. 4.11. Here, the L - S_{AW} interface profiles $\eta(x, z)$ (Eq. (2.19)) and $S_2(x, z)$ (Eq. (2.20)) are calculated for $\alpha = \pi/3$ and $T^* = 0.9$ using the projected density containing odd Fourier-modes up to second order. The profiles are qualitatively equivalent to those obtained without using the odd modes in the projected density $\bar{\varrho}(\mathbf{r}, \omega)$ (Eq. (2.12)). In agreement with the results shown in Fig. 4.11 one observes an orientational order (within the main layers of the S_{AW} phase) persisting up to a few particle diameter R into the liquid phase ($(z_\eta - z_{S_2})/R = 0.24 - (-2.23) = 2.47$).

Appendix D

Implications of the presence of odd Fourier modes in $\bar{\varrho}(\mathbf{r}, \omega)$

In this appendix the implications of considering the occurrence of odd Fourier modes – up to second-order ones – within the projected density $\bar{\varrho}(\mathbf{r}, \omega)$ are discussed. Including

these terms, $\bar{\varrho}(\mathbf{r}, \boldsymbol{\omega})$ takes the following modified form:

$$\begin{aligned}
\bar{\varrho}(\mathbf{r}, \boldsymbol{\omega}, [\varrho]) &= \frac{1}{4\pi} \left[Q_0(\mathbf{r}, [\varrho]) + Q_1(\mathbf{r}, [\varrho]) \cos(2\pi(\mathbf{r} \cdot \hat{\mathbf{n}})/d) \right. \\
&+ Q_2(\mathbf{r}, [\varrho]) \cos(4\pi(\mathbf{r} \cdot \hat{\mathbf{n}})/d) + 5P_2(\boldsymbol{\omega} \cdot \hat{\mathbf{n}}) \left(Q_3(\mathbf{r}, [\varrho]) \right. \\
&+ Q_4(\mathbf{r}, [\varrho]) \cos(2\pi(\mathbf{r} \cdot \hat{\mathbf{n}})/d) + Q_5(\mathbf{r}, [\varrho]) \cos(4\pi(\mathbf{r} \cdot \hat{\mathbf{n}})/d) \left. \right) \\
&+ Q_6(\mathbf{r}, [\varrho]) \sin(2\pi(\mathbf{r} \cdot \hat{\mathbf{n}})/d) + Q_7(\mathbf{r}, [\varrho]) \sin(4\pi(\mathbf{r} \cdot \hat{\mathbf{n}})/d) \\
&+ 5P_2(\boldsymbol{\omega} \cdot \hat{\mathbf{n}}) \left(Q_8(\mathbf{r}, [\varrho]) \sin(2\pi(\mathbf{r} \cdot \hat{\mathbf{n}})/d) \right. \\
&\left. \left. + Q_9(\mathbf{r}, [\varrho]) \sin(4\pi(\mathbf{r} \cdot \hat{\mathbf{n}})/d) \right) \right]. \tag{D.1}
\end{aligned}$$

Eq. (D.1) differs from Eq. (2.12) by the (odd Fourier-)terms corresponding to the coefficients $Q_i(\mathbf{r})$ with $i \in [6, \dots, 9]$:

$$Q_i(\mathbf{r}, [\varrho]) = \frac{1}{\mathcal{V}_d} \int_{\mathcal{V}} d^3 r' \int_{\mathcal{S}} d^2 \omega' \varrho(\mathbf{r}', \boldsymbol{\omega}') w_i(\mathbf{r}, \mathbf{r}', \boldsymbol{\omega}'), \tag{D.2}$$

where

$$\begin{aligned}
w_6 &= 2\mathcal{T}(\mathbf{r} - \mathbf{r}') \sin(2\pi(\mathbf{r}' \cdot \hat{\mathbf{n}})/d), \\
w_7 &= 2\mathcal{T}(\mathbf{r} - \mathbf{r}') \sin(4\pi(\mathbf{r}' \cdot \hat{\mathbf{n}})/d), \\
w_8 &= 2\mathcal{T}(\mathbf{r} - \mathbf{r}') P_2(\boldsymbol{\omega}' \cdot \hat{\mathbf{n}}) \sin(2\pi(\mathbf{r}' \cdot \hat{\mathbf{n}})/d), \\
w_9 &= 2\mathcal{T}(\mathbf{r} - \mathbf{r}') P_2(\boldsymbol{\omega}' \cdot \hat{\mathbf{n}}) \sin(4\pi(\mathbf{r}' \cdot \hat{\mathbf{n}})/d). \tag{D.3}
\end{aligned}$$

The coefficients Q_i with $i \in [6, \dots, 9]$ vanish for the considered bulk phases, because smectic-A phases exhibit mirror-symmetry with respect to the layer center. At interfaces they do not vanish, in general. In order to compare the corresponding interface profiles $\eta(\mathbf{r}) = \frac{\pi}{6} LR^2 \int_{\mathcal{S}} d^2 \omega \varrho(\mathbf{r}, \boldsymbol{\omega})$ and $S_2(\mathbf{r}) = \int_{\mathcal{S}} d^2 \omega f(\mathbf{r}, \boldsymbol{\omega}) P_2(\boldsymbol{\omega} \cdot \hat{\mathbf{n}})$ (see Eqs. (2.19) and (2.20), respectively; \mathcal{S} is the full solid angle) obtained from solving the Euler-Lagrange equation, i.e., Eq. (2.8), by using the projected density without the odd terms given by Eq. (2.12) and the projected density containing these terms, i.e., by using Eq. (D.2), the case $\alpha = \pi/3$ (see Eq. (4.1)) and the L - S_{AW} interface shown in Fig. 4.11 are considered again. In Fig. D.1 the two respective profiles are shown by using Eq. (D.1): for both $\eta(\mathbf{r})$ and $S_2(\mathbf{r})$ there are no qualitative differences compared with Fig. 4.11. The

interface positions $z_\eta/R \approx 0.24$ and $z_{S_2}/R \approx -2.23$, corresponding to the structural and orientational transitions, are shifted in z -direction compared to the results shown in Fig. 4.11. But their distance $(z_\eta - z_{S_2})/R \approx 2.47$ is comparable to the previous results ($(z_\eta - z_{S_2})/R \approx 2.96$ in Fig. 4.11). Hence, in qualitative agreement with the results shown in Fig. 4.11 one observes a persisting orientational order (within the main layers of the S_{AW} phase) up to a few particle diameters R into the liquid phase.

Bibliography

- [1] K. Binnemans. *Ionic Liquid Crystals*. Chem. Rev. **105**, 4148 (2005).
- [2] N. Yamanaka, R. Kawano, W. Kubo, T. Kitamura, Y. Wada, M. Watanabe, and S. Yanagida. *Ionic liquid crystal as a hole transport layer of dye-sensitized solar cells*. Chem. Comm. **41**, 740 (2005).
- [3] T. Kato. *From Nanostructured Liquid Crystals to Polymer-Based Electrolytes*. Ang. Chem. Int. Ed. **49**, 7847 (2010).
- [4] P.-G. de Gennes and J. Prost. *The Physics of Liquid Crystals* (Oxford University Press, Oxford, 1974), 2 edn.
- [5] J.-P. Hansen and I. R. McDonald. *Theory of Simple Liquids* (Academic Press, Amsterdam, 1986).
- [6] J. M. Kosterlitz and D. J. Thouless. *Long range order and metastability in two dimensional solids and superfluids. (Application of dislocation theory)*. J. Phys. C: Solid State Phys. **5**, L124 (1972).
- [7] J. M. Kosterlitz and D. J. Thouless. *Ordering, metastability and phase transitions in two-dimensional systems*. J. Phys. C: Solid State Phys. **6**, 1181 (1973).
- [8] J. M. Kosterlitz. *The critical properties of the two-dimensional xy model*. J. Phys. C: Solid State Phys. **7**, 1046 (1974).
- [9] A. Jaster. *The hexatic phase of the two-dimensional hard disk system*. Phys. Lett. A **330**, 120 (2004).
- [10] R. Pindak, D. E. Moncton, S. C. Davey, and J. W. Goodby. *X-Ray Observation of a Stacked Hexatic Liquid-Crystal B Phase*. Phys. Rev. Lett. **46**, 1135 (1981).

- [11] S. Chandrasekhar, B. K. Sadashiva, and K. A. Suresh. *Liquid crystals of disc-like molecules*. Pramana **9**, 471 (1977).
- [12] S. Laschat, A. Baro, N. Steinke, F. Giesselmann, C. Hägele, G. Scalia, R. Judele, E. Kapatsina, S. Sauer, A. Schreivogel, and M. Tosoni. *Discotic Liquid Crystals: From Tailor-Made Synthesis to Plastic Electronics*. Angew. Chem. Int. Ed. **46**, 4832 (2007).
- [13] J.-C. P. Gabriel, C. Sanchez, and P. Davidson. *Observation of Nematic Liquid-Crystal Textures in Aqueous Gels of Smectite Clays*. J. Phys. Chem. **100**, 11139 (1996).
- [14] J. L. Lebowitz and E. H. Lieb. *Existence of Thermodynamics for Real Matter with Coulomb Forces*. Phys. Rev. Lett. **22**, 631 (1969).
- [15] E. H. Lieb and J. L. Lebowitz. *The constitution of matter: Existence of thermodynamics for systems composed of electrons and nuclei*. Adv. Math. **9**, 316 (1972).
- [16] F. H. Stillinger and R. Lovett. *Ion-Pair Theory of Concentrated Electrolytes. I. Basic Concepts*. J. Chem. Phys. **48**, 3858 (1968).
- [17] F. H. Stillinger and R. Lovett. *General Restriction on the Distribution of Ions in Electrolytes*. J. Chem. Phys. **49**, 1991 (1968).
- [18] R. Lovett and F. H. Stillinger. *Ion-Pair Theory of Concentrated Electrolytes. II. Approximate Dielectric Response Calculation*. J. Chem. Phys. **48**, 3869 (1968).
- [19] D. Mitchell, D. A. McQuarrie, A. Szabo, and J. Groeneveld. *On the second-moment condition of Stillinger and Lovett*. J. Stat. Phys. **17**, 15 (1977).
- [20] P. Martin and C. Gruber. *A new proof of the Stillinger-Lovett complete shielding condition*. J. Stat. Phys. **31**, 691 (1983).
- [21] S. Wiegand, J. M. H. Levelt Sengers, K. J. Zhang, M. E. Briggs, and R. W. Gammon. *Discrepancies in turbidity measurements in the ionic binary mixture triethyl n-hexyl ammonium triethyl n-hexyl boride in diphenyl ether*. J. Chem. Phys. **106**, 2777 (1997).

- [22] S. Wiegand, R. F. Berg, and J. M. H. Levelt Sengers. *Critical viscosity of the ionic mixture triethyl n-hexyl ammonium triethyl n-hexyl borate in diphenyl ether*. J. Chem. Phys. **109**, 4533 (1998).
- [23] S. Wiegand, M. E. Briggs, J. M. H. Levelt Sengers, M. Kleemeier, and W. Schröer. *Turbidity, light scattering, and coexistence curve data for the ionic binary mixture triethyl n-hexyl ammonium triethyl n-hexyl borate in diphenyl ether*. J. Chem. Phys. **109**, 9038 (1998).
- [24] H. L. Bianchi and M. L. Japas. *Phase equilibria of a near-critical ionic system. Critical exponent of the order parameter*. J. Chem. Phys. **115**, 10472 (2001).
- [25] A. Z. Panagiotopoulos. *Critical parameters of the restricted primitive model*. J. Chem. Phys. **116**, 3007 (2002).
- [26] E. Luijten, M. E. Fisher, and A. Z. Panagiotopoulos. *Universality Class of Criticality in the Restricted Primitive Model Electrolyte*. Phys. Rev. Lett. **88**, 185701 (2002).
- [27] Y. C. Kim and M. E. Fisher. *Discretization Dependence of Criticality in Model Fluids: A Hard-Core Electrolyte*. Phys. Rev. Lett. **92**, 185703 (2004).
- [28] H. Bartsch, O. Dannenmann, and M. Bier. *Thermal and structural properties of ionic fluids*. Phys. Rev. E **91**, 042146 (2015).
- [29] M. E. Fisher. *The story of coulombic criticality*. J. Stat. Phys. **75**, 1 (1994).
- [30] V. Kobelev, A. B. Kolomeisky, and M. E. Fisher. *Lattice models of ionic systems*. J. Chem. Phys. **116**, 7589 (2002).
- [31] M. E. Fisher and Y. Levin. *Criticality in ionic fluids: Debye-Hückel theory, Bjerrum, and beyond*. Phys. Rev. Lett. **71**, 3826 (1993).
- [32] M. A. Gebbie, M. Valtiner, X. Banquy, E. T. Fox, W. A. Henderson, and J. N. Israelachvili. *Ionic liquids behave as dilute electrolyte solutions*. Proc. Natl. Acad. Sci. USA **110**, 9674 (2013).
- [33] A. A. Lee, D. Vella, S. Perkin, and A. Goriely. *Are Room-Temperature Ionic Liquids Dilute Electrolytes?* J. Phys. Chem. Lett. **6**, 159 (2015).

- [34] A. M. Smith, A. A. Lee, and S. Perkin. *The Electrostatic Screening Length in Concentrated Electrolytes Increases with Concentration*. J. Phys. Chem. Lett. **7**, 2157 (2016).
- [35] A. A. Lee, C. S. Perez-Martinez, A. M. Smith, and S. Perkin. *Underscreening in concentrated electrolytes*. Faraday Discuss. **199**, 239 (2017).
- [36] K. Goossens, K. Lava, C. W. Bielawski, and K. Binnemans. *Ionic liquid crystals: versatile materials*. Chem. Rev. **116**, 4643 (2016).
- [37] M. Yoshio, T. Kagata, K. Hoshino, T. Mukai, H. Ohno, and T. Kato. *One-Dimensional Ion-Conductive Polymer Films: Alignment and Fixation of Ionic Channels Formed by Self-Organization of Polymerizable Columnar Liquid Crystals*. J. Am. Chem. Soc. **128**, 5570 (2006).
- [38] P. Bruce, B. Scrosati, and J.-M. Tarascon. *Nanomaterials for Rechargeable Lithium Batteries*. Ang. Chem. Int. Ed. **47**, 2930 (2008).
- [39] N. Yamanaka, R. Kawano, W. Kubo, N. Masaki, T. Kitamura, Y. Wada, M. Watanabe, and S. Yanagida. *Dye-Sensitized TiO₂ Solar Cells Using Imidazolium-Type Ionic Liquid Crystal Systems as Effective Electrolytes*. J. Phys. Chem. B **111**, 4763 (2007).
- [40] C. K. Lee, H. W. Huang, and I. J. B. Lin. *Simple amphiphilic liquid crystalline-alkylimidazolium salts. A new solvent system providing a partially ordered environment*. Chem. Comm. **36**, 1911 (2000).
- [41] G. Stell, K. C. Wu, and B. Larsen. *Critical Point in a Fluid of Charged Hard Spheres*. Phys. Rev. Lett. **37**, 1369 (1976).
- [42] M. J. Gillan. *Liquid-vapour equilibrium in the restricted primitive model for ionic liquids*. Mol. Phys. **49**, 421 (1983).
- [43] R. Dickman and G. Stell. *Phase diagram of the lattice restricted primitive model*. AIP Conf. Proc. **492**, 225 (1999).
- [44] A. Z. Panagiotopoulos and S. K. Kumar. *Large Lattice Discretization Effects on the Phase Coexistence of Ionic Fluids*. Phys. Rev. Lett. **83**, 2981 (1999).

- [45] J. M. Caillol, D. Levesque, and J. J. Weis. *A Monte Carlo finite size scaling study of charged hard-sphere criticality*. J. Chem. Phys. **107**, 1565 (1997).
- [46] G. Orkoulas and A. Z. Panagiotopoulos. *Phase behavior of the restricted primitive model and square-well fluids from Monte Carlo simulations in the grand canonical ensemble*. J. Chem. Phys. **110**, 1581 (1999).
- [47] L. Onsager. *The effects of shape on the interaction of colloidal particles*. Ann. N. Y. Acad. Sci. **51**, 627 (1949).
- [48] W. Maier and A. Saupe. *Eine einfache molekulare Theorie des nematischen kristallinflüssigen Zustandes*. Z. Naturforschung A **13**, 564 (1958).
- [49] W. Maier and A. Saupe. *Eine einfache molekular-statistische Theorie der nematischen kristallinflüssigen Phase. Teil I¹*. Z. Naturforschung A **14**, 882 (1959).
- [50] W. Maier and A. Saupe. *Eine einfache molekular-statistische Theorie der nematischen kristallinflüssigen Phase. Teil II*. Z. Naturforschung A **15**, 287 (1960).
- [51] W. L. McMillan. *Simple Molecular Model for the Smectic A Phase of Liquid Crystals*. Phys. Rev. A **4**, 1238 (1971).
- [52] W. L. McMillan. *X-Ray Scattering from Liquid Crystals. I. Cholesteryl Nonanoate and Myristate*. Phys. Rev. A **6**, 936 (1972).
- [53] J. P. Straley. *Liquid Crystals in Two Dimensions*. Phys. Rev. A **4**, 675 (1971).
- [54] J. P. Straley. *Frank Elastic Constants of the Hard-Rod Liquid Crystal*. Phys. Rev. A **8**, 2181 (1973).
- [55] J. P. Straley. *Theory of piezoelectricity in nematic liquid crystals, and of the cholesteric ordering*. Phys. Rev. A **14**, 1835 (1976).
- [56] P. Sheng and P. J. Wojtowicz. *Constant-coupling theory of nematic liquid crystals*. Phys. Rev. A **14**, 1883 (1976).
- [57] T. Kato, N. Mizoshita, and K. Kishimoto. *Functional Liquid-Crystalline Assemblies: Self-Organized Soft Materials*. Ang. Chem. Int. Ed. **45**, 38 (2006).

- [58] J. W. Goodby, I. M. Saez, S. J. Cowling, V. Görtz, M. Draper, A. W. Hall, S. Sia, G. Cosquer, S.-E. Lee, and E. P. Raynes. *Transmission and Amplification of Information and Properties in Nanostructured Liquid Crystals*. Ang. Chem. Int. Ed. **47**, 2754 (2008).
- [59] C. Tschierske. *Development of Structural Complexity by Liquid-Crystal Self-assembly*. Ang. Chem. Int. Ed. **52**, 8828 (2013).
- [60] R. Berardi, A. P. J. Emerson, and C. Zannoni. *Monte Carlo investigations of a Gay-Berne liquid crystal*. J. Chem. Soc., Faraday Trans. **89**, 4069 (1993).
- [61] A. Galindo, A. J. Haslam, S. Varga, G. Jackson, A. G. Vanakaras, D. J. Photinos, and D. A. Dunmur. *The phase behavior of a binary mixture of rodlike and disclike mesogens: Monte Carlo simulation, theory, and experiment*. J. Chem. Phys. **119**, 5216 (2003).
- [62] R. van Roij. *The isotropic and nematic liquid crystal phase of colloidal rods*. Eur. J. Phys. **26**, S57 (2005).
- [63] H. Bartsch, M. Bier, and S. Dietrich. *Smectic phases in ionic liquid crystals*. J. Phys.: Condens. Matter **29**, 464002 (2017).
- [64] H. Bartsch, M. Bier, and S. Dietrich. *Interface structures in ionic liquid crystals*. To be published, arXiv:1901.03217 (2019).
- [65] R. Evans. *The nature of the liquid-vapour interface and other topics in the statistical mechanics of non-uniform, classical fluids*. Adv. Phys. **28**, 143 (1979).
- [66] N. Metropolis, A. W. Rosenbluth, M. N. Rosenbluth, A. H. Teller, and E. Teller. *Equation of State Calculations by Fast Computing Machines*. J. Chem. Phys. **21**, 1087 (1953).
- [67] M. Allen and D. Tildesley. *Computer Simulation of Liquids*. Oxford Science Publ. (Clarendon Press, Oxford, 1989).
- [68] P. Tarazona. *Free-energy density functional for hard spheres*. Phys. Rev. A **31**, 2672 (1985).
- [69] Y. Rosenfeld. *Free-energy model for the inhomogeneous hard-sphere fluid mixture and density-functional theory of freezing*. Phys. Rev. Lett. **63**, 980 (1989).

- [70] R. Roth. *Fundamental measure theory for hard-sphere mixtures: a review*. J. Phys.: Condens. Matter **22**, 063102 (2010).
- [71] S. Kondrat, M. Bier, and L. Harnau. *Phase behavior of ionic liquid crystals*. J. Chem. Phys. **132**, 184901 (2010).
- [72] B. J. Berne and P. Pechukas. *Gaussian Model Potentials for Molecular Interactions*. J. Chem. Phys. **56**, 4213 (1972).
- [73] J. G. Gay and B. J. Berne. *Modification of the overlap potential to mimic a linear site-site potential*. J. Chem. Phys. **74**, 3316 (1981).
- [74] J. D. Parsons. *Nematic ordering in a system of rods*. Phys. Rev. A **19**, 1225 (1979).
- [75] S.-D. Lee. *A numerical investigation of nematic ordering based on a simple hard-rod model*. J. Chem. Phys. **87**, 4972 (1987).
- [76] P. I. Teixeira and M. M. Telo da Gama. *Density-functional theory for the interfacial properties of a dipolar fluid*. J. Phys.: Condens. Matter **3**, 111 (1991).
- [77] C. M. Gordon, J. D. Holbrey, A. R. Kennedy, and K. R. Seddon. *Ionic liquid crystals: hexafluorophosphate salts*. J. Mater. Chem. **8**, 2627 (1998).
- [78] K.-M. Lee, Y.-T. Lee, and I. J. B. Lin. *Supramolecular liquid crystals of amide functionalized imidazolium salts*. J. Mater. Chem. **13**, 1079 (2003).
- [79] D. Ster, U. Baumeister, J. Lorenzo Chao, C. Tschierske, and G. Israel. *Synthesis and mesophase behaviour of ionic liquid crystals*. J. Mater. Chem. **17**, 3393 (2007).
- [80] M. Wang, X. Pan, S. Xiao, C. Zhang, W. Li, and S. Dai. *Regulating mesogenic properties of ionic liquid crystals by preparing binary or multi-component systems*. J. Mater. Chem. **22**, 2299 (2012).
- [81] H. Löwen. *Melting, freezing and colloidal suspensions*. Phys. Rep. **237**, 249 (1994).
- [82] F. A. Lindemann. *Über die Berechnung molekularer Eigenfrequenzen*. Phys. Z. **11**, 609 (1910).
- [83] J. J. Gilvarry. *The Lindemann and Grüneisen Laws*. Phys. Rev. **102**, 308 (1956).

- [84] X. H. Zheng and J. C. Earnshaw. *On the Lindemann criterion in 2D*. Europhys. Lett. **41**, 635 (1998).
- [85] E. de Miguel and C. Vega. *The global phase diagram of the Gay–Berne model*. J. Chem. Phys. **117**, 6313 (2002).
- [86] E. de Miguel, E. M. del Río, and F. J. Blas. *Stability of smectic phases in the Gay–Berne model*. J. Chem. Phys. **121**, 11183 (2004).
- [87] Y. Rosenfeld. *Density functional theory of molecular fluids: Free-energy model for the inhomogeneous hard-body fluid*. Phys. Rev. E **50**, R3318 (1994).
- [88] H. Hansen-Goos and K. Mecke. *Fundamental Measure Theory for Inhomogeneous Fluids of Nonspherical Hard Particles*. Phys. Rev. Lett. **102**, 018302 (2009).
- [89] H. Hansen-Goos and K. Mecke. *Tensorial density functional theory for non-spherical hard-body fluids*. J. Phys.: Condens. Matter **22**, 364107 (2010).
- [90] R. Wittmann, M. Marechal, and K. Mecke. *Fundamental mixed measure theory for non-spherical colloids*. Europhys. Lett. **109**, 26003 (2015).
- [91] R. Wittmann, M. Marechal, and K. Mecke. *Fundamental measure theory for non-spherical hard particles: predicting liquid crystal properties from the particle shape*. J. Phys.: Condens. Matter **28**, 244003 (2016).
- [92] S. Jabbari-Farouji, J.-J. Weis, P. Davidson, P. Levitz, and E. Trizac. *On phase behavior and dynamical signatures of charged colloidal platelets*. Sci. Rep. **3**, 3559 (2013).
- [93] S. Jabbari-Farouji, J.-J. Weis, P. Davidson, P. Levitz, and E. Trizac. *Interplay of anisotropy in shape and interactions in charged platelet suspensions*. J. Chem. Phys. **141**, 224510 (2014).
- [94] T. Koda and H. Kimura. *Phase Diagram of the Nematic-Smectic A Transition of the Binary Mixture of Parallel Hard Cylinders of Different Lengths*. J. Phys. Soc. Jpn. **63**, 984 (1994).
- [95] R. van Roij and B. Mulder. *Demixing versus ordering in hard-rod mixtures*. Phys. Rev. E **54**, 6430 (1996).

- [96] G. Cinacchi, L. Mederos, and E. Velasco. *Liquid–crystal phase diagrams of binary mixtures of hard spherocylinders*. J. Chem. Phys. **121**, 3854 (2004).
- [97] Y. Martínez-Ratón, E. Velasco, and L. Mederos. *Stability of smectic phases in hard-rod mixtures*. J. Chem. Phys. **123**, 104906 (2005).
- [98] R. van Roij, P. Bolhuis, B. Mulder, and D. Frenkel. *Transverse interlayer order in lyotropic smectic liquid crystals*. Phys. Rev. E **52**, R1277 (1995).
- [99] M. P. Neal and A. J. Parker. *Computer simulations using a longitudinal quadrupolar Gay–Berne model: effect of the quadrupole magnitude on the formation of the smectic phase*. Chem. Phys. Lett. **294**, 277 (1998).
- [100] R. Meyer, L. Liebert, L. Strzelecki, and P. Keller. *Ferroelectric liquid crystals*. J. Physique Lett. **36**, 69 (1975).
- [101] L. Mederos and D. E. Sullivan. *Smectic-A ordering at a liquid-vapor interface*. Phys. Rev. A **46**, 7700 (1992).
- [102] A. M. Somoza, L. Mederos, and D. E. Sullivan. *Wetting and layering transitions in liquid crystals*. Phys. Rev. E **52**, 5017 (1995).
- [103] S. Praetorius, A. Voigt, R. Wittkowski, and H. Löwen. *Structure and dynamics of interfaces between two coexisting liquid-crystalline phases*. Phys. Rev. E **87**, 052406 (2013).
- [104] G. Wulff. XXV. *Zur Frage der Geschwindigkeit des Wachstums und der Auflösung der Krystallflächen*. Kristallogr. Mineral. **34**, 449 (1901).
- [105] C. Blanc. *Measurement of the anisotropy of the energy of an isotropic-smectic interface in a smectic cylinder: Application to the L_3 - L_α interface*. Phys. Rev. E **64**, 011702 (2001).
- [106] B. Q. Lu, R. Evans, and M. M. T. da Gama. *The form of the density profile at a liquid-gas interface*. Mol. Phys. **55**, 1319 (1985).
- [107] P.-G. de Gennes. *Some effects of long range forces on interfacial phenomena*. J. Phys. Lett. **42**, 377 (1981).

- [108] J. A. Barker and J. R. Henderson. *Generalized van der Waals theories and the asymptotic form of the density profile of a liquid–vapor interface*. J. Chem. Phys. **76**, 6303 (1982).
- [109] S. Dietrich and M. Napiórkowski. *Analytic results for wetting transitions in the presence of van der Waals tails*. Phys. Rev. A **43**, 1861 (1991).
- [110] M. Wertheim. *Fluids of hard convex molecules*. Molecular Physics **83**, 519 (1994).
- [111] B. Groh and S. Dietrich. *Ferroelectric phase in Stockmayer fluids*. Phys. Rev. E **50**, 3814 (1994).